

ADVANCED ALGORITHMS TO ENHANCE SIGNAL TO NOISE RATIO OF PEEL PLY AT
THE BONDLINE OF OUT-OF-AUTOCLAVE COMPOSITE ASSEMBLIES

A Thesis by

Gary S. LeMay

Bachelor of Science, Wichita State University, 2013

Submitted to the Department of Mechanical Engineering
and the faculty of the Graduate School of
Wichita State University
in partial fulfillment of
the requirements for the degree of
Master of Science

December 2016

© Copyright 2016 by Gary S. LeMay

All Rights Reserved

ADVANCED ALGORITHMS TO ENHANCE SIGNAL TO NOISE RATIO OF PEEL PLY AT
THE BONDLINE OF OUT-OF-AUTOCLAVE COMPOSITE ASSEMBLIES

The following faculty members have examined the final copy of this thesis for form and content, and recommend that it be accepted in partial fulfillment of the requirement for the degree of Master of Science with a major in Mechanical Engineering.

Davood Askari, Committee Chair

Hamid Lankarani, Committee Member

Ali Eslami, Committee Member

DEDICATION

To my wife, Mrs. Lacey Cathcart LeMay, and my friends and family – whom I love, each of which have inspired me and have made numerous sacrifices during the years that I was away from them.

ACKNOWLEDGEMENTS

I would like to thank my advisor and committee chair, Dr. Davood Askari for his support, guidance and parallel direction that he has provided throughout this thesis. I would also like to thank my committee members Dr. Hamid Lankarani and Dr. Ali Eslami for taking the time to review this report and be a part of my thesis defense committee. I'm grateful to the composite layout technicians Jessica Lorenc, Robert Reiling and Roy Thrush, who assisted in the manufacturing of the representative reference standards that made this research possible. Additionally, special thanks goes out to the Boeing Automated Systems group for providing the necessary system, tools and software to make this project as success. I would also like to thank my current lead engineer Michael Grosser and my manager Michael Dame for their leadership during this project. I would like to especially thank my former lead engineer David Gayle whom is now an Associate Technical Fellow with the Boeing Company. David catapulted my career by believing in me and giving me the opportunity to achieve my goals.

ABSTRACT

The objective of this thesis is to develop an algorithm (based on mathematical functions) to improve the signal to noise ratio between constituents of similar acoustic impedance in bonded out-of-autoclave carbon fiber reinforced polymer assemblies. In particular, peel ply, a release fabric that may be trapped between the adhesive and the substrate during the manufacturing process. The assemblies consist of a pre-cured resin infused out-of-autoclave 3D woven fabric preform bonded to a pre-cured out-of-autoclave prepreg fabric substrate. Conventional ultrasonic nondestructive testing techniques and analysis software cannot consistently achieve signal to noise ratios that meet quantifiable rejection thresholds of accurately sized peel ply inserts at the bonded interface (i.e. bondline) of the aforementioned assemblies. To demonstrate the approach, ultrasonic pulse echo with full waveform capture was used to inspect a reference standard (i.e. representation of configuration and complexity of the part to be inspected) with peel ply inserts (sized according to minimum detectable requirements) placed between the film adhesive and the 3D woven fabric preform. The ultrasonic signal was produced by a 64 element array transducer with a central frequency of 2.8 Megahertz, utilizing a customary shoe and water bubbler. Waveform post-acquisition analysis with post processing software was used to analyze and enhance the signal response between the peel ply and the bondline resulting in the final algorithm. To verify the results, the signal to noise ratio of each insert was calculated for both the raw and processed data. As the measure of detectability, the method relies on principles of statistical measurement to provide an industry standard of 3:1 as the signal to noise response.

TABLE OF CONTENTS

Chapter	Page
1. INTRODUCTION	1
1.1 Introduction	1
1.2 Motivation	2
1.3 Research Objectives	5
1.4 Approach	8
2. LITERATURE REVIEW	11
2.1 What is Nondestructive Testing	11
2.2 Common Non Destructive Test Methods.....	12
2.2.1 Visual Testing	13
2.2.1.1 Applications	13
2.2.1.2 Advantages	13
2.2.1.3 Limitations	14
2.2.2 Liquid Penetrant Testing	14
2.2.2.1 Applications	15
2.2.2.2 Advantages	15
2.2.2.3 Limitations	15
2.2.3 Magnetic Particle Testing.....	15
2.2.3.1 Applications	16
2.2.3.2 Advantages	16
2.2.3.3 Limitations	17
2.2.4 Eddy Current Testing	17
2.2.4.1 Applications	19
2.2.4.2 Advantages	19
2.2.4.3 Limitations	19
2.2.5 Radiography Testing	19
2.2.5.1 Applications	21
2.2.5.2 Advantages	22
2.2.5.3 Limitations	22
2.2.6 Ultrasonic Testing	22
2.2.6.1 Applications	26
2.2.6.2 Advantages	27
2.2.6.3 Limitations	27
2.2.7 Acoustic Emission Testing.....	28
2.2.7.1 Applications	29
2.2.7.2 Advantages	29
2.2.7.3 Limitations	30

TABLE OF CONTENTS (continued)

Chapter	Page
2.3	Recent Advances of Non Destructive Test Methods - CFRP Bonded Assemblies 30
2.3.1	Laser Bond Inspection..... 31
2.3.1.1	Applications 33
2.3.1.2	Advantages 33
2.3.1.3	Limitations 33
2.3.2	Infrared Thermography Testing 34
2.3.3	Lock-In Thermography Testing 35
2.3.3.1	Applications 38
2.3.3.2	Advantages 39
2.3.3.3	Limitations 39
2.3.4	Digital Shearography Testing..... 39
2.3.4.1	Applications 44
2.3.4.2	Advantages 44
2.3.4.3	Limitations 44
2.4	Ultrasonics and Optimization..... 45
2.4.1	Ultrasonic Transducer 45
2.4.2	Ultrasonic Frequency 48
2.4.3	Signal Optimization..... 48
3.	METHODOLOGY 49
3.1	Reference Standard Materials 49
3.1.1	Out-of-Autoclave Fabric Substrate 49
3.1.2	Out-of-Autoclave Fabric Preform 50
3.1.3	Peel Ply Inserts 51
3.1.4	Film Adhesive 51
3.2	Reference Standard Assembly 51
3.3	Ultrasonic Setup and Inspection of the Reference Standard 53
3.3.1	Ultrasonic System Details 54
3.3.2	Ultrasonic Parameters 55
3.3.3	Ultrasonic Inspection..... 61
4.	ALGORITHM DEVELOPMENT 63
4.1	Algorithm Workflow..... 63
4.2	Signal conditioning functions..... 64
4.2.1	Filtering 64
4.2.2	Rectification 65
4.2.3	Gain Control..... 67
4.2.4	Scale/Offset 68

TABLE OF CONTENTS (continued)

Chapter	Page
4.3 Gating Functions	68
4.3.1 Fixed Gate	69
4.3.2 Variable Gate.....	69
4.3.3 Peak Tracking Gate	70
4.4 Output.....	71
4.4.1 Minimum- Maximum Output.....	71
4.4.2 Gate Position	72
4.4.3 Integrate.....	73
4.4.4 Peak Detection.....	74
4.4.5 A-Scan Output.....	75
4.5 Ultrasonic Waveform Region of Interest	76
4.6 Final Algorithm	78
4.6.1 Signal Conditioning Algorithm Workflow	78
4.6.2 Zero Front Surface Algorithm Workflow	81
4.6.3 Integrate Algorithm Workflow.....	82
5. ANALYSIS AND RESULTS.....	85
5.1 Analysis.....	85
5.2 Results	90
6. CONCLUSION.....	95
7. FUTURE WORK.....	98
REFERENCES	100
APPENDIX.....	111

LIST OF TABLES

Table		Page
1.	Reflection coefficient and percent reflection based on acoustic impedance of selected combinations of materials based on standard material properties	4
2.	Peel ply insert signal to noise ratio summary	92

LIST OF FIGURES

Figure		Page
1.	(a) C-Scan of two composite parts bonded together with imbedded peel ply inserts and the difference in the ultrasonic waveform reflections from (b) the peel ply insert and (c) the bondline.....	5
2.	Scattering by material causing grain noise that obscures signals from an internal flaw where (a) represents the ultrasonic pulse/echo inspection and (b) represents the ultrasonic A-Scan as a rectified signal [16].....	6
3.	C-Scan images of (a) autoclave cured fabric standard, (c) oven cured fabric standard and the resulting A-Scans (b) and (d) illustrating extraneous ultrasonic signals	7
4.	Rectified signal response illustrating the height of the baseline noise compared to the peak signal of interest	8
5.	Illustration of (a) single elements as an array producing longitudinal waves and the (b) array transducer with (c) water bubbler	9
6.	Representative reference standard that shows the pre-cured OoA 3D woven fabric preform, the pre-cured OoA base substrate, the bondline between the two and the peel ply inserts placed between the bondline and the fabric preform.....	9
7.	Resulting C-Scan image of the representative reference standard.....	10
8.	Working principles of the liquid penetrant process (a) application of the liquid penetrant, (b) removal of the liquid penetrant and (c) application of the developer and resulting capillary action [24]	14
9.	Working principles of magnetic particle testing [27]	16
10.	Working principles of eddy current testing [31].....	18
11.	Eddy currents being disrupted by a defect at or near the surface [31].....	18
12.	Electromagnetic Spectrum [32]	20
13.	Working principles of radiography testing [34].....	21
14.	Types of ultrasonic techniques a) pulse-echo, b) pitch-catch and c) thru-transmission [39]	23

LIST OF FIGURES (continued)

Figure	Page
15. Illustration of particles at rest, longitudinal and shear wave propagation within a solid material [40].....	24
16. Typical (a) pulse echo system, (b) A-Scan, (c) B-Scan and (d) C-Scan.....	26
17. Working principles of acoustic emission testing [44].....	29
18. Bondline defects a) foreign material, b) disbond, c) voids, d) kissing bond	31
19. Overall Laser Bond Inspection (LBI) process [56].....	32
20. Results comparing Laser Bond Inspection (LBI) fluence (J/cm^2) to ultrasonic testing (UT) of a pulse echo C-Scan image [56]	33
21. Flow chart illustrating the different active thermography approaches [61].....	35
22. Top view of the setup used for lock-in thermography of composite lap shear samples ($\beta = 30^\circ$, $DT = 30cm$, $DL = 20cm$) [67]	36
23. Maximum phase angle by testing carried out on specimen VA0. A_1 and A_2 represent defect and defect free areas, respectively, to determine phase angle [67].....	37
24. Phase image results, based on optimum frequency of 0.0125 Hz obtained by test specimen VA0 and sequential test specimens VA01 – VA12, where black areas indicate debonding and green lines represent areas of interest due to partial debonding [67].....	38
25. Schematic layout of the working principles of digital shearography a) working principles of the system, b) non deformed and deformed observations (1 and 2) of the acquired analog signals, c) digital interferometric images (state 1 and state 2) with the resulting shearogram (relative phase change) [72]	40
26. CFRP air-cooled inlet (top view) illustrating the cracked region and the length and width of the disbond between the local stiffener and external skin [77]	41
27. Shearogram with Piezo shaker placement on the inspection surface at six different locations a-f [77]	42
28. Shearogram illustrating the imposed stress vibration field and localized complex fringe pattern for regions of interest (ROI) reinforced by bonded stiffeners (A, B, and C) and disbanded ROI (D) [77]	42

LIST OF FIGURES (continued)

Figure	Page
29. Shearograms of thermal loading inspections from (a) and (b) the back surface of the composite assembly, as well as from (c) the external surface. The revealed disbanded stiffener is highlighted in shearograms (b) and (c) [77]	43
30. Array transducer with a water bubbler manufactured by GE Inspection Technologies ...	46
31. Working principles of a 1D focused linear array transducer utilizing an active group of elements electronically focused to a specific depth and scanned horizontally [37]	46
32. Single element transducer and the ultrasonic sound field that is produced [40]	47
33. Illustration of the transducer array	47
34. OoA fabric substrate – prepreg CFRP of 8HS fabric	49
35. Pattern of an 8 Harness Satin Weave Fabric [82]	50
36. OoA fabric preform – oven cured 3D woven multilayer fabric.....	50
37. 3D multilayer woven fabric [83].....	50
38. PTFE-coated plain weave fiberglass a) cloth and b) inserts	51
39. Representation of the OoA fabric substrate and dimensions	52
40. Representation of the film adhesive placed atop the OoA fabric substrate	52
41. Representation of the peel ply insert locations and dimensions placed atop the film adhesive.....	52
42. Representation of the OoA fabric preform placed atop the peel ply inserts	53
43. CAD model illustrating the reference standard in an exploded view	53
44. Peel ply inserts extended beyond the fabric preform for reference.	53
45. Representation of the overall system	54
46. Array transducer setup atop the reference standard.....	54
47. Parameters tab utilized to configure the end effector selection and data parameters	55

LIST OF FIGURES (continued)

Figure	Page
48. Edit Pulser/Receiver window.....	56
49. PE Depth tab utilized to configure the desired output in inches.....	57
50. PE Amplitude tab utilized to configure the desired output in dB.....	58
51. Low Pass Filter tab utilized to configure the low pass filter	58
52. Time Corrected Gain (TCG) tab utilized to setup the TCG over a range of thicknesses .	59
53. A-Scan display illustrating the reflections from the surface and back surface of the test object.....	59
54. A-Scan display illustrating the pulse echo depth gate, triggered by the “main bang” (i.e. initial signal transmitted by the transducer).....	60
55. A-Scan display illustrating the pulse echo amplitude gate, triggered by the first interface (i.e. initial signal transmitted by the surface of the test object)	60
56. A-Scan display illustrating the time corrected gain (TCG), triggered by the first interface (i.e. compensation of gain as a function of time to obtain the same signal amplitude of reflections form equal reflectors at different thicknesses).....	60
57. Ultrasonic inspection of the reference standard.....	61
58. Amplitude C-Scan of the reference standard with front and back surface reflectors as reference.....	61
59. Resulting edge reflection that is not normal to the surface.....	62
60. Comparison of attenuation due to the edge of the insert and the center of the insert.....	62
61. Algorithm Workflow	63
62. Examples of (a) low-pass and (b) high-pass filtering including an input signal, impulse response and output signal [84]	64
63. IIR low pass and high pass filter menu function and parameters	65
64. Raw data (yellow) and post processed data (white) of (a) full wave rectification, (b) positive half-wave rectification and (c) negative half-wave rectification	66

LIST OF FIGURES (continued)

Figure	Page
65. Rectifier menu function and parameters	66
66. Variable gain menu function and parameters	67
67. Automatic gain control (ACG) menu function and parameters.....	67
68. Examples of the Scale/Offset menu function and parameters, with the raw and post processed A-Scan results	68
69. Fixed gate menu function and parameters	69
70. Variable gate menu function and parameters.....	70
71. Peak tracking gate menu function and parameters	71
72. Minimum-Maximum function menu and parameters	72
73. Gate position function menu and parameters.....	73
74. Integrate function menu and parameters.....	74
75. Peak detection function menu and parameters.....	75
76. A-Scan Output function menu and parameters	76
77. A-Scan Output tabs that shows the result in the A-Scan	76
78. Ultrasonic waveform of the peel ply insert and the bondline in the frequency domain ...	77
79. Ultrasonic waveform of the peel ply insert and the bondline in the time domain	78
80. Signal conditioning algorithm workflow	79
81. Ultrasonic waveform with variable gain.....	80
82. Ultrasonic waveform with low pass filter.....	80
83. Ultrasonic waveform with scale/offset	80
84. Ultrasonic waveform illustrating the region of interest	81

LIST OF FIGURES (continued)

Figure	Page
85. Zero front surface algorithm workflow.....	81
86. Front surface signal reflection set to zero	82
87. Integrate algorithm workflow	83
88. Post processed integration of the bondline and peel ply insert.....	84
89. Final integration algorithm	84
90. Amplitude C-Scan data with parameter tab (AmplBW).....	85
91. Integration C-Scan post processed data with parameter tab (Integrate_XMT_pp)	86
92. Identification of peel ply inserts with histogram polygons on C-Scan by (a) amplitude and (b) integration.....	86
93. Histogram statistics tool displaying data from within the polygon	87
94. Length of inserts with length perpendicular to the edge of the OoA fabric preform.....	87
95. Illustration of the amplitude gate and the signal amplitude from both the edge and center of the insert	88
96. Bimodal histogram with low and high signal attenuation	89
97. AMP1 insert with high attenuation extending beyond the actual size.....	89
98. Integrated signals from the (a) gated bondline and (b) the gated peel ply.....	90
99. Unimodal histogram with an accurately sized insert using upper threshold	90
100. Amplitude C-Scan with statistical values for each insert using the lower threshold.....	91
101. Integrated C-Scan with statistical values for each insert using the upper threshold.....	91
102. Signal to noise ratio of 0.25” by 1.00” peel ply inserts	93
103. Signal to noise ratio of 0.375” by 1.00” peel ply inserts	93

LIST OF ABBREVIATIONS / NOMENCLATURE

8HS	8 harness satin fabric
AE	Acoustic Emission
AMP	Identification of the Amplitude Insert
ASTM	American Society for Testing and Materials
AUSS	Automated Ultrasonic Scanning System
CFRP	Carbon Fiber Reinforced Polymer
dB	Decibels
DST	Digital Shearography Testing
ET	Eddy Current Testing
FBH	Flat Bottom Hole
GWI	Guided Wave Inspection
IIR	Infinite Impulse Response
INT	Identification of the Integrated Insert
IR	Infrared Camera
IRT	Infrared Thermography Testing
ISO	International Standards Organization
LBI	Laser Bond Inspection
LT	Lock-In Thermography
MIL-STD	Military Standard
MT	Magnetic Particle Testing
NDT	Non Destructive Testing
NMAB	National Material Advisory Board
OEM	Original Equipment Manufacturer

LIST OF ABBREVIATIONS / NOMENCLATURE (continued)

OoA	Out-of-Autoclave
PA	Phased Array
PE	Pulse Echo
PEA	Pulse Echo Amplitude
PED	Pulse Echo Depth
PT	Liquid Penetrant Testing
PTFE	Polytetrafluoroethylene
RF	Radio Frequency
ROI	Region of Interest
RT	Radiography Testing
RTM	Resin Transfer Molding
SHM	Structural Health Monitoring
SNR	Signal to Noise Ratio
STD	Standard
TCG	Time Corrected Gain
UT	Ultrasonic Testing
VT	Visual Testing
XMT	Transmit Side of the System

LIST OF SYMBOLS

Z	Acoustic Impedance
v	Velocity
$ \Delta\phi $	Absolute Phase Angle
μ_1	Background Mean
Br-	Bromide Ion
cm ²	Centimeter Squared
μ_2	Defect Mean
ρ	Density
d	Distance
eV	Electron Volt
f	Frequency
Hz	Hertz
in	Inches
J	Joules
kHz	Kilohertz
MHz	Megahertz
μsec	Microsecond
ω	Modulation Frequency
nm	Nanometer
Φ	Phase Angle
V_0	Reference Volt
R	Reflection Coefficient
$y[n]$	Running Sum

LIST OF SYMBOLS (continued)

Ag^+	Silver Ion
c_p	Specific Heat Constant
σ	Standard Deviation
k	Thermal Conductivity
μ	Thermal Diffusion
α	Thermal Diffusivity
t	Time
$x[n]$	Value of Original Signal
V	Volt
λ	Wavelength

CHAPTER 1

INTRODUCTION

1.1 Introduction

Carbon fiber reinforced polymer (CFRP) composites are becoming very popular for high volume applications such as automobiles, boats, turbine blades, sporting equipment and high performance military, commercial and aerospace structures. Structural performance such as high specific strength, stiffness, fracture toughness, fatigue strength and durability are favorable attributes of CFRP compared to alternative materials. CFRP composites can now be designed to incorporate specific geometry configurations as well as provide visual appealing aesthetics. One of the main advantages is the capability to tailor CFRP composites towards specific applications based on loading conditions in which fibers are aligned to carry the required loads and deformations [1]. CFRP also provides opportunities for weight reduction and fuel savings, lowering operating expenses. Over 50 percent of next generation commercial aircraft will include some type of fiber reinforced composite with percentages increasing for military applications [2]. These attributes lead to extended research opportunities to reduce manufacturing processing steps and time improving part quality providing a simpler more cost effective product.

Out-of-Autoclave (OoA) materials have long been an established material system for secondary structural applications; however, recent advancements in material properties allow for more advanced structural applications [2]. Therefore, OoA materials are very close to becoming the alternative for primary structure (i.e. responsible for load bearing) applications satisfying reduced manufacturing requirements. OoA composite materials can be cured at lower temperatures and pressures within ovens via vacuum-bag-assist; therefore, high capital costs

such as autoclaves can be disregarded during the manufacturing process especially for very large composite parts. Original Equipment Manufacturers (OEM's) of composite aerospace structures (i.e. Boeing, Airbus, Textron, etc.) can now award work to suppliers (i.e. companies that can offer more specific services at a reduced cost) that was impossible to obtain due to high operating costs attributed to autoclaves. OoA materials can be fabricated with fewer complications, allowing for flexible manufacturing. Therefore, large composite structures can be produced with various geometrical configurations such as incorporated stiffeners then co-cured in one cycle [2].

1.2 Motivation

Even though certain OoA properties have achieved parity with autoclaved cured materials, OoA materials are cured at reduced temperatures and pressures resulting in less compaction. Therefore, voids and volatiles such as air and moisture are not always evacuated from the structure. These voids and volatiles cause surface roughness and internal scattered noise reducing sensitivity of conventional nondestructive testing (NDT) methods compromising the inspection and results.

Moreover, bonded joints further increase inspection complexity due to the addition of the bondline. Adhesively bonded joints in CFRP composites are slowly replacing alternative mechanical joining processes providing a number of advantages such as reduced structural weight, fabrication costs, and number of structural components with improved damage tolerance [3]. Traditional aerospace joining methods utilize various types of fasteners that must be inserted into holes, cutting the fibers inducing stress risers significantly deteriorating structural performance. These holes and cuts are especially detrimental to OoA materials that currently just meet property requirements for primary structures. Hence, bonded joints have been developed to

overcome these issues; designed to endure typical static and cyclic loads for specific amounts of time with little to no effect on the load bearing capability of the composite assembly [3]. Bonded joints are currently being utilized with co-cured OoA materials to manufacture integrated aerospace assemblies for structural applications [3]. However, as the number of bonded joints increase, so does the opportunity for defects (i.e. rejectable indications) to transpire; increasing the need for appropriate in-process NDT inspections during the manufacturing process.

Defects inherent to each type of composite laminate, including bonded joints, that must be reliably detected based on reference standards by instrumental NDT methods are specifically voids, delaminations and inclusions. One type of inclusion that may find its way into the assembly, especially the bondline, during the manufacturing process is peel ply (i.e. release film); by definition an inclusion of foreign material. Peel ply is a Teflon coated polymeric thin film used to prevent the prepreg resin from bleeding through the release fabric and into the breather fabric during the layup process. It is also used to keep outer surfaces of the pre-cured substrates clean and free from contamination prior to any further manufacturing such as bonding. Consequently, peel ply must be accounted for during the entire manufacturing process. Therefore, nondestructive inspection processes must be able to reliably detect peel ply to ensure all foreign materials have been removed. If left behind, peel ply creates a delamination between the adhesive and the mating surface due to its design not to adhere. Peel plies are commonly used as inserts to establish an initial delamination for a variety of fracture toughness testing modes [4]. Therefore, peel ply will be the source of crack initiation causing catastrophic failure.

Unfortunately, peel ply is one of the most difficult types of foreign material to quantifiably detect ultrasonically in OoA fabric materials especially at the bonded interface. To distinguish between two types of materials the reflection coefficient from the boundary must be

of a distinguishable value to obtain the desired signal to noise ratio. The greater the mismatch, the more energy is reflected at the interface increasing the signal amplitude. The acoustic impedance Z of a material is the product of material density ρ and acoustic velocity v according to equation (1.1) [5].

$$Z = \rho * v \quad (1.1)$$

The reflection coefficient R for longitudinal waves is then determined by equation (1.2) where Z_1 is the acoustic impedance of the first material and Z_2 is of the second [6].

$$R = \left(\frac{Z_2 - Z_1}{Z_2 + Z_1} \right)^2 \quad (1.2)$$

Table 1 shows the reflection coefficient and percent reflection based on the acoustic impedance between selected combinations of materials based on standard material properties.

Table 1

Reflection coefficient and percent reflection based on acoustic impedance of selected combinations of standard material properties [7-11]

Material	Density [lb/in ³]	Material Velocity [in/μsec]	Acoustic Impedance [lb/in ² s]	Reflection Coefficient	Percent Reflection
Fiberglass	4.69E-02	1.08E-01	5.07E+03	2.430E-02	2.43%
Composite	5.78E-02	1.20E-01	6.94E+03		
Polyamide	4.48E-02	8.70E-02	3.90E+03	7.866E-02	7.87%
Composite	5.78E-02	1.20E-01	6.94E+03		
Brass	3.09E-01	1.74E-01	5.38E+04	5.954E-01	59.54%
Composite	5.78E-02	1.20E-01	6.94E+03		
Air	4.43E-05	1.30E-02	5.75E-01	9.997E-01	99.97%
Composite	5.78E-02	1.20E-01	6.94E+03		
Fiberglass	4.69E-02	0.108	5.07E+03	1.697E-02	1.70%
Polyamide	4.48E-02	0.087	3.90E+03		

It is clear that the acoustic impedance between fiberglass (i.e. material properties selected for the peel ply insert) and the polyamide material (i.e. material properties selected for the film adhesive) is very similar resulting in a reflection coefficient of 0.01697 with only a 1.70% reflection. Therefore, peel ply does not create an easily detectable reflection at the bondline as does brass and air with 60% and 99.97% reflection, respectively. Furthermore, Figure 1 shows less than a 0.1 Volt difference in the ultrasonic waveform reflection from the peel ply insert and the bondline.

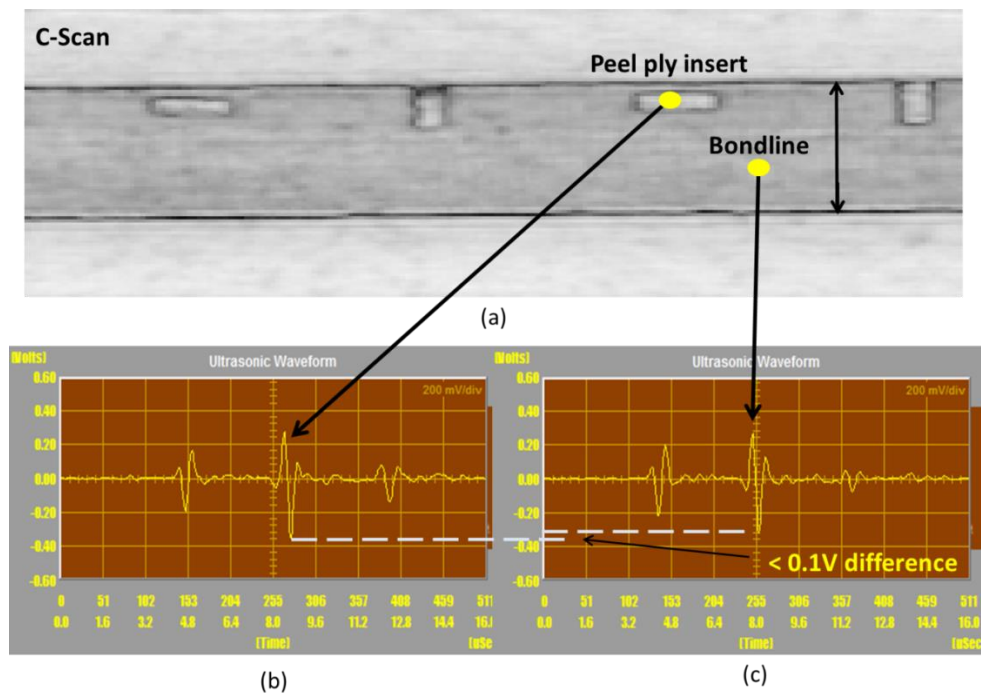


Figure 1: (a) C-Scan of two composite parts bonded together with imbedded peel ply inserts and the difference in the ultrasonic waveform reflections from (b) the peel ply and (c) the bondline

1.3 Research Objectives

Ultrasonic Testing (UT) is the primary approved volumetric NDT method used to inspect both autoclave and out-of-autoclave cured composite laminates, and bonded composite assemblies for aerospace applications [12- 14]. UT is superior to other evaluation methods for a

number of reasons such as the ability to perform single sided inspection to identify critical defects (e.g. delamination, disbonds, foreign material, porosity, etc.), depth position and size accuracy. However, UT can be challenging in materials that are not homogenous, rough, irregular in shape, or very thin [15]. Likewise, porous metals and materials of large grain structure can obscure indications from discrepancies due to scattered noise leading to false calls and uncertain results. Figure 2 shows a pulse echo (PE) inspection and scattered noise (i.e. noisy signal) as a result of large grain sizes within a metallic specimen.

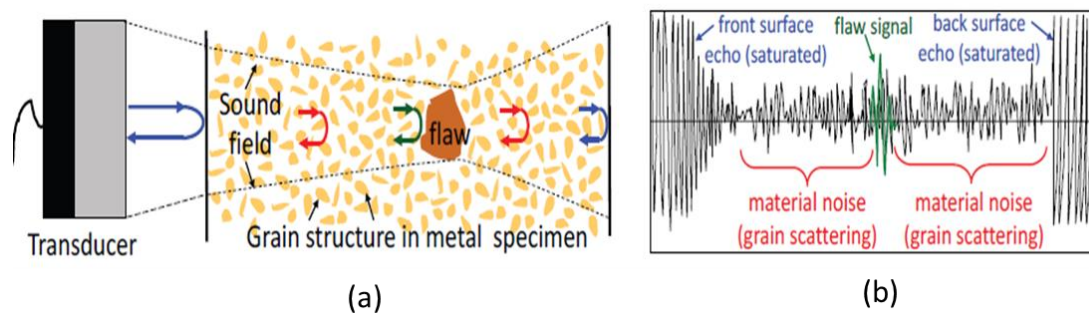


Figure 2: Scattering by material causing grain noise that obscures signals from an internal flaw where (a) represents the ultrasonic pulse/echo inspection and (b) represents the ultrasonic A-Scan as a rectified signal [16]

Out-of-Autoclave CFRP materials are less homogenous than autoclave cured due to reduced pressures and temperatures [17]. The consequence is extraneous ultrasonic signals (i.e. noise) due to internal reflections and refractions that cause attenuation potentially masking defects leading to unidentifiable indications. Figure 3 shows the A-Scan (i.e. analog signal) result of extraneous ultrasonic signals within an out-of-autoclave cured fabric standard compared to autoclave cured.

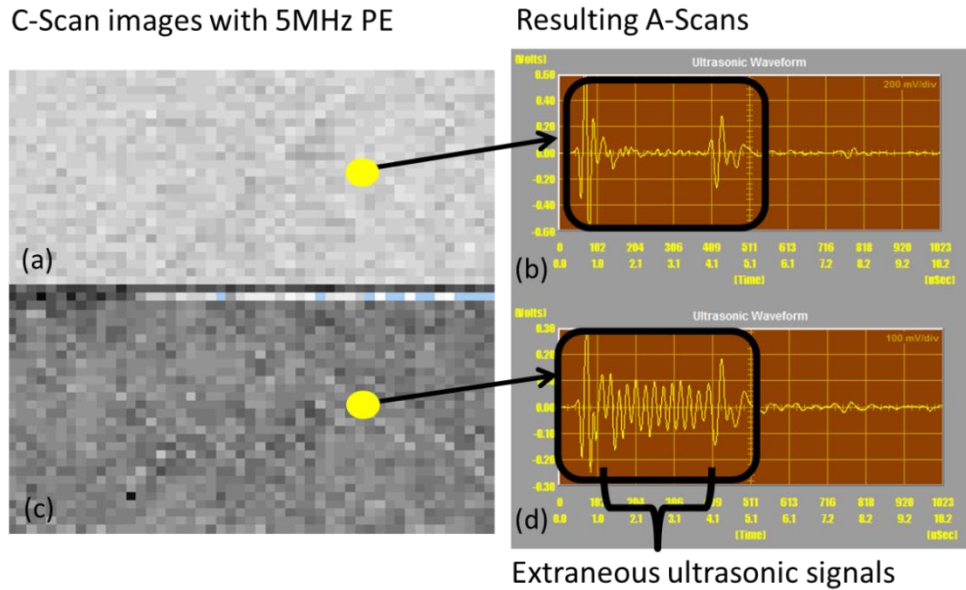


Figure 3: C-Scan images of (a) autoclave cured fabric standard, (c) oven cured fabric standard and the resulting A-Scans (b) and (d) illustrating extraneous ultrasonic signals

Extended research has been conducted to differentiate ultrasonic scattering within the material (medium) to improve the probability of defect detection in noisy materials [18]. However, to reliably detect defects signal-to-noise ratios (SNR) must be calculated to ensure capability of the NDT equipment, verify the process and the quality of reference standards. The SNR is the measure of detectability of a defect and is the most appropriate means of quantifying defects by statistical methods, eliminating false calls by optimizing reliability. A SNR of 3:1 is a typical industry standard determined from a signal response of a defect by means of a reference standard [14, 19]. Figure 4 depicts the height of the baseline noise (N) from the rectified signal compared to the peak signal of interest (S).

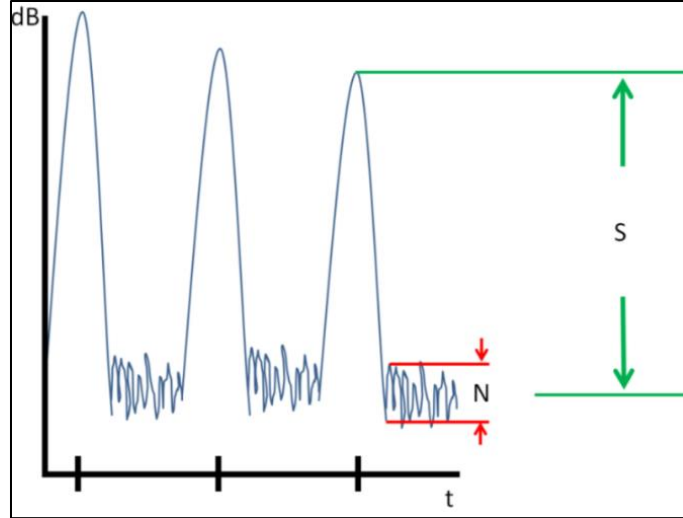


Figure 4: Rectified signal response illustrating the height of the baseline noise compared to the peak signal of interest

SNR values can be calculated according to equation (1.3); the mean value that accurately sizes the defect by $\pm 25\%$ is subtracted from the background mean of a known good area adjacent to the defect and then divided by the standard deviation of the background. Where μ_2 is the mean value of the defect, μ_1 is the background mean and σ_1 is the standard deviation of the background.

$$\frac{(\mu_1 - \mu_2)}{\sigma_1} \quad (1.3)$$

Therefore, it is imperative that the appropriate NDT method and signal processing techniques are developed to quantify and reliably detect peel ply at the bondline of OoA composite assemblies.

1.4 Approach

To demonstrate the approach, ultrasonic pulse echo with phased array (PA) was conducted utilizing a water bubbler system as the coupling mechanism allowing for signal transmission from the transducer to the reference standard. Figure 5 shows the working mechanism of the array transducer and the array transducer with water bubbler.

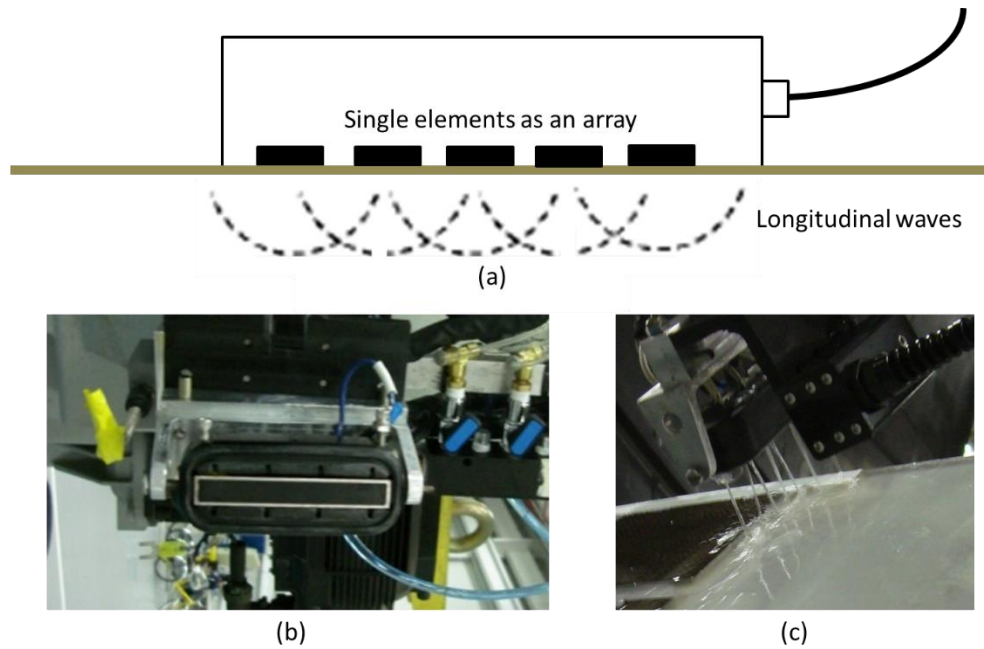


Figure 5: Illustration of (a) single elements as an array producing longitudinal waves and the (b) array transducer with (c) water bubbler

The ultrasonic frequency selected was 2.8 MHz (i.e. central frequency) based on sensitivity, resolution and attenuation. Evaluation was performed utilizing a representative reference standard shown in Figure 6. The reference standard was assembled with peel ply inserts placed between the bondline and the pre cured OoA 3D woven fabric preform and bonded to the pre cured OoA fabric substrate. Figure 7 depicts the resulting initial C-Scan (i.e. a two dimensional display as a planer view) image of the reference standard.

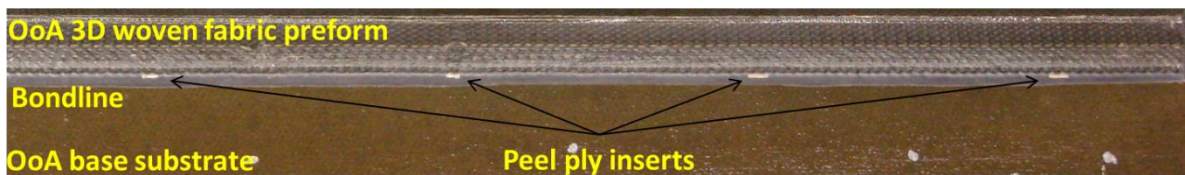


Figure 6: Representative reference standard that shows the pre-cured OoA 3D woven fabric preform, the pre-cured OoA base substrate, the bondline between the two and the peel ply inserts placed between the bondline and the fabric preform

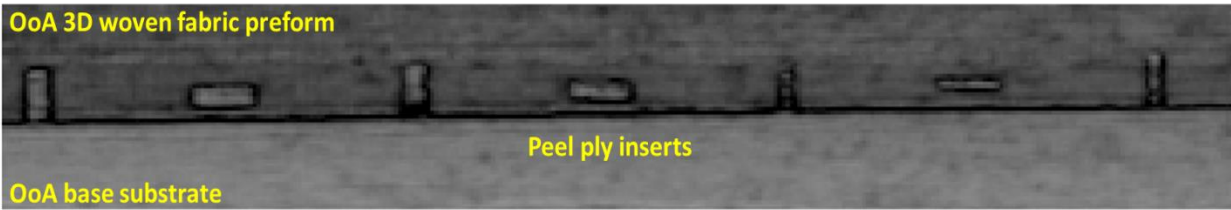


Figure 7: Resulting C-Scan image of the representative reference standard

Advanced algorithm software tools (Matlab based) were then configured and applied to the raw ultrasonic signal to improve the SNR between the peel ply inserts and the bondline. The objective of this work is to provide a reliable ultrasonic test method to quantify defects of similar acoustic impedance such as peel ply inserts at the bondline of large co-cured OoA composite aerospace structures. The results will be incorporated into the manufacturing process as an approved ultrasonic inspection technique fulfilling all established requirements for the assembly under consideration.

CHAPTER 2

LITERATURE REVIEW

This chapter provides a review of common nondestructive test methods and recent advances relevant to the inspection of CFRP bonded assemblies. Throughout this research each nondestructive test method selected to evaluate CFRP bonded assemblies utilized ultrasonic testing as the baseline or verification. It is clear that ultrasonic testing is the most comprehensively approved and suitable nondestructive test method based on acceptance criterion requirements for CFRP materials and bonded composite assemblies. The ultrasonic transducer and frequency were selected based on function to provide the desired output for signal optimization.

2.1 What is Nondestructive Testing

Nondestructive Testing (NDT) provides a mean to determine the condition and quality of materials and structures without damaging it, while maintaining its integrity and performance. The science of NDT incorporates numerous technologies either in-process (i.e. during manufacturing) or in-service (i.e. in operation) that characterize a materials property and or integrity. The term applies to non-medical applications such as aerospace, automotive, roads and bridges, pipelines, trains, power and refinery stations, and many more. The science of NDT cannot determine the future usefulness of a material or structure, but it can provide quality assurance ensuring safety and reliability throughout the lifetime. Significant variations in material properties and characteristics can be determined and measured from initial test articles to final service applications, such as residual stress, alloy type, hardness and microstructure to name a few. Depending on the technology, material parameters such as, defects (i.e. rejectable indications), discontinuities (i.e. indications that may not be a defect), structural integrity,

malstructure, dimensions, physical and mechanical properties, composition and chemical analysis and dynamic stress responses can be concluded [20]. The resulting information may be determined by a single method or a combination thereof. Secondary methods (i.e. alternative NDT method in conjunction with the primary as an aid or verification) may be necessary to conclude the inspection. NDT ensures the product meets the requirements and inspections are conducted (established by standard practices), based on specific standards such as American Society of Testing and Materials (ASTM), Military Standards (MIL-STD), International Organization for Standardization (ISO), etc. Rising costs of part failure increases the demand for sounder materials; therefore, NDT provides a mean to warrant such materials and structures are manufactured and assembled at a higher quality without rising costs [20].

2.2 Common Non Destructive Test Methods

The National Material Advisory Board (NMAB) has classified the following NDT methods into six categories as the majority: visual, penetrating radiation, magnetic-electrical, mechanical vibration, thermal and chemical/electrochemical [20]. Each of which can be characterized by a number of principle factors such as source, nature of the signal, means of detection, means of recording and interpretation. Research continues to improve NDT methods applying physics and scientific principles. Most of these “other methods” have yet to reach maturity and become known as an approved industry standard test method. The most common standard test methods include Visual and Optical Testing (VT), Liquid Penetrant Testing (PT), Magnetic Particle Testing (MT), Electromagnetic or Eddy Current Testing (ET), Radiography Testing (RT), Ultrasonic Testing (UT) and Acoustic Emission Testing (AE) [21].

2.2.1 Visual Testing

Visual testing (VT) is the oldest and most basic NDT method. It is also the most common because it is essential to perform many other test methods [21]. Visual testing depends on the human eye to find and verify defects with or without aid [22]. Inspections are either performed by direct or indirect (i.e. remote) techniques. Direct techniques require the eye to be within 24 inches of the surface of the test object at an angle no less than 30 degrees [22]. Indirect techniques include borescopes, cameras and computer aided vision systems with resolution comparable to direct. Mirrors and magnification tools are allowed to improve line of sight and field of view.

2.2.1.1 Applications

VT can be applied to any type of material(s) for the detection of surface and subsurface (e.g. translucent materials) defects. Applications consist of outer and inner (e.g. pipe, stringer, holes) surface conditions (e.g. tears, cracks, corrosion, chips, etc.), part or material alignment, leaks, etc. VT is most commonly conducted prior to any other NDT method to ensure adequate part preparation and verify presence of surface anomalies that may misconstrue results.

2.2.1.2 Advantages

VT is a simple test method that can be performed quickly. In some cases may be conducted while the part or material is in use [23]. VT is inexpensive producing instant results with minimal operator training. Secondary inspections with VT are common and effective in interpreting results.

2.2.1.3 Limitations

Visual testing is limited to surface inspections on opaque materials. Line of sight, adequate illumination and acceptable part surfaces are required to accurately perform the inspection. Access to interior surfaces may be difficult and remote equipment may be expensive.

2.2.2 Liquid Penetrant Testing

Similar to visual testing, liquid penetrant testing (PT) is used to detect surface defects after the surface has been thoroughly cleaned and dried. Any contaminants will affect the test results. Once the surface is prepared, colored or fluorescent dyes are applied to the surface of the test object. Most common colored penetrant dyes are red and only require white light for detection. Fluorescent dyes require a dark area (i.e. dark room) and require ultraviolet light for detection. Liquid penetrant dyes rely on capillary action allowing the dye to be drawn into surface indications. The excess dye is then removed once the dwell time (i.e. period of time allowing the dye to sit) is complete. Then the developer is applied assisting as a blotter to draw the dye from the indication to the surface. A visual examination is then conducted to examine the surface of the part interpreting the results. The working principles of the liquid penetrant process are shown in Figure 8.

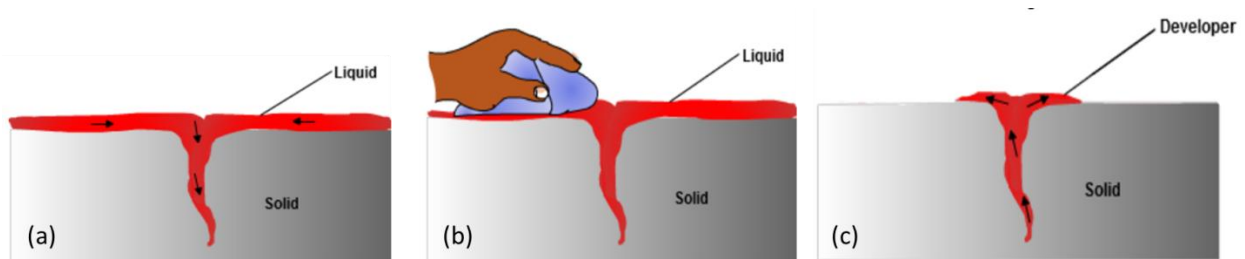


Figure 8: Working principles of the liquid penetrant process (a) application of the liquid penetrant, (b) removal of the liquid penetrant and (c) application of the developer and resulting capillary action [24]

The process greatly improves the detectability of surface indications by either providing contrast between the dye and the part or by making indications appear larger due to bleed out. Most indications found with liquid penetrant testing would have otherwise gone unnoticed with just a visual test alone.

2.2.2.1 Applications

PT is sufficient for the detection of defects open to the surface of non-permeable materials such as pits, cracks, scratches, surface porosity, etc. PT is most commonly conducted on materials that are ferrous and nonferrous metals and alloys as well as ceramics, glass and plastics [25].

2.2.2.2 Advantages

PT is sensitive to small surface defects and can be performed on a large selection of material types. PT is a quick inspection method that can be conducted on numerous small parts at once, complex geometries or large surface areas. PT is portable and inexpensive.

2.2.2.3 Limitations

PT is limited to surface defects that must permit proper penetrant fill. Complete access to the inspection surface is required. Inspections may be inconclusive on porous materials such as castings, anodized aluminum, and nonmetallic parts. Critical procedures must be followed such as surface cleaning, dwell times, and applications of appropriate dyes and developers [24].

2.2.3 Magnetic Particle Testing

Magnetic particle testing (MT) is a magnetic flux leakage test that is similar to visual and liquid penetrant testing for the detection of surface defects. In some cases based on certain parameters such as intensity and defect depth, subsurface (i.e. just below the surface) defects are detectable and verified by secondary methods. Testing is conducted on materials that are strongly

attracted to magnetic forces (e.g. ferromagnetic materials). MT methods are based on the principles of magnetic lines of force around a magnet that continuously enter and exit each pole (i.e. north and south). Utilizing this physical phenomenon, a magnetic field is applied to the part under test either by alternating current, half-wave rectified current or full wave rectified current [26]. Defects break the lines of force creating new poles allowing new lines of force to continue creating magnetic flux leakage. Magnetic flux leakage attracts fine magnetic particles applied by either dry or wet methods. The colored or fluorescent particles highlight the defect to aid in detection. The working principles of magnetic particle testing are shown in Figure 9.

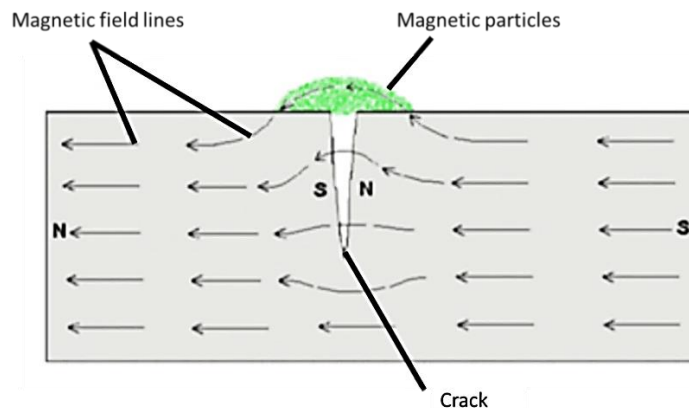


Figure 9: Working principles of magnetic particle testing [27]

2.2.3.1 Applications

Various forms of ferromagnetic materials such as billets, blooms, rods, bars and tubes are most commonly inspected with magnetic particle testing. Application examples include the detection of surface defects in castings, laminations in plates, surface defects associated with welds, internal and external surfaces of pressure vessels and cargo tanks, to name a few [28].

2.2.3.2 Advantages

Both surface and subsurface defects can be detected; otherwise, unnoticed with an unaided eye. Surface preparation is not as critical as other NDT methods. It is a safe, quick and

low cost NDT method that can be conducted portably. Requires minimal training to conduct and interoperate results.

2.2.3.3 Limitations

Materials must be ferromagnetic; therefore, non-ferrous materials such as aluminum, stainless steel, and magnesium are not applicable [28]. A magnetic field must be applied and defects must be perpendicular to the lines of force. Removal of coatings or plating may be required. Materials may require demagnetization prior to use. Only small parts or sections can be inspected at once.

2.2.4 Eddy Current Testing

Eddy current testing (ET) is used to locate surface or subsurface defects in electrically conductive materials by principles of electromagnetic induction. Eddy current testing can be used to evaluate material characteristics such as hardness, heat treatment condition, and a variety of metallurgical conditions [29]. The fundamentals of eddy current testing are based on the change in terminal impedance of the coil due to the primary magnetic field of the coil being brought into proximity of the electrically conductive materials [30]. Alternating currents are applied to the conductor (e.g. a probe usually made of copper wire) simultaneously developing the primary magnetic field. Figure 10 shows the working principles of eddy current in which the primary magnetic field produces eddy currents (i.e. induced electrical currents that flow in a circular path) that then create a secondary magnetic field that is opposed to the primary.

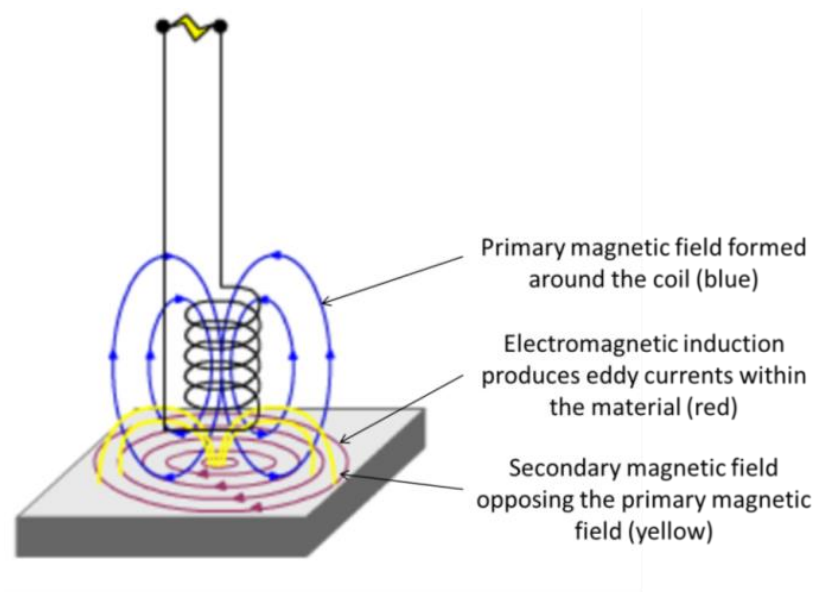


Figure 10: Working principles of eddy current testing [31]

The newly formed eddy currents reduce the inductance of the coil increasing the resistance that is detected by the instrument in which the coil is attached. Changes or disruptions to the eddy currents further reduce the inductance causing more resistance. For example, if a defect is at or near the surface of the material, the eddy currents will be disrupted as they flow around the crack, changing the resistance. The disruption of eddy currents is shown in Figure 11.

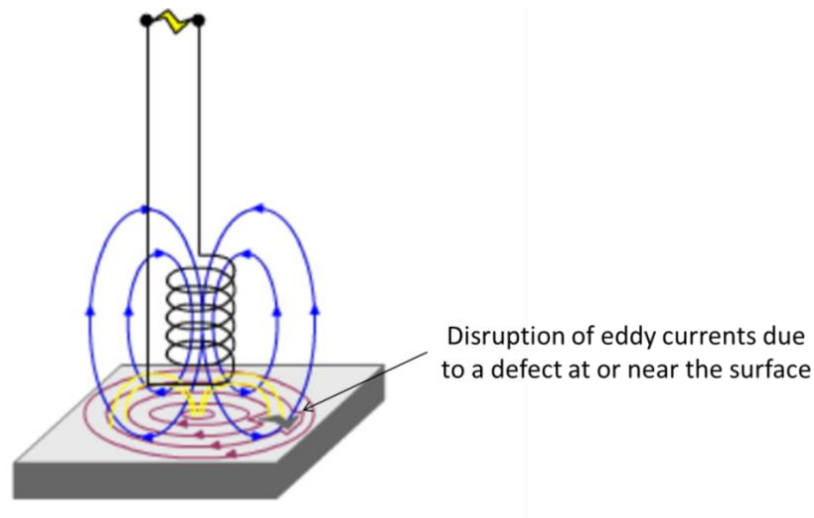


Figure 11: Eddy currents being disrupted by a defect at or near the surface [31]

2.2.4.1 Applications

ET applications include electrical conductivity and resistivity measurements, verification of hardness and alloy, material identification, heat treatments and heat damage, coating thickness and crack detection.

2.2.4.2 Advantages

Numerous applications are possible for electrically conductive materials. ET is sensitive to small cracks at or near the surface providing immediate results. Defects are detectable through thin surface coatings. Conductivity measurements are very accurate. Surface preparation is minimal and equipment is portable and easy to use.

2.2.4.3 Limitations

ET is limited to electrically conductive materials and is susceptible to magnetic permeability changes in ferromagnetic materials. ET is also inadequate for defects orientated parallel to the test surface. Signal responses from discontinuities must be interoperated and validated with reference standards. The depth of penetration is also limited [31].

2.2.5 Radiography Testing

Unlike the previously mentioned NDT methods, radiography testing (RT) is a common volumetric inspection method used to detect internal defects providing a permanent photographic record of inspection via radiograph or digital detector. Penetrating radiation from either an x-ray generator or decaying radioactive isotope is passed through the test object onto a detection source (e.g. film or digital detectors such as photostimuable phosphorous, fluorescent screen, or camera). The ability to penetrate the test object is a function of the wavelength. Penetrating radiation wavelengths are approximately 0.001 to 1 nm for x-ray and 0.01 to 0.0001 nm for

gamma rays. Each provides energies greater than 100 eV as indicated in the following electromagnetic spectrum shown in Figure 12.

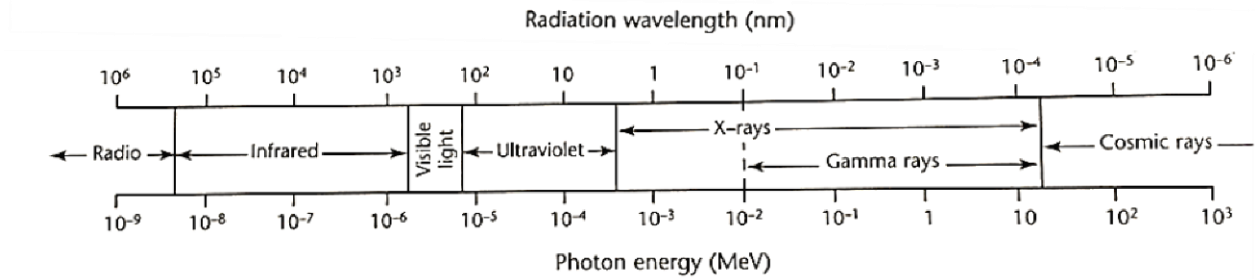


Figure 12: Electromagnetic Spectrum [32]

Upon penetration into the test object, the radiation interacts with the detection source causing ionization (i.e. atoms or molecules that become positively or negatively charged). A radiographic image is produced by the measure of ionization. For film, the radiation must provide enough energy to ionize the film freeing the negative Bromide (Br^-) ions causing interactions with the positive Silver (Ag^+) ions creating a latent (i.e. invisible) image until developed. Similarly, for digital detectors, the radiation interacts with materials that fluoresce upon ionization, creating the image [33].

Defect detection depends on the difference in the physical density of the material and the thickness [34]. An increase in density or thickness contributes to attenuation, reducing the energy and amount of radiation the detection source is exposed too. The result is a lighter image for film and a darker image for digital detectors. Figure 13 shows the working principles of radiography testing in which radiation leaves the anode and is passed through the diaphragm and specimen exposing the film [34]. For example, the dark region of the film below the flaw (i.e. defect) has been exposed to more penetrating radiation. The dark region indicates the flaw is either less dense or has reduced the total overall thickness.

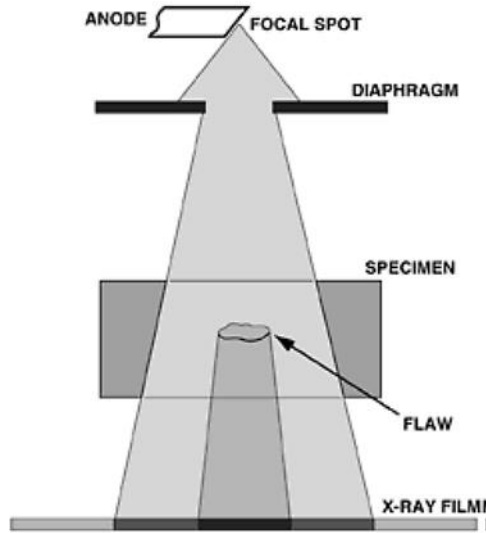


Figure 13: Working principles of radiography testing [34]

For accurate detection, the defect must be orientated parallel to the penetrating radiation limiting its use for defect detection in CFRP materials. The majority of CFRP defects such as delaminations, foreign materials and porosity (i.e. planer distribution between plies) are orientated planer to the surface, perpendicular to the radiation beam. Therefore, detection must be a factor of significant difference in density between the material and defect. Delaminations and planer porosity do not provide enough difference in density compared to defect free areas and are therefore undetectable. Similarly, foreign materials inherent to CFRP manufacturing are of thin polymeric films and most commonly do not provide the required difference in density to be detected.

2.2.5.1 Applications

Primary applications include the inspection of metal castings, welds, piping and tubing, nuclear, aviation and space flight components, electrical components and honeycomb composites [35]. Common detectable defects for applications other than most CFRP laminated composites (i.e. metals, castings, ceramics, honeycomb structures, etc.) include porosity, inclusions, shrinkage, cracks, slag, tungsten, incomplete penetration, oxidation, corrosion, component

placement, terminals, cell wall fractures, node bond separation and foreign material detection of contrasting densities [35].

2.2.5.2 Advantages

RT is a volumetric inspection method that can be conducted on a variety of material types and components providing accurate and permanent records. Inspections can be conducted on a variety of shapes and sizes. RT provides improved sensitivity compared to other NDT methods. Characterization of discontinuities can also be accomplished [36].

2.2.5.3 Limitations

Safety hazards associated with radiation must be made aware of and tested for. Thicknesses may be limited due to attenuation. Accessibility to both sides of the part is required. Detection is dependent on defect orientation or differences in density and most CFRP laminated composite defects are undetectable [36]. RT can be time consuming and requires expensive capital equipment costs. Extensive training and experience is necessary to perform inspections and interoperate results.

2.2.6 Ultrasonic Testing

Ultrasonic testing (UT) utilizes high frequency acoustic waves to inspect and evaluate components providing quantitative results. Most generally, UT techniques are categorized as internal defect detection, thickness evaluation or bond characterization. Each of which can be further subdivided depending on technique [37, 38]. The basic principle of UT is based on solid materials transmitting acoustic waves. Acoustic waves are transmitted and received by the ultrasonic instrument via a controlled electronic pulse that activates the transducer element(s) incased within the search unit or probe. The transducer element is generally made of a piezoelectric ceramic (i.e. smart material) that generates an acoustic wave (i.e. sound wave) in

response to the electronic pulse and vice versa, also known as the piezoelectric effect. When activated, the acoustic wave is transmitted and received by one of three setup configurations such as pulse-echo, pitch-catch or thru-transmission [39]. Pulse-echo utilizes a single sided setup (i.e. placed on one side of the component under test) in which a single probe is used to transmit and receive acoustic waves. Pitch-catch is also a single sided setup that utilizes separate transmit and receive probes. Thru-transmission is a dual sided technique that also uses separate transmit and receive probes placed facing one another on each side of the test object. The pulse-echo, pitch-catch and thru-transmission setups are shown in Figure 14.

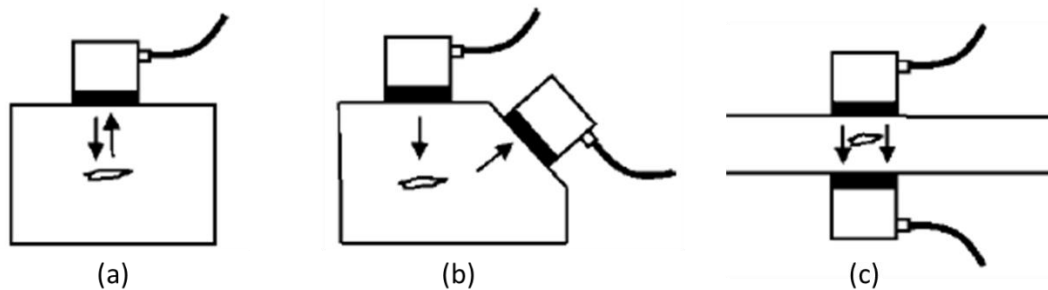


Figure 14: Types of ultrasonic techniques a) pulse-echo, b) pitch-catch and c) thru-transmission [39]

There are four modes in which acoustic waves can propagate in solid materials based on particle oscillation; longitudinal waves (particle vibration parallel to wave direction), shear waves (particle vibration perpendicular to wave direction), surface waves or plate waves (particle vibration perpendicular to the surface) [40]. The two most common wave modes are longitudinal and shear; however, shear waves require acoustically solid materials such as metals and do not effectively propagate in most composite materials [41]. Longitudinal waves are applicable for defects orientated parallel to the test surface such as porosity, voids, delaminations and foreign materials, as well as material thickness and defect depth. Shear waves are applicable for defects orientated other than parallel to the test surface such as defects associated to welded

joints; porosity, slag, lack of fusion, deficient root penetration, and longitudinal and transverse cracks. The direction of particle motion and wave propagation for longitudinal and shear waves is shown in Figure 15.

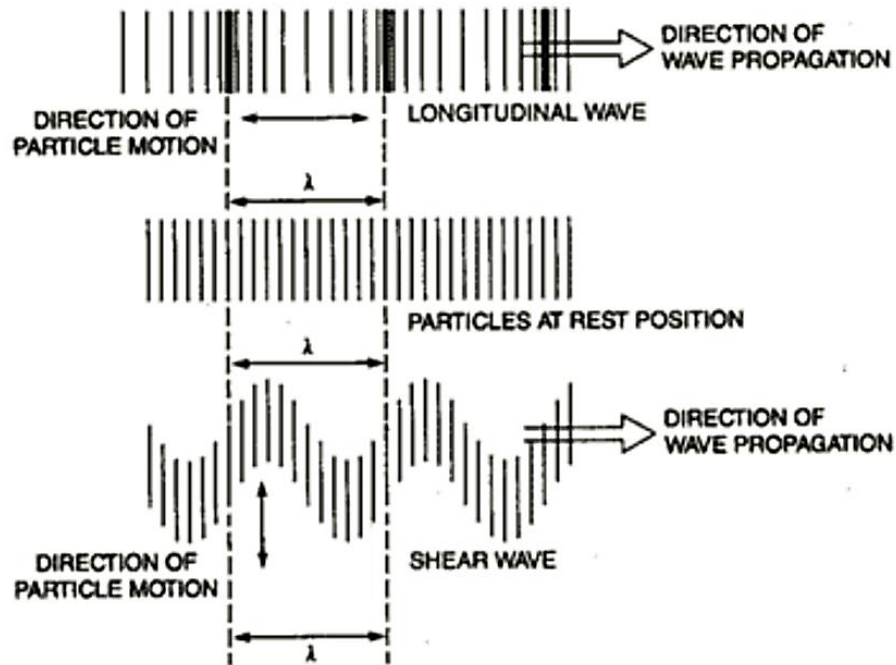


Figure 15: Illustration of particles at rest, longitudinal and shear wave propagation within a solid material [40]

Properties of propagating acoustic waves are based on the wavelength λ , frequency f and velocity v . The wavelength is proportional to the velocity and inversely proportional to the frequency according to equation (2.1) [40].

$$\lambda = \frac{v}{f} \quad (2.1)$$

Acoustic waves are reflected at interfaces such as front and back surfaces of the test object and internal defects. Increasing the frequency results in shorter wavelengths allowing more interactions to occur, significantly improving the probability of defect detection. The shorter the wavelength, the smaller the defect can be detected. As a common practice, defects

must be greater than one-half the wavelength to be accurately detected. Acoustic waves propagate through materials via sound pressure. The tighter the molecules or atoms are elastically bound, the greater the material density (i.e. amount of mass per unit volume) and pressure. Excess pressure allows wave propagation within materials. To determine acoustic wave transmission or boundary reflections due to interfaces or dissimilar materials, the reflection coefficient must be determined based on the acoustic impedance as described in section 1.2. The greater the mismatch, the more energy is reflected at the interface increasing the signal amplitude. In contrast, materials of similar acoustic impedance have reduced signal amplitudes making it difficult to quantitatively differentiate the two.

Ultrasonic frequencies greater than 500 kHz require a couplant placed between the search unit and the test object to allow sound transmission either by contact or immersion (i.e. immersed in a water bath) testing [42]. The couplant must be of a compatible medium that improves the acoustic impedance mismatch between air and the test object allowing more sound energy to enter the test object. The sound energy can be accurately controlled with immersion testing, because the part is fully immersed in the water bath. It is more difficult to maintain coupling with contact testing, while moving the transducer through the couplant placed on the test surface, resulting in variability. However, the efficiency of energy transfer is greater in contact testing, due to less energy reflected back through the water bath [39].

UT establishes three types of displays used to evaluate discontinuities identified as A-Scan, B-Scan and C-Scan shown in Figure 16.

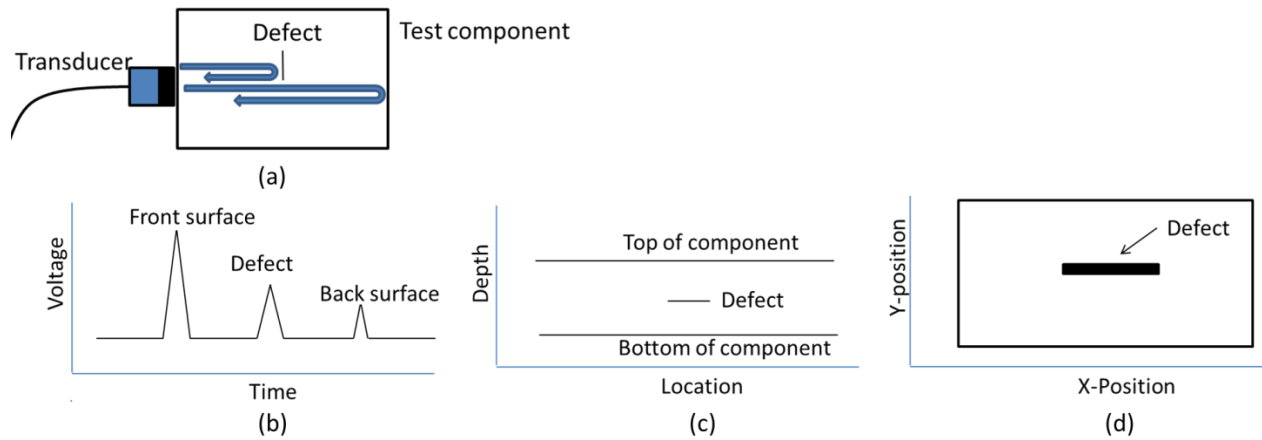


Figure 16: Typical (a) pulse echo system, (b) A-Scan, (c) B-Scan and (d) C-Scan

The most common is A-Scan, which displays electronic signals in analog form from acoustic reflections as voltage versus time on an oscilloscope. The A-Scan display is setup by placing the normal signal reflected from the surface of the part at the initial time and the normal signal reflected from the back surface furthest in time. Generally, reflected signals from defects orientated normal to the surface appear between the front and back while reducing the back surface signal. Defects other than normal appear as much weaker signals or a loss of back surface signal. The B-Scan displays a cross sectional view of the component under test. The location of the defect along the scanning path is illustrated on the x-axis while the depth is illustrated on the y-axis. The C-Scan is generated by moving the transducer in a raster pattern along the x and y coordinates while the position and signals are recorded. The result is a two dimensional planer view from above. The defect size and location is available based on position.

2.2.6.1 Applications

UT is a volumetric NDT method in which most applications are considered as internal defect detection, cross sectional evaluation (i.e. thickness and corrosion testing) or adhesive bond characterization for in-process or in-service materials and products. UT comprises of an assortment of test methods such as pulse echo, angle beam, immersion/modified immersion,

multiple transducer, phased array, lamb wave, guided wave, air coupled and resonance [37]. A large variety of defects can be detected utilizing ultrasonic test methods such as delaminations, voids, cracks, disbonds, variations in thickness, corrosion, corrosion cracking, foreign material, inclusions, weld defects, contamination, density variation, and porosity. A variety of materials can be inspected such as composite materials including CFRP laminates and honeycomb core as well as metals and alloys, ceramics, plastics, and glass [38].

2.2.6.2 Advantages

UT is a quantitative, economical, versatile and useful NDT method. UT offers high speed testing of large and small scale components of numerous material types throughout many industries. Equipment types include digital thickness gauge, automated scanning systems and defect detectors, resonance devices and others. When appropriate techniques are combined with suitable equipment, UT tests are very sensitive for very thick or long sections of all types of materials and bonded assemblies. UT is required by most acceptance criteria allowing for the detection of specified defects with accurate location and size via rapid evaluation; either manual or automated [12-14, 41]. Unlike many NDT methods, UT only requires access from one side of the test object.

2.2.6.3 Limitations

UT methods may be limited to certain test object characteristics such as component geometry (e.g. size, contour, surface roughness, and complexity and defect orientation) and internal structure (e.g. grain size, grain orientation, acoustic impedance differences of joined materials) [37]. Most UT applications require a couplant (i.e. a material used to facilitate ultrasonic energy into the test object, typically water, gel or oil) to eliminate air between the transducer and test object for frequencies higher than 500 kHz. UT instrumentation and

equipment may not be compatible with the test environment (e.g. temperature, radiation levels, electrical interference and others) that may lead to unreliable results. Finally, operators must be highly skilled and trained accordingly to operate equipment and interpret results.

2.2.7 Acoustic Emission Testing

Acoustic emission testing (AE) differs from the preceding NDT methods in two regards. First is the origin of the signal; AE is a passive volumetric NDT method in which the origin of the energy is released from the source within the test specimen rather than from the test method. Secondly, AE ensures structural integrity by monitoring discontinuity initiation and advancement due to deformation in real time to detect active discontinuities [43]. Therefore, AE is most commonly used as an in-service inspection method rather than in-process by monitoring dynamic changes within the material during service.

AE waves are similar to ripples created by a stone that is thrown into a pond. The ripples propagate from the stone (i.e. the source) until they reach the banks. A bobber floating on the surface simulates the sensor which reacts to the ripples by bobbing up and down for extended periods of time compared to the impact of the stone. Figure 17 shows the working principles of acoustic emission testing. As the specimen is stressed by external forces, the source releases energy due to deformation in the form of acoustic waves that propagate through the material. The waves extend to the surface and are received by a nearby sensor that is connected to the detection instrument that analyzes and records the resulting signal.

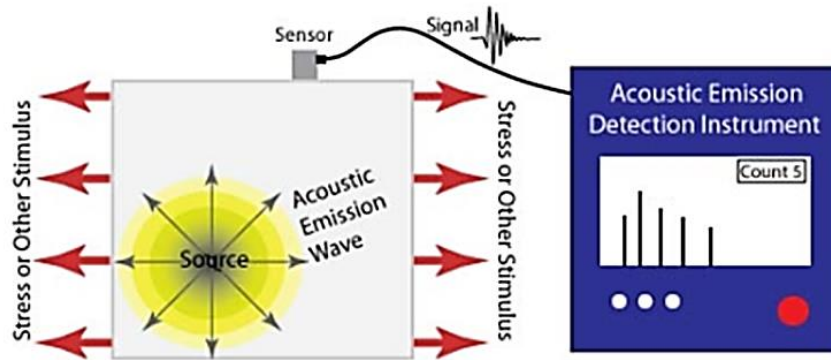


Figure 17: Working principles of acoustic emission testing [44]

There are a variety of mechanisms that generate the source of acoustic emission from applied external stresses. For metals, the energy source originates from indications such as crack initiation and growth, dislocations, slip, sliding of grain boundaries, and fracture. Composite energy sources include delamination and disbond, matrix cracking, interfacial failure, and fiber fracture [43- 45].

2.2.7.1 Applications

A wide variety of structures can be externally stressed and monitored by AE such as metals and nonmetals or any variety thereof (i.e. composites). AE is effective in monitoring CFRP materials in the presence of the primary source mechanism compared to other NDT methods [45]. AE is the most effective in-service method used to monitor materials and characterize failure mechanisms due to active behavior such as cracks, corrosion and hydrogen embrittlement.

2.2.7.2 Advantages

In contrast to other NDT methods, AE is a dynamic test monitoring system used to detect discontinuities and defects within an entire structure during a single test. AE provides accessibility otherwise inaccessible with other NDT methods. AE allows the opportunity to

continue service by monitoring discontinuities until rework or repair is required. AE will detect and monitor active discontinuities preventing catastrophic failures.

2.2.7.3 Limitations

Static discontinuities do not produce acoustic emission signals. Qualitative results are produced; therefore, secondary NDT methods such as UT must be conducted to determine the severity of damage [44]. AE can only contribute to material characterization by monitoring the direction of wave travel, frequency and amplitude of acoustic waves [45]. Material properties, conditions and setup also influence signal responses; therefore, extensive training must be completed to obtain and interpret the results.

2.3 Recent Advances of Non Destructive Test Methods - CFRP Bonded Assemblies

Carbon fiber reinforced polymers (CFRP) are progressively being utilized for structural applications in aerospace and aircraft components slowly replacing traditional metals and alloys due to the ability to further tailor certain properties while maintaining or reducing weight. It is important to note that CFRP defects differ from traditional metals and must be accounted for. These defects include foreign materials (i.e. backing film or peel ply, etc.), delamination, porosity, impact damage and disbonds [46]. From a manufacturability standpoint, large CFRP structures may be fabricated and assembled as smaller sections through bonding techniques. Subsequently, bonding techniques and processes provide the capability to manufacture large final structures that would have otherwise been difficult due to accessibility to large curing facilities. The bonds between CFRP assemblies are interfacial bonds (i.e. held together by intermolecular forces) between the adherend and the adhesive and are essential to the overall joint strength [47]. However, adhesive bonding techniques are inherent to several types of defects that can reduce the overall joint strength [46, 47]. Bondline defects occur either within

the adhesive or the adherend-adhesive interface and are generally categorized as foreign material, disbond, voids or kissing bonds as shown in Figure 18.

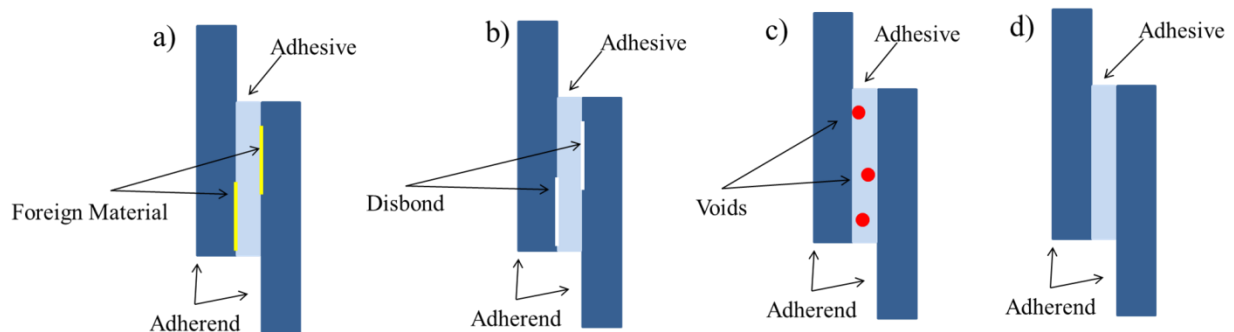


Figure 18: Bondline defects a) foreign material, b) disbond, c) voids, d) kissing bond

Each of these defects is most commonly attributed to poor preparation, inclusion of foreign material or inadequate assembly techniques. While procedures are in place to overcome these issues, appropriate NDT methods must be in place to detect and distinguish defects during the manufacturing process. Therefore, in-service monitoring NDT methods such as structural health monitoring (SHM) [48- 50], acoustic emission (AE) [51, 52], and guided wave inspection (GWI) [48, 53, 54] will be omitted. The following sections review recent advances of in-process NDT methods applicable to the inspection of CFRP bonded assemblies.

2.3.1 Laser Bond Inspection

Laser Bond Inspection (LBI) has been specifically designed for the inspection of CFRP bonded assemblies and scarf repairs. A high energy pulsed laser beam is applied to the surface of the assembly creating a mechanical stress wave that propagates through the composite material to the bonded interface. The mechanical wave applies stress to the bond resulting in a test of relative strength. If the bond is substandard (i.e. below designed strength) resulting from insufficient surface preparation or foreign material, LBI identifies the associated defects [55-57]. Alternatively, strong bonds are unaffected.

Part preparation is conducted by applying a thin light absorbing material to the surface and then a thin layer of water must be poured over the material. The laser is passed through the water and absorbed by the opaque material. An ionized gas (i.e. plasma) is created and is temporarily contained by the water. During containment, the stress wave intensifies permitting transmission through the material to the bondline. The results are correlated to the bond strength by the Fluence Number (i.e. optically delivered energy per unit area). The energy and diameter of the laser pulse can be varied to establish the desired strength of the stress wave depending on application [55]. A diagram of the process is shown in Figure 19.

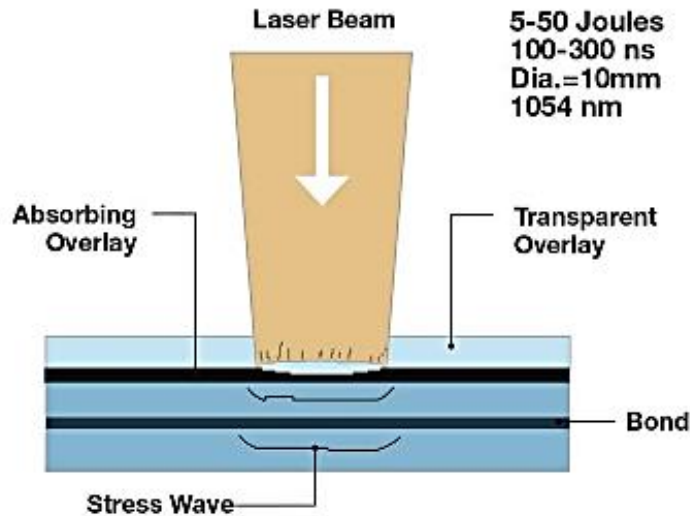


Figure 19: Overall Laser Bond Inspection (LBI) process [56]

Recently a test was conducted comparing LBI with UT using a composite-to-composite adhesive interface [56]. The results of the comparison are shown in Figure 20. It was concluded that LBI detected a bond failure at 5.6 J/cm^2 , while UT marginally detected the same failure. The failure was secondarily inspected by ultrasonic A-Scan verifying the marginal indication.

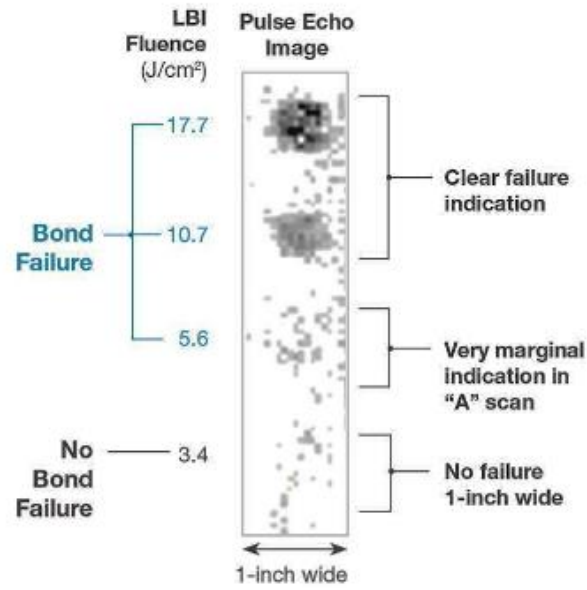


Figure 20: Results comparing Laser Bond Inspection (LBI) fluence (J/cm^2) to ultrasonic testing (UT) of a pulse echo C-Scan image [56]

2.3.1.1 Applications

LBI has been specifically designed for the detection of bondline defects such as foreign material, disbonds, voids and kissing bonds in a variety of composite assemblies and scarf repairs. Complex geometries and assemblies are easily inspected. LBI can be used during initial manufacturing processes as well as subsequent inspections throughout [57].

2.3.1.2 Advantages

LBI inspection processes can be performed in all types of environments on numerous joint configurations such as composite to composite, metal to composite and metal to metal [57]. LBI provides quantitative strength measurements identifying weak bonds otherwise undetectable with conventional NDT methods.

2.3.1.3 Limitations

LBI systems are relatively expensive compared to alternative NDT methods. The surface of the test object must be prepared with a light absorbing material. Water must be applied to the

surface in conjunction with the laser during the inspection. Safety protocols must be in place for the use of lasers. LBI is a relatively slow inspection method compared to UT with arrays.

Currently, LBI inspections are limited to structures that are less than 1 inch thick. There is an unknown amount of damage applied to the bond during inspection and may need to be verified with UT.

2.3.2 Infrared Thermography Testing

Infrared Thermography Testing (IRT) is a non-contact NDT method, which can be classified as either a passive or active method [58 -62]. Both methods use external heat sources (e.g. heat gun, halogen lamps, etc.) to stimulate the part surface increasing the temperature allowing for the detection of variations in thermal emissivity (i.e. material(s) ability to emit thermal radiation) by an infrared (IR) camera. Each material type including trapped air provides a unique thermal emissivity [59]. IRT provides a visual display of infrared energy emitted or transmitted by the material(s). The presence of a defect will change the path and heat flow within the test object, resulting in a disparity of thermal emissivity [60]. The passive approach provides a qualitative temperature profile of the part surface, based on differences between areas that react to the heat source and the surroundings. Passive approaches typically do not provide sufficient temperature contrasts between surface and subsurface defects [58]. Active approaches utilize external heat sources to actively create a significant thermal contrast between suspect and good areas allowing subsurface detection via thermal diffusivity during the transient phase [61]. Known characteristics such as bandwidth and time duration of excitation allow for quantification of subsurface defects either quantitatively or qualitatively. The most common active thermography applications are shown in Figure 21.

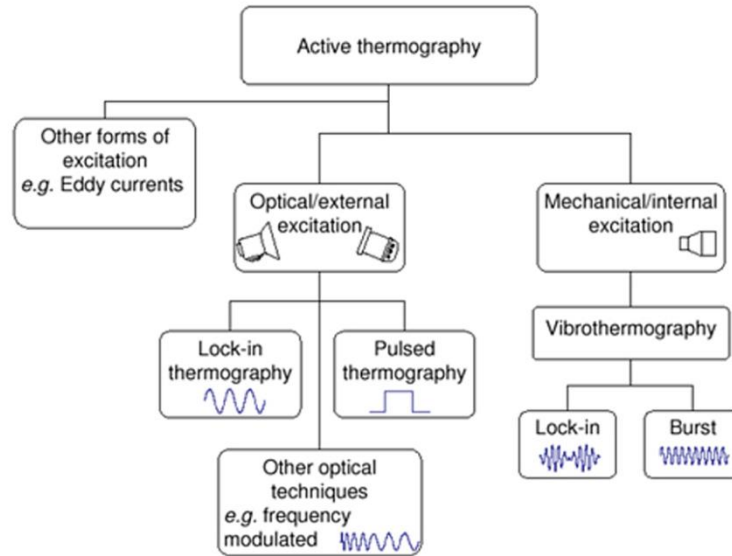


Figure 21: Flow chart illustrating the different active thermography approaches [61]

Recently active methods such as pulsed heating [62- 64], step heating [65] and lock-in thermography (LT) [66, 67] have been used to evaluate and characterize bonded joints in composite materials. The following is a review of lock-in thermography based on the ability to provide more inspection details and image definition at greater depths in CFRP materials compared to other IRT methods [68].

2.3.3 Lock-In Thermography Testing

Lock-in thermography testing (LT) methods are active methods that apply the external heat source at a single “lock-in” frequency, periodically controlled, heating the surface of the test object. The heat generates thermal waves that propagate longitudinally through the thickness of the article via temperature gradient-induced heat conduction [66]. The thermal infrared emission at the surface is monitored and recorded by an infrared (IR) camera. The resulting wave is reconstructed by measuring the progress of temperature differences in amplitude and phase changes at the surface [67]. The phase shift ϕ based on depth (z) can be defined by equation (2.5), where λ is the frequency wavelength and μ is the thermal diffusion [67].

$$\phi(z) = \frac{2\pi z}{\lambda} = \frac{z}{\mu} \quad (2.5)$$

According to equation (2.6) the thermal diffusion μ can be calculated in which ω is the modulation frequency, α is the thermal diffusivity, c_p is the specific heat constant, ρ is the density, and k is the thermal conductivity [67].

$$\mu = \sqrt{\frac{2k}{\omega\rho c_p}} = \sqrt{\frac{2\alpha}{\omega}} \quad (2.6)$$

Recently, Palumbo Davide et al. [67] evaluated the bondline of composite adhesive lap joint samples exposed to hygrothermal aging (i.e. form of environmental conditioning) with lock-in thermography. The tests were performed with a Flir 640 IR camera with a thermal sensitivity of <30mK. The setup is shown in Figure 22.

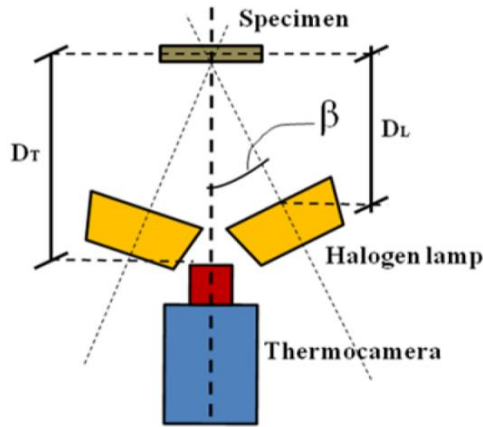


Figure 22: Top view of the setup used for lock-in thermography of composite lap shear samples ($\beta = 30^\circ$, $D_T = 30\text{cm}$, $D_L = 20\text{cm}$) [67]

The test was conducted on one side of each lap joint specimen to detect the initial bonded interface, prior to mechanical testing. Each specimen consisted of the same adherend and adhesive thickness of 2.5mm and 0.76mm, respectively. For reference, a Teflon foil insert was

placed between the bonded interfaces, simulating a disbond. A total of 12 lap joint specimens were identified by VA and followed by the lot number to determine the magnitude of debonding adjacent to the Teflon insert prior to and after aging. Test sample VA0 was used to determine the optimum frequency of 0.0125 Hz, based on absolute phase angle $|\Delta\phi|$ (deg) vs. frequency (Hz) shown in Figure 23. Figure 24 show the resulting phase images of the test sample VA0 along with sequential test specimens VA01 – VA12. Black areas indicate debonding and green lines represent areas of interest (i.e. discontinuity) due to partial debonding.

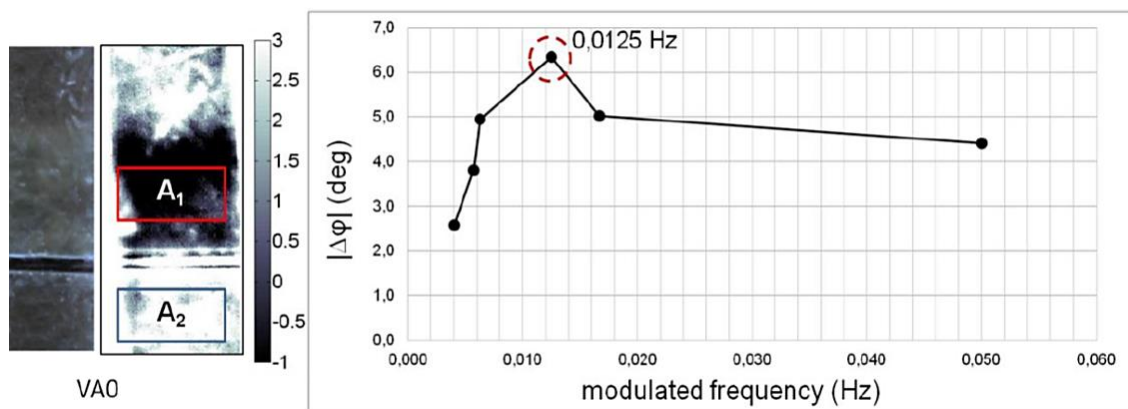


Figure 23: Maximum phase angle by testing carried out on specimen VA0. A₁ and A₂ represent defect and defect free areas, respectively, to determine phase angle [67]

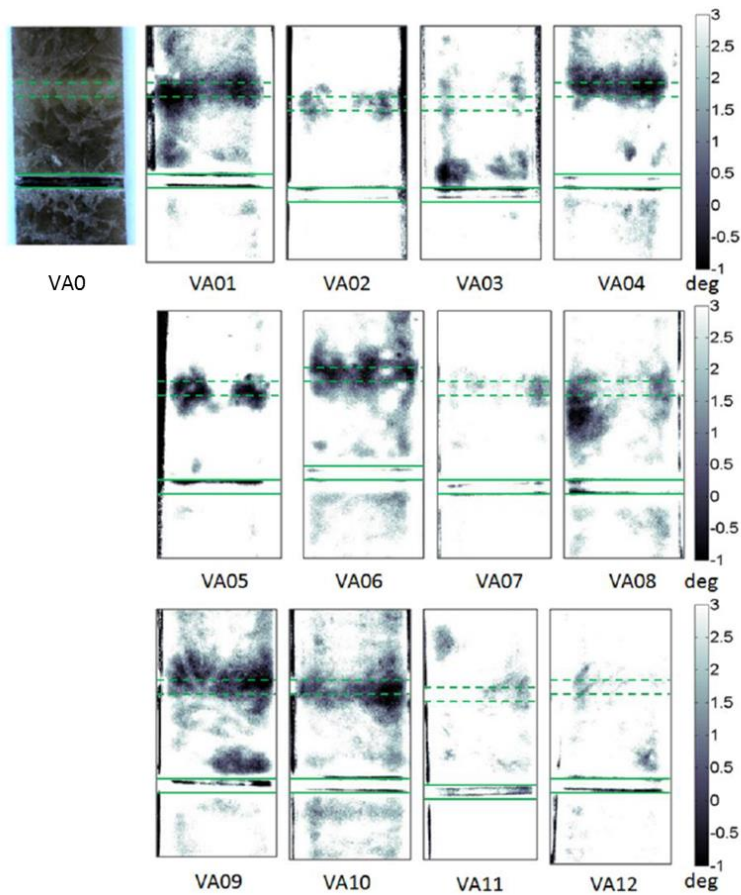


Figure 24: Phase image results, based on optimum frequency of 0.0125 Hz obtained by test specimen VA0 and sequential test specimens VA01 – VA12, where black areas indicate debonding and green lines represent areas of interest due to partial debonding [67]

Results concluded lock-in thermography’s ability to identify bondline defects caused by exposure to environment or manufacturing processes via hygrothermal aging processes [67]. Verification and correlation of the results was conducted with UT. Quantitative analysis was conducted to identify bondline defects based on a predetermined threshold. It was proven that the LT results were in agreement with the UT results.

2.3.3.1 Applications

Both IRT and LT methods provide the ability to reliably detect a variety of defects in adhesively bonded joints [62-69]. Depth profiles of thermal conductivity or diffusivity can be measured on CFRP materials. CFRP coating thickness measurements such as variations and

wear can also be determined. Moisture can be validated during in-process or in-service applications.

2.3.3.2 Advantages

IRT and LT are single sided non-contact surface inspection methods in which large area surfaces can be inspected simultaneously. Small thermal emissivity differences of materials are easily detectable providing exceptional foreign material and delamination detection. Phase and modulation images are available with frequency processing. Numerical modeling such as slope derivatives due to emissivity are easily conducted and interpreted. The main advantage LT has over IRT is that a single optimum frequency can be locked in based on the phase angle allowing for greater definition at greater depths [67, 68].

2.3.3.3 Limitations

IRT and LT require thermal perturbation of the part surface through external heat sources. Cooling losses due to convection can cause contrasting results and must be accounted for. Active processes require uniform heating, which may be difficult to achieve. Subsequent mathematical analysis may be required to provide necessary quantitative analysis. Observable defects are generally shallow; therefore, material thickness is limited compared to other volumetric NDT methods such as UT.

2.3.4 Digital Shearography Testing

Digital Shearography Testing (DST) measures the in-plane and out-of-plane derivatives of surface deformations of the test object under mechanical stress. The shearing interferometer (i.e. shearography camera) captures the interferometric (i.e. diffuse surface reflections) image and delivers resulting phase change information of the gradient of interfering light waves [70]. First, an interferometric image of the test object surface is acquired prior to being stressed. The

surface is then stressed by thermal, vacuum or dynamic loading, nondestructively, to intensify deformations around any defect. A second interferometric image of the surface under stress is then acquired and compared resulting in the shearogram (i.e. digital image depicting differences in gradients of the surface). The shearogram is similar to a topography map in which the defects can be measured based on peak amplitude [71]. DST offers measurable surface strains via surface displacements to aid in the detection of CFRP defects such as delaminations, disbonds, impact damage and thickness variations [73, 74]. However, most of the literature reviewed only referred to detecting disbonds between the CFRP face sheet (≤ 0.078 inches thick) and honeycomb or foam core assemblies [75, 76]. A schematic layout of the principle of digital shearography is shown in Figure 25.

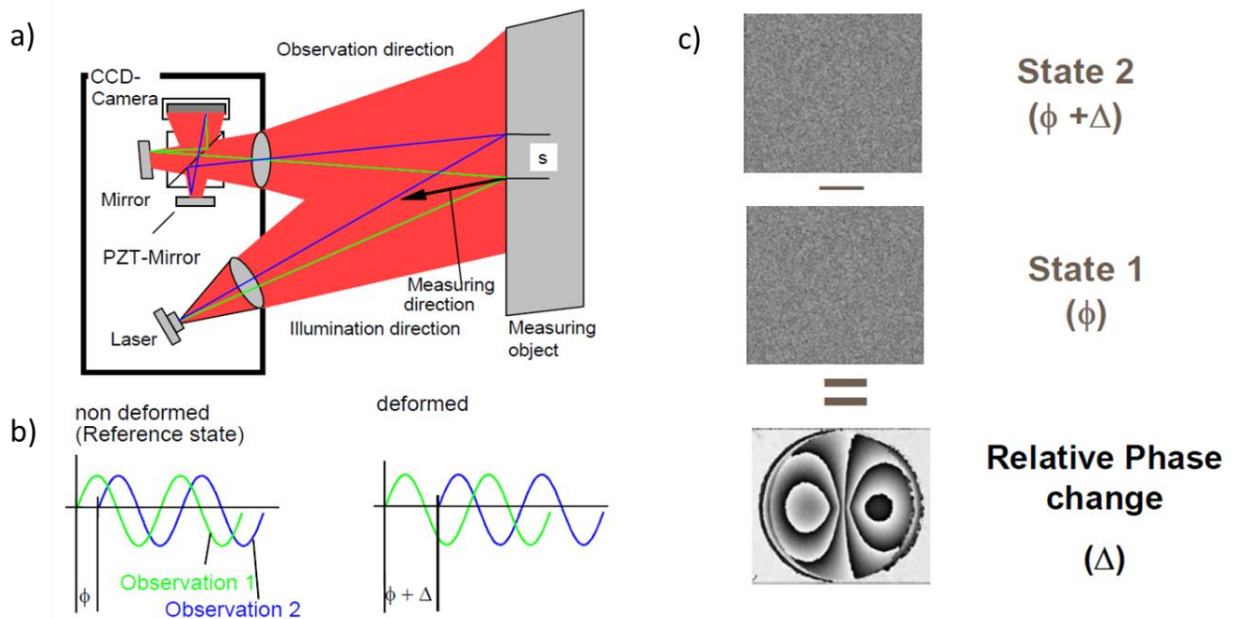


Figure 25: Schematic layout of the working principles of digital shearography a) working principles of the system, b) non deformed and deformed observations (1 and 2) of the acquired analog signals, c) digital interferometric images (state 1 and state 2) with the resulting shearogram (relative phase change) [72]

Recently, De Angelis G. et al. [77] documented the investigation of a disbond due to impact damage in an air cooled inlet CFRP assembly. A photo of the assembly and disbonded region between the composite local stiffener and composite external skin is shown in Figure 26.

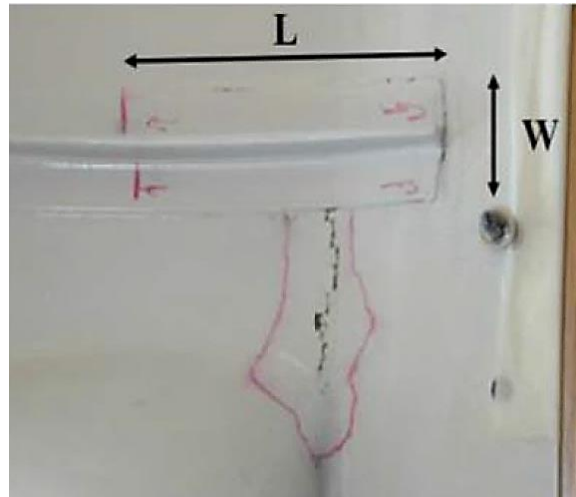


Figure 26: CFRP air-cooled inlet (top view) illustrating the cracked region and the length and width of the disbond between the local stiffener and external skin [77]

The flange thickness of the stiffener was not documented; however, flat bottom hole (FBH) standards from 0.067 inches to 0.157 inches were used to validate the test. This concludes the flange thickness did not exceed 0.157 inches. UT was conducted to validate the disbond prior to DST. The method of dynamic (piezo shaker up to 20 kHz) and thermal (650W fan-less halogen lamps) loading was used to conduct the DST. To ensure coverage, it was necessary to move the piezo shaker to six different locations (a-e) to complete the dynamic loading inspection shown in Figure 27. Based on the figure, it was unclear where the piezo shaker was located in locations b, c and e. Figure 28 shows the imposed stress vibration field and the localized complex fringe pattern affected by the difference in bending stiffness between the bonded (A, B and C) and disbonded (D) interfaces.

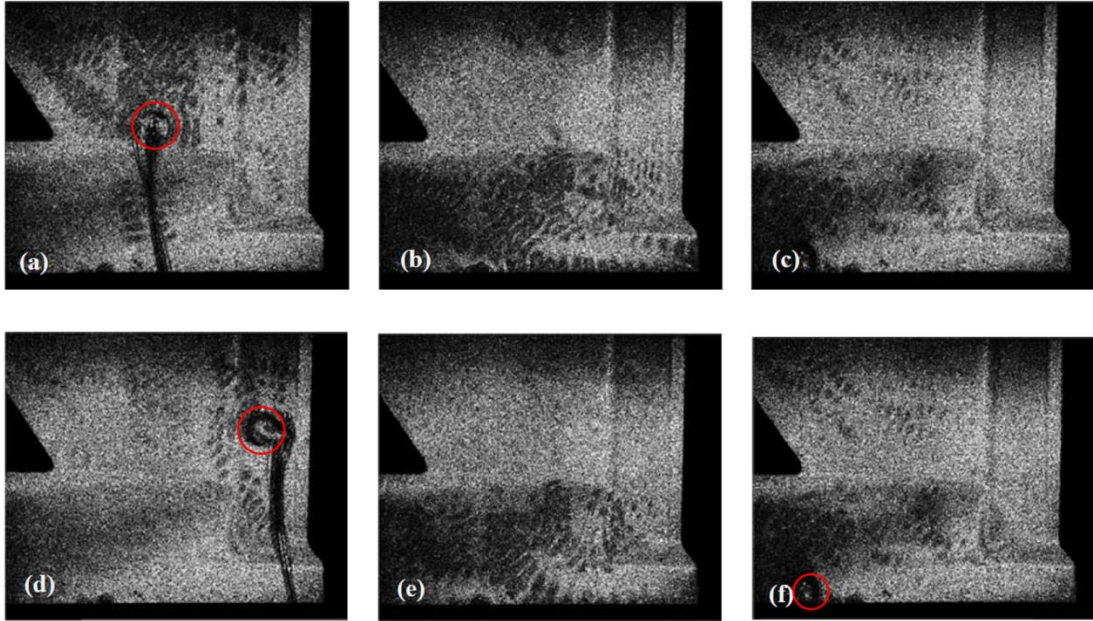


Figure 27: Shearogram with Piezo shaker placement on the inspection surface at six different locations a-f [77]

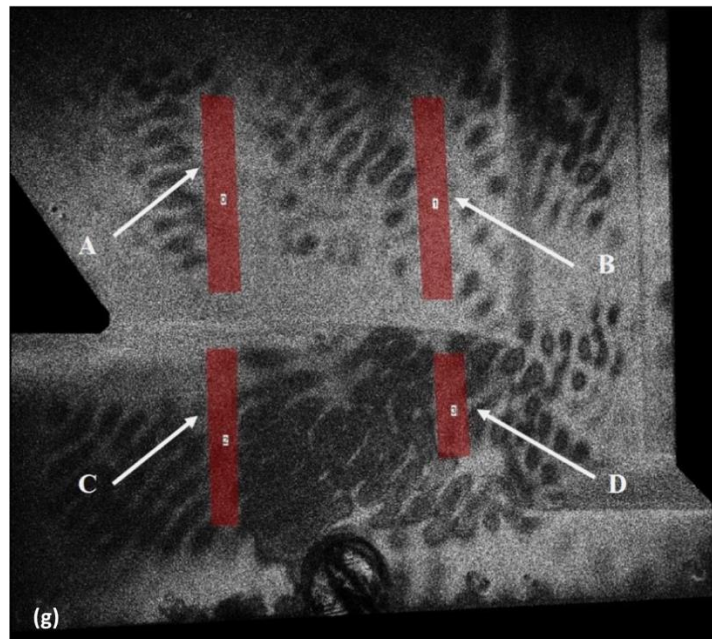


Figure 28: Shearogram illustrating the imposed stress vibration field and localized complex fringe pattern for regions of interest (ROI) reinforced by bonded stiffeners (A, B, and C) and disbonded ROI (D) [77]

Thermal loading was applied to inspect a larger area reducing the need for multiple loading locations. The thermal loading shearogram results are shown in Figure 29. Shearograms a) and b)

are the resulting inspection conducted from the back surface of the composite assembly while c) is the result from the external surface. Local differences in displacement gradient were due to local changes in heat flow revealing the disbond shown in shearograms b) and c). The thermal loading technique was more feasible than dynamic loading, while disbonds were recognized almost instantly [77].

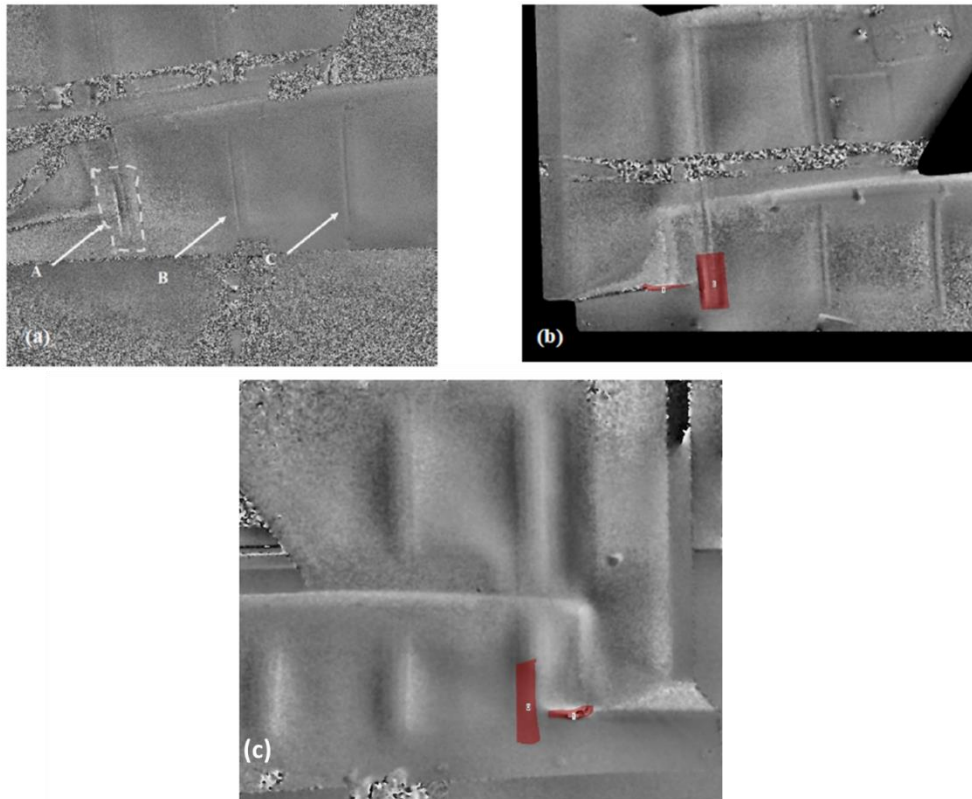


Figure 29: Shearograms of thermal loading inspections from (a) and (b) the back surface of the composite assembly, as well as from (c) the external surface. The revealed disbonded stiffener is highlighted in shearograms (b) and (c) [77]

The results conclude that DST is capable of detecting disbonds in thin (≤ 0.157 inches) CFRP assemblies. However, the results are qualitative pictures of features and surface anomalies verified with UT. Quantitative DST results such as defect size, area, and depth and material deformation vs. loading was not provided. Furthermore, additional equipment is necessary to determine surface derivative slope changes for further analysis, if required [74].

2.3.4.1 Applications

DST provides either portable or large area (i.e. gantry system) noncontact inspection solutions for the detection of delaminations, disbonds, cracks, and impact damage, strain and modulus changes. DST can be used to measure surface deformation to an applied load as well as derivatives of surface displacements as strain results. DST also offers a high speed low cost inspection method for quality assurance, material optimization and manufacturing process control [74].

2.3.4.2 Advantages

DST is sensitive to in-plane and out-of-plane surface displacements through non-contact inspection. DST can be performed over a large area compared to other NDT methods and can be automated for production applications. DST can detect defects at early stages within the manufacturing process and is also applicable to in-service inspections. Extensive technical experience is not necessary to operate the equipment.

2.3.4.3 Limitations

Surface conditions such as glossiness interfere with DST inspection skewing the results. Consequently, surface dulling agents may be necessary for accurate inspections. Surfaces must be mechanically stressed to reveal defects that may lead to unwanted stress. Surface and subsurface defects are detected as surface displacements; DST does not provide the ability to accurately size or determine the depth of subsurface defects. Material thickness is limited compared to other volumetric NDT methods. Additional equipment is necessary to determine quantitative results and is limited to qualitative observations providing descriptive results.

2.4 Ultrasonics and Optimization

There are many volumetric NDT methods capable of detecting discontinuities in CFRP materials. However, not all discontinuities that are detected by NDT methods are considered unacceptable. Acceptance criteria have been established based on destructive testing to determine the minimum requirements, such as discontinuity type, size and depth location that significantly reduce the performance of the material. Any discontinuity that does not meet the acceptance criterion is defined as a defect and is deemed rejectable. To be effective, appropriate NDT methods are identified based on the ability to meet acceptance criterion requirements. Ultrasonic testing has been specified as the most effective NDT method capable of complying with CFRP acceptance criterion requirements [12-14, 19, 41, & 74]. Ultrasonic testing is also the most effective NDT method used to meet bondline acceptance requirements and is often used as the baseline to alternative methods [47, 49, 62, 67, 68, 70, 73, 77-81]. Therefore, in this study all testing will be conducted with ultrasonic pulse echo and full digital waveform acquisition for post processing analysis. Amplitude (i.e. attenuation levels of the peak signal in decibels) C-Scan information along with digital A-Scan will be used for data interpretation.

2.4.1 Ultrasonic Transducer

The array transducer selected for this application was manufactured by General Electric Inspection Technologies; a 4 inch, 2.8 MHz array of 64 elements (i.e. 1D single row of 64 elements) with a 0.0629 inch pitch (i.e. the center distance between each element) and water bubbler shown in Figure 30. The array probe specification is included in Appendix A.



Figure 30: Array transducer with a water bubbler manufactured by GE Inspection Technologies

Ultrasonic arrays consist of multiple single elements (i.e. small individual transducers) epoxied together to form either a 1D linear array or a 2D matrix array. Arrays are electronically controlled to either send or receive ultrasonic signals, individually or as an active group of apertures (i.e. group of elements that are controlled simultaneously) that can be steered, scanned, swept and focused [37]. The element pitch is the distance between the centers of each element. The smaller the pitch the more sensitivity and resolution. An illustration of the working principles of an array is shown in Figure 31. Each element produces independent sound fields similar to one single element probe as shown in Figure 32.

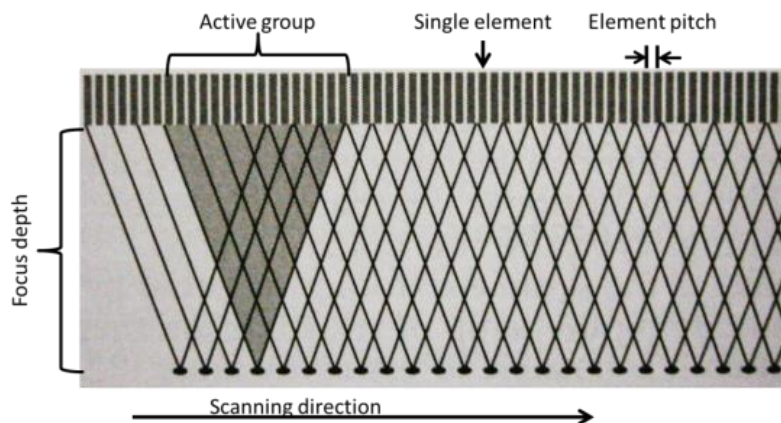


Figure 31: Working principles of a 1D focused linear array transducer utilizing an active group of elements electronically focused to a specific depth and scanned horizontally [37]

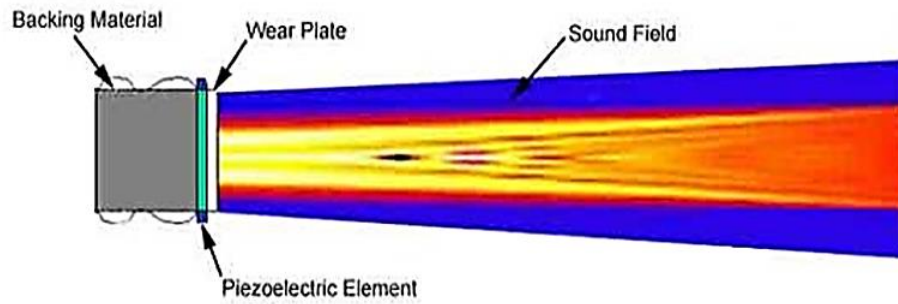


Figure 32: Single element transducer and the ultrasonic sound field that is produced [40]

The final ultrasonic wave front is created by constructive or destructive interference of the individual ultrasonic waves from each element. Figure 33 shows an illustration of the transducer array with the initial ultrasonic waves from each element resulting in the final wave front due to constructive interference.

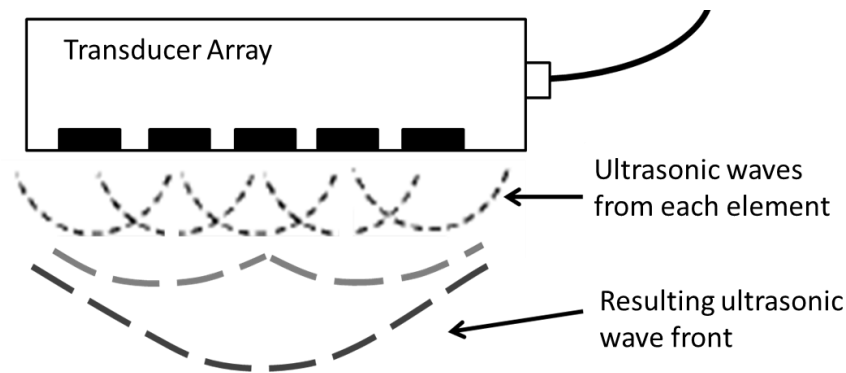


Figure 33: Illustration of the transducer array

Ultrasonic scanning with arrays is much faster than conventional single element probes, providing improved coverage [37]. Sensitivity and resolution is also improved due to the size of each individual element and the pitch between each center. Ultrasonic arrays also offer much more flexibility; therefore, setups can be changed quickly, depending on the application [37].

2.4.2 Ultrasonic Frequency

Most commonly CFRP laminated composites and bonded assemblies are ultrasonically inspected at frequencies greater than 500 kHz in regards to sensitivity and depth [73]. Lower frequencies between 500 kHz and 2.25 MHz allow for more penetration in the material. Higher frequencies between 15 MHz and 25 MHz provide greater sensitivity with reduced penetration [40]. As previously discussed, out-of-autoclave CFRP materials are manufactured at reduced pressure and temperature compared to autoclave cured materials resulting in less compaction and more volatiles. The result causes attenuation and unwanted noise (i.e. reflections and scattering) of the ultrasonic signals at higher frequencies, further limiting penetration and wave propagation. Also, under consideration is the infinitesimal acoustic impedance difference between peel ply and the cured film adhesive (i.e. bondline); higher frequencies are more sensitive, improving differentiation. Selecting the correct frequency requires a compromise between lack of penetration and attenuation due to noise that increases with frequency and sensitivity that decreases with frequency [78]. Based on the considerations, a central frequency of 2.8 MHz was selected for the inspection of the fabricated reference standard to achieve the final results.

2.4.3 Signal Optimization

Boeing Automated Systems Group (BASG) provides digital waveform acquisition, storage and analysis tools permitting detailed real-time and post-acquisition analysis of received RF signals in digital format. To improve the reliability of the ultrasonic inspection the digital waveform will be acquired and post processed with user defined algorithms (developed by BASG) in an effort to satisfy the specified 3:1 SNR.

CHAPTER 3

METHODOLOGY

This chapter elucidates to the method used to develop the reference standard, ultrasonic system setup and inspection of the standard. The manufactured reference standard is a representation of the configuration and complexity of the part to be inspected. Reference standards are utilized to properly perform the initial setup prior to the inspection, to ensure accuracy of the system and reliable defect detection. The following system setup was configured with the appropriate parameters to ensure accuracy of the ultrasonic inspection of the standard.

3.1 Reference Standard Materials

Each of the materials selected for the reference standard construction are designed for Out-of-Autoclave (OoA) applications for primarily structural components.

3.1.1 Out-of-Autoclave Fabric Substrate

Figure 34 depicts the OoA fabric substrate; a prepreg CFRP material which includes a toughened epoxy resin system with an 8 harness satin weave (8HS) carbon fabric. Figure 35 shows the pattern of the 8HS. The epoxy resin system was designed for the use of OoA prepreg materials and can be cured at lower temperatures producing quality components for structural applications.



Figure 34: OoA fabric substrate – prepreg CFRP of 8HS fabric

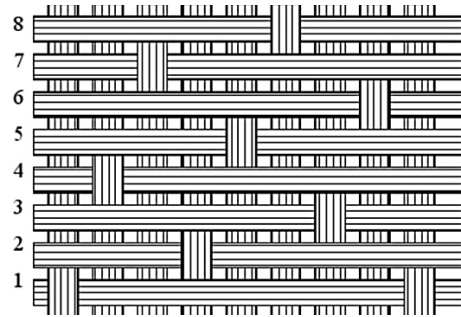


Figure 35: Pattern of an 8 Harness Satin Weave Fabric [82]

3.1.2 Out-of-Autoclave Fabric Preform

Figure 36 shows the OoA fabric preform; a carbon based 3D multilayer woven fabric similar to the material shown in Figure 37. The same epoxy resin system that was incorporated into the prepreg substrate was heated and injected into the 3D woven fabric and oven cured via resin transfer molding (RTM) completing the preform.

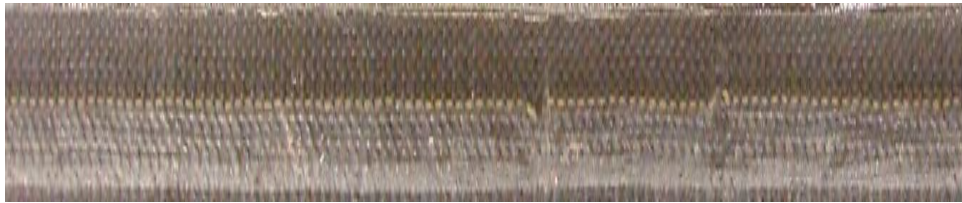


Figure 36: OoA fabric preform – oven cured 3D woven multilayer fabric



Figure 37: 3D multilayer woven fabric [83]

3.1.3 Peel Ply Inserts

Figure 38 depicts the material used as the peel ply inserts between the film adhesive and the OoA fabric preform; a non-porous Polytetrafluoroethylene (PTFE) coated plain weave fiberglass cloth which allows for easy removal pre or post-cure.

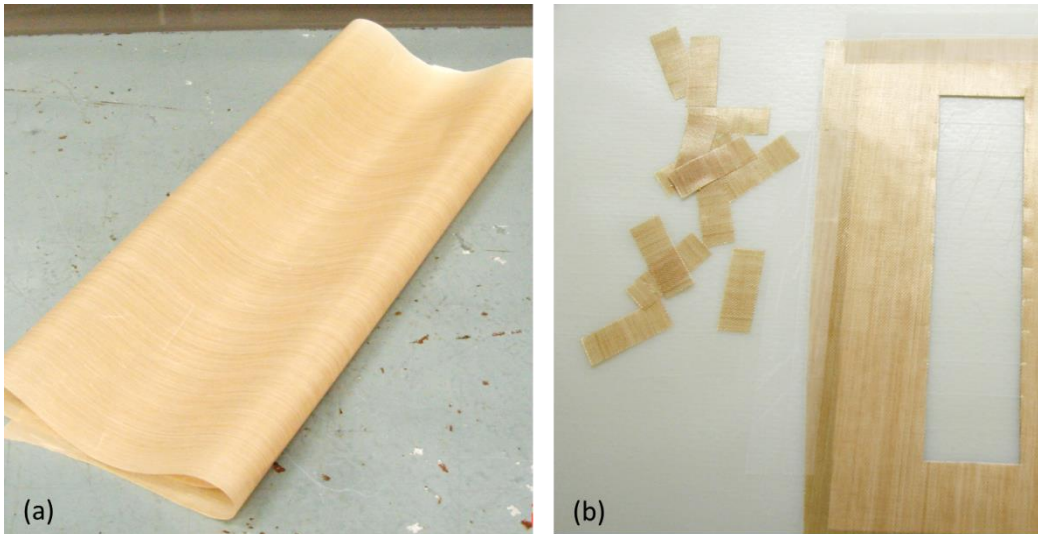


Figure 38: PTFE-coated plain weave fiberglass a) cloth and b) inserts

3.1.4 Film Adhesive

The film adhesive used to bond the substrate to the preform has been designed for co-cured, co-bonded or secondary bonding applications and is compatible with both the substrate and preform.

3.2 Reference Standard Assembly

Both OoA fabric substrate and OoA fabric preform were laid up and cured per manufacturer specifications. The OoA fabric substrate was then machined to 32 inches long by 12 inches wide, represented in Figure 39. Once cured, the peel ply was removed from the substrate and the film adhesive was centered and placed, represented in Figure 40. The 8 peel ply inserts (4 @ 0.250 x 1.00 inches and 4 @ 0.375 X 1.00 inches) were then placed at specific locations atop the adhesive represented in Figure 41. The peel ply was then removed from the

top substrate and place atop the peel ply inserts encompassing the film adhesive represented in Figure 42. An exploded view of the reference standard is represented in Figure 43. The assembly was then bagged and cured per the film adhesive manufacturer specifications for secondary bonding applications. The peel ply inserts were intentionally left extended beyond the bonded interface for visual reference shown in Figure 44.

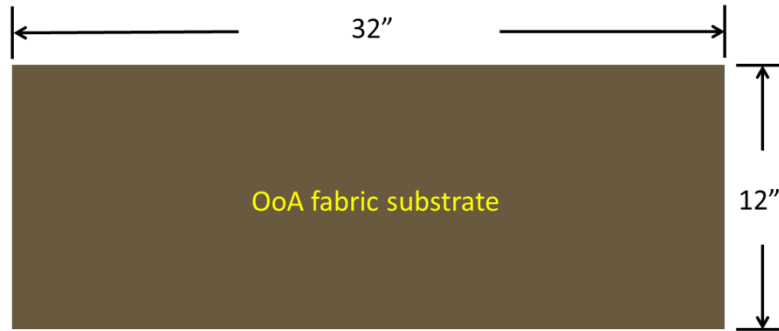


Figure 39: Representation of the OoA fabric substrate and dimensions

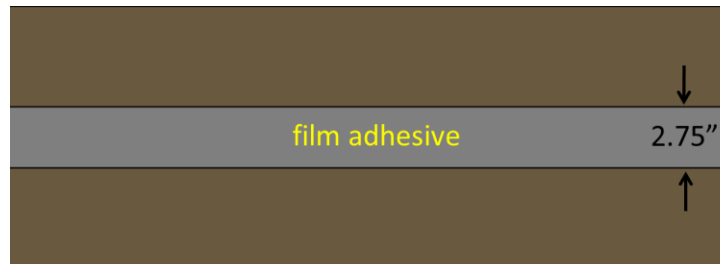


Figure 40: Representation of the film adhesive placed atop the OoA fabric substrate

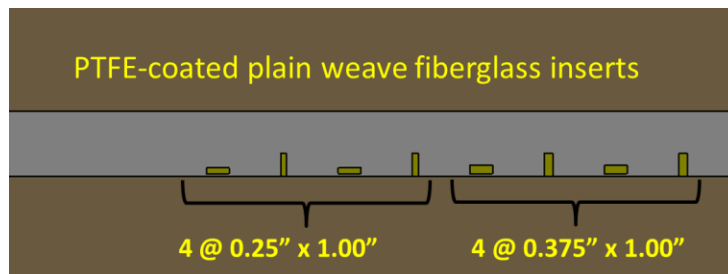


Figure 41: Representation of the peel ply insert locations and dimensions placed atop the film adhesive



Figure 42: Representation of the OoA fabric preform placed atop the peel ply inserts

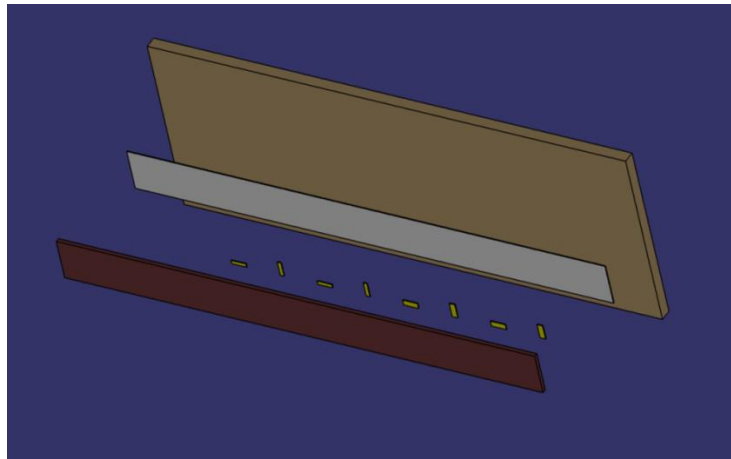


Figure 43: CAD model illustrating the reference standard in an exploded view

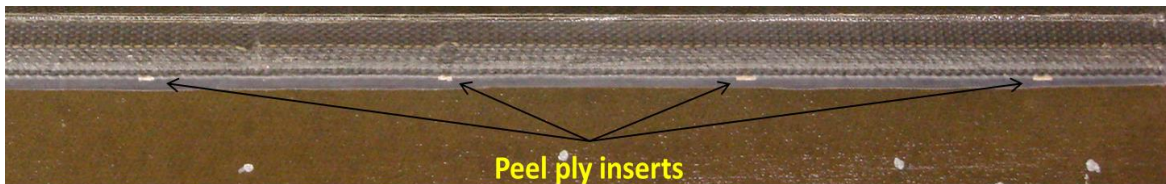


Figure 44: Peel ply inserts extended beyond the fabric preform for reference.

3.3 Ultrasonic Setup and Inspection of the Reference Standard

Once the standard assembly was complete, the ultrasonic parameters were setup using the standard as a reference. The reference standard was then ultrasonically inspected with the Automated Ultrasonic Scanning System Generation Seventeen (AUSS XVII), manufactured by the Boeing Company.

3.3.1 Ultrasonic System Details

The AUSS XVII is an ultrasonic pulse echo inspection system designed for phased array inspection applications with the selected array transducer. The water bubbler system was incorporated within the housing surrounding the transducer to apply a thin film of water as the couplant medium between the transducer and the reference standard. Figure 45 is an illustration of the overall system. Figure 46 shows the array setup atop the reference standard (i.e. on the OoA fabric substrate side) to establish the ultrasonic parameters prior to inspection.

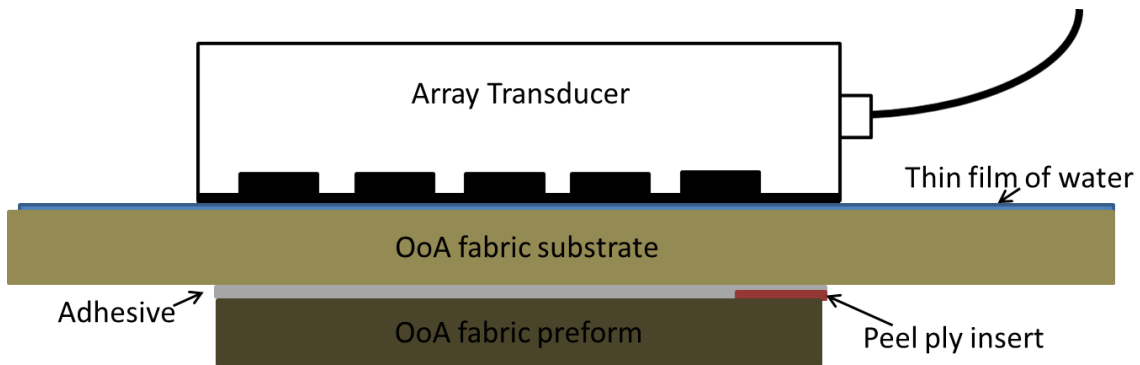


Figure 45: Representation of the overall system

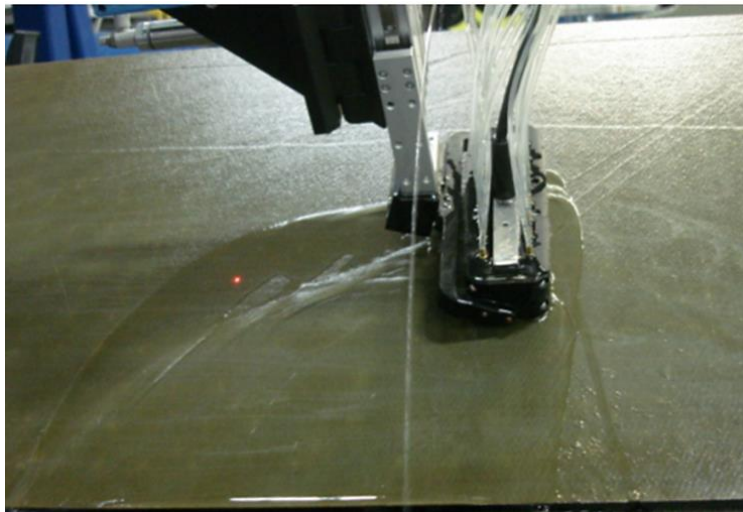


Figure 46: Array transducer setup atop the reference standard

3.3.2 Ultrasonic Parameters

The ultrasonic parameters were configured by utilizing “Machine State Editor” (AUSS XVII software package and user interface for ultrasonic setup, configuration and evaluation) shown in the following figures. The “Effector Selection” and “Data Parameters” were established within the Parameters tab shown in Figure 47. The primary location was selected as the forward horizontal scan (FwdHorizScan) effector with the standard (Std) terminal. The DelayLine (i.e. optimum distance between the array and the test object) was assigned with the appropriate transducer (Xducer) frequency of 5 MHz (i.e. optimum setting for the 2.8 MHz array) for the flat array (Array-Flat). The data parameters collected were from the transmitting (XMT) side of the system (i.e. only one transducer transmitting and receiving the signal) that include both the amplitude (Ampl) of the ultrasonic signal and surface distance (i.e. real time surface distance data collected to ensure constant contact between the transducer and test object).

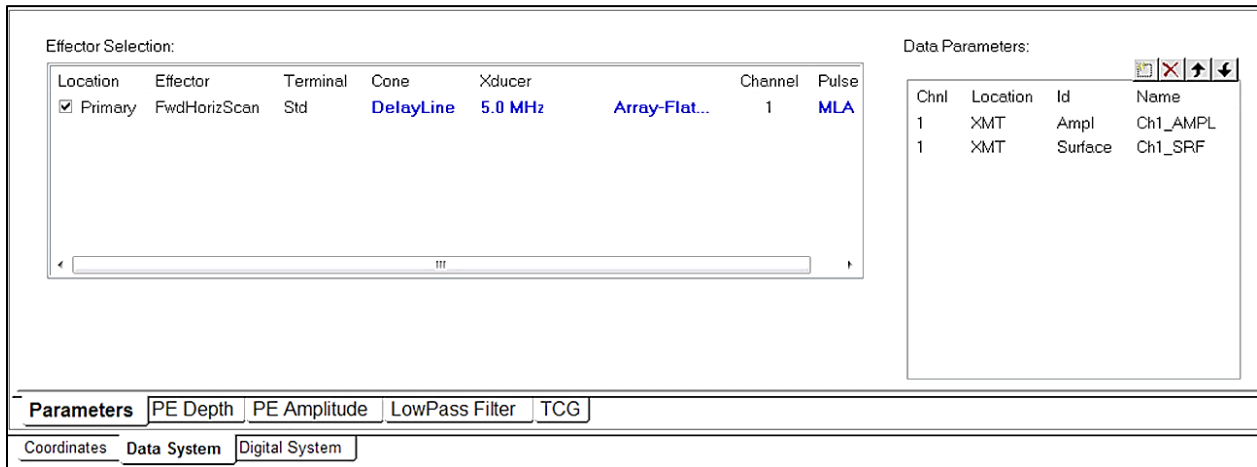


Figure 47: Parameters tab utilized to configure the end effector selection and data parameters

The Edit Pulsar/Receiver information is shown in Figure 48. The transmit aperture (i.e. the group of active elements that electronically transmit the signal) was set to 5 and the receive aperture (i.e. group of active elements that electronically receive the signal) was set to 4. The pulser was set to 40 volts with a focused beam at a depth of 5.00 inches (i.e. ideal voltage and

focal depth for the thickness of the part to be inspected). The receiver was set to a damping resistance of 50 Ohms.

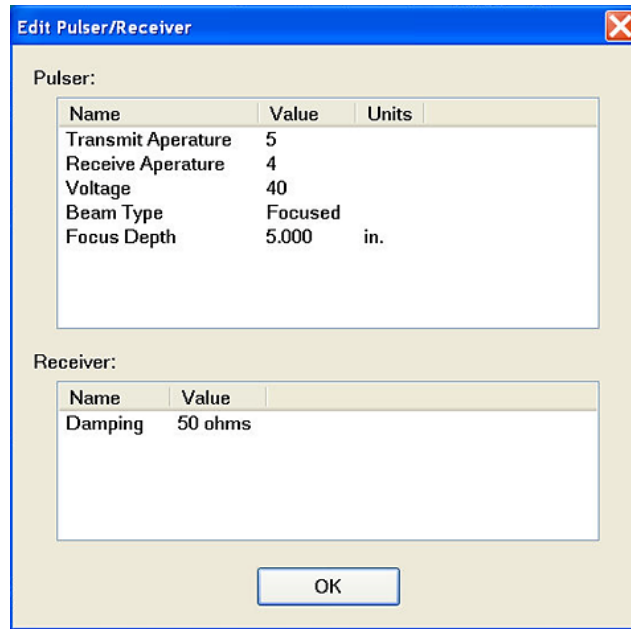


Figure 48: Edit Pulser/Receiver window

The depth and amplitude parameters were configured within the “PE Depth” and “PE Amplitude” tabs shown in Figure 49 and Figure 50, respectively. The parameters are established to capture and record the depth in inches and the peak amplitude of the signal in decibels (dB). The depth is determined by the distance the sound wave travels from the surface of the test object to the surface of the defect or the back surface of the test object. The distance can be calculated according to equation (3.1), where d is the distance traveled in inches, v is the velocity of sound within the material (in/ μ sec), and t is the measured round trip transit time [40].

$$d = vt/2 \tag{3.1}$$

The peak amplitude of the signal is based on the achieved voltage level and then converted to dB (i.e. logarithmic attenuation level) according to equation (3.2), where V is the measured potential in volts and V_o is the reference potential in volts [40].

$$dB = 20\log\left(\frac{V}{V_0}\right) \quad (3.2)$$

From the PE Depth tab, the “Gate” selected was the pulse echo depth gate (PED Gate) configured to ensure the reflected signals from the front and back surface of the test object that were obtained encompassing the entire part thickness. The “Video Signal Control” was configured to establish the optimum signal. The “Event Generation” was configured to establish accurate thickness readings in which the event marks (CEmrk) are triggered by the peak of the front and back surface signals, respectively. The “Part Characteristics” were configured per the type of material under inspection.

Figure 49: PE Depth tab utilized to configure the desired output in inches

From the PE Amplitude tab, the “Gate” selected was the pulse echo amplitude transmit gate (PEA XMT) configured to ensure the back surface signal was included. The peak amplitude (in volts) of the signal is detected by the PEA XMT Gate and then converted to dB according to equation (3.2) with ½ dB resolution with no additional gain required.

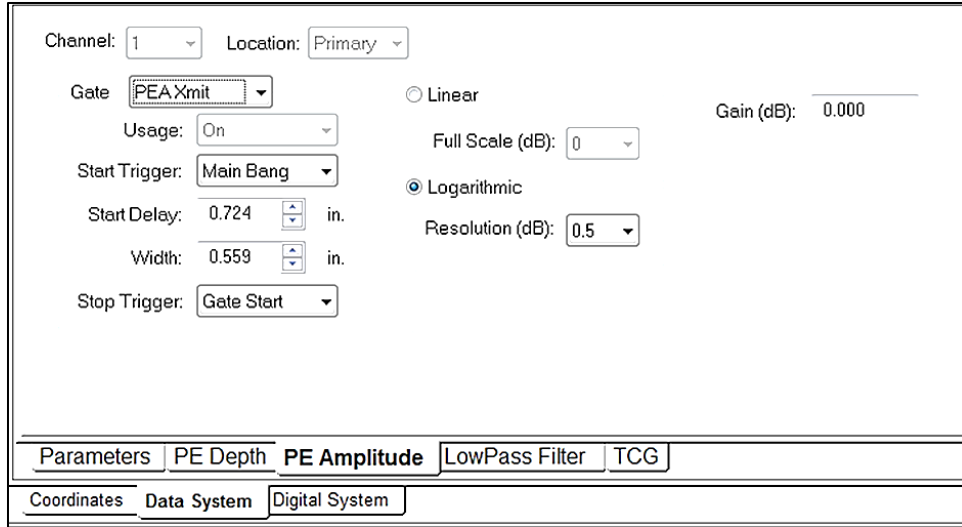


Figure 50: PE Amplitude tab utilized to configure the desired output in dB

The “Low Pass Filter” tab shown in Figure 51 is utilized to allow signals with a frequency lower than the selected cutoff frequency to pass while attenuating signals of higher frequencies. The cut off frequency was set to 5 MHz with an additional gain of 3.00 dB (i.e. additional gain to maintain the desired signal strength initially reduced by the low pass filter).

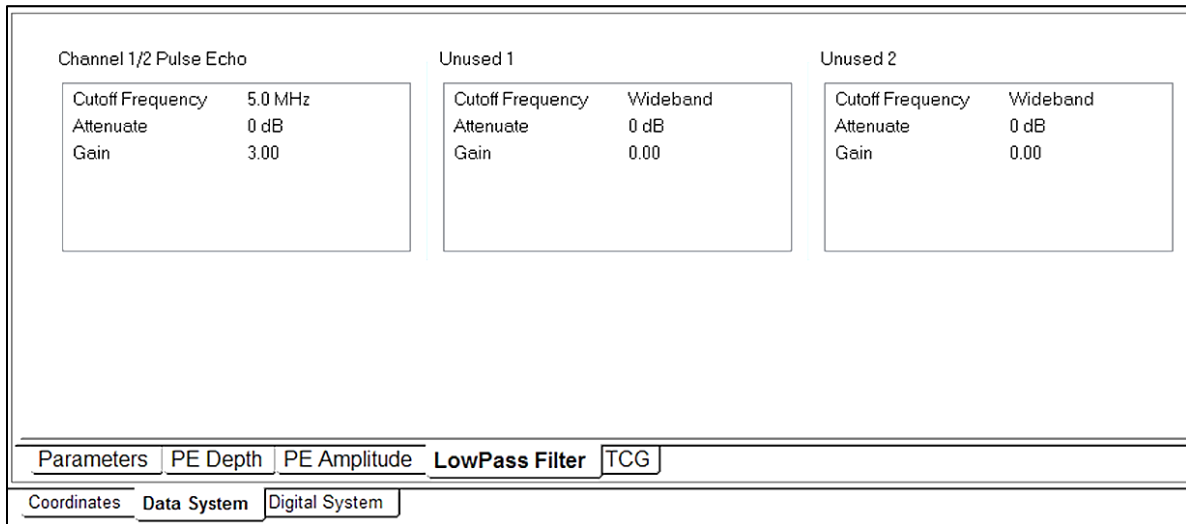


Figure 51: Low Pass Filter tab utilized to configure the low pass filter

The Time Corrected Gain (TCG) tab shown in Figure 52 is utilized to electronically compensate the signal gain as a function of time to obtain the same signal amplitude of reflections from equal reflectors at different thicknesses.

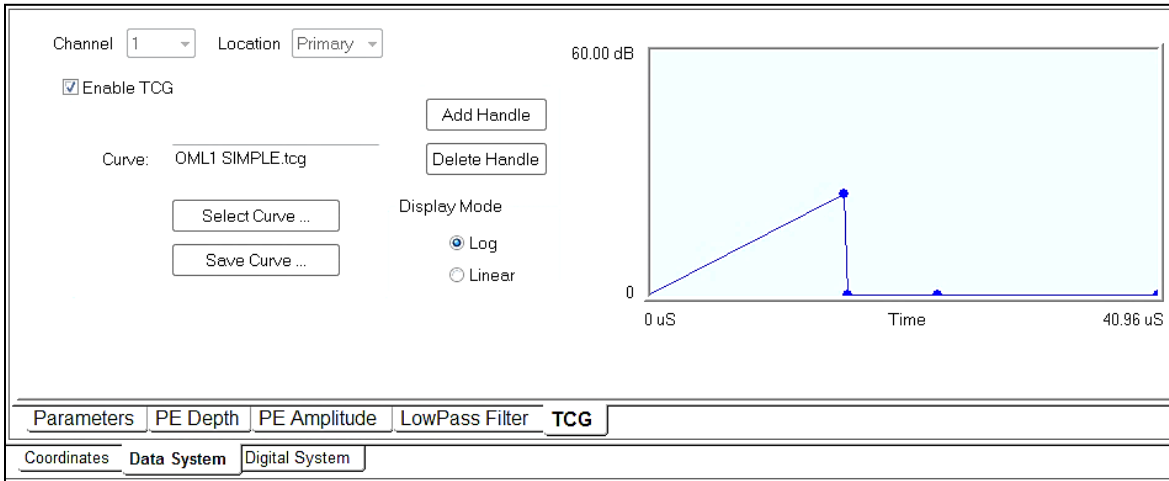


Figure 52: Time Corrected Gain (TCG) tab utilized to setup the TCG over a range of thicknesses

The following Figure 53 through Figure 56 show the video output displayed in real time via the A-Scan scope display based on the selected ultrasonic parameters.

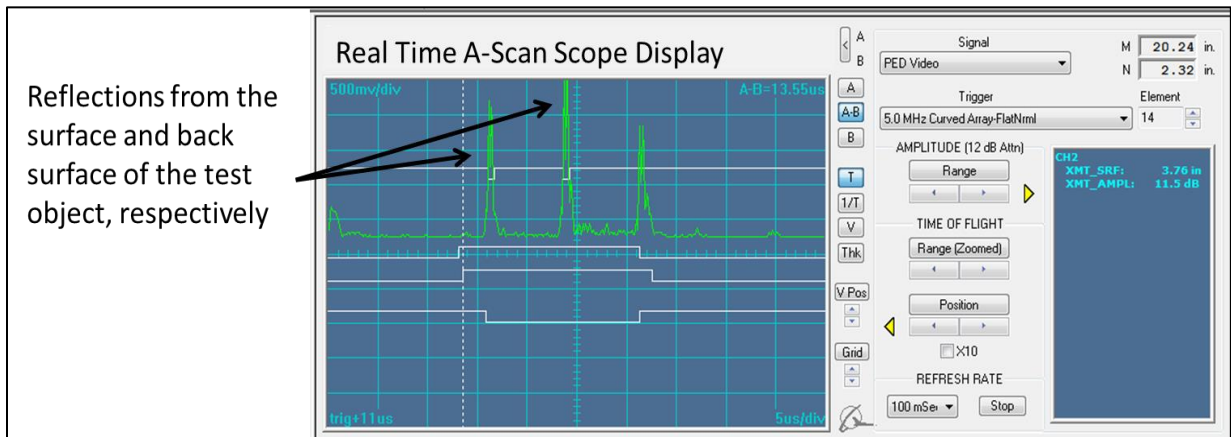


Figure 53: A-Scan display illustrating the reflections from the surface and back surface of the test object

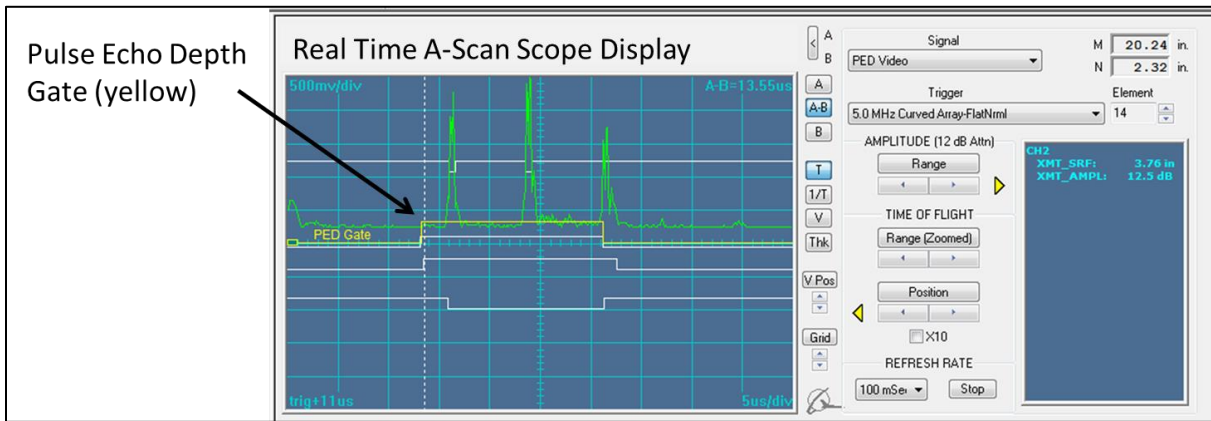


Figure 54: A-Scan display illustrating the pulse echo depth gate, triggered by the “main bang” (i.e. initial signal transmitted by the transducer)

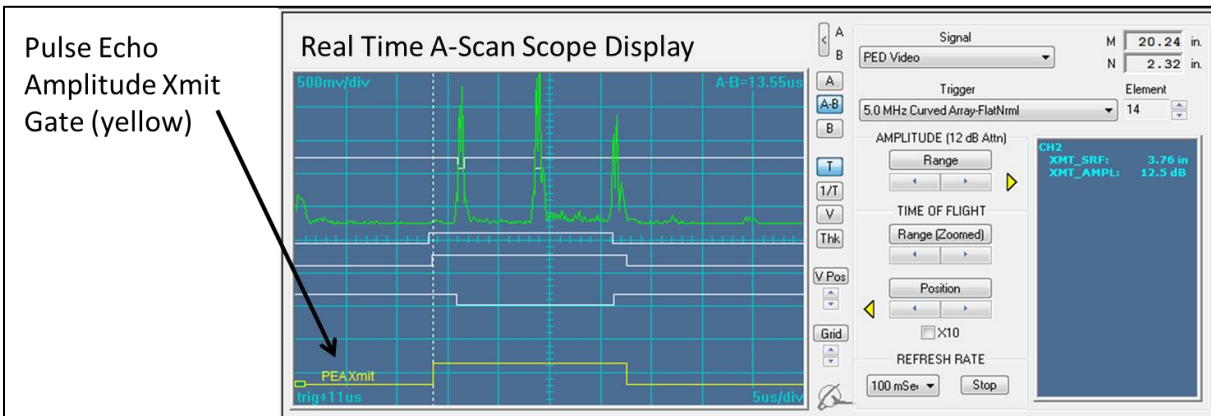


Figure 55: A-Scan display illustrating the pulse echo amplitude gate, triggered by the first interface (i.e. initial signal transmitted by the surface of the test object)

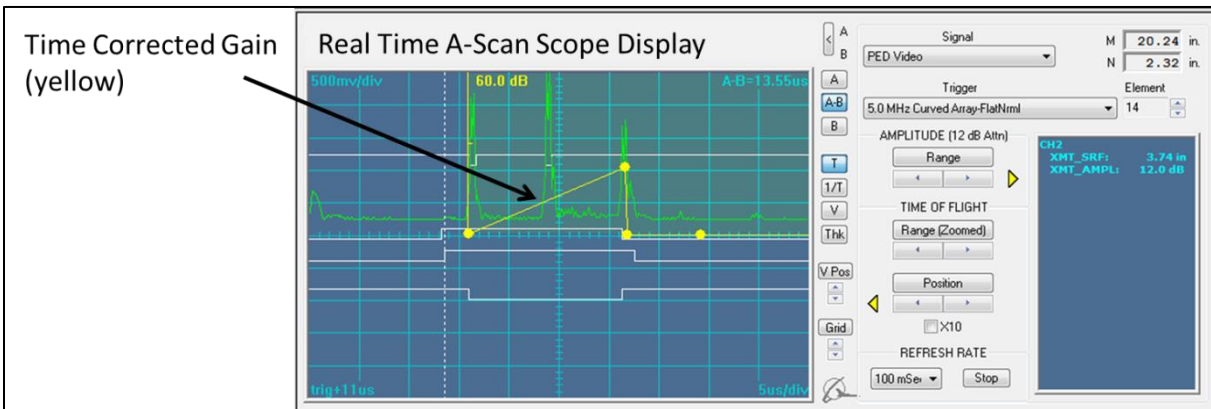


Figure 56: A-Scan display illustrating the time corrected gain (TCG), triggered by the first interface (i.e. compensation of gain as a function of time to obtain the same signal amplitude of reflections from equal reflectors at different thicknesses)

3.3.3 Ultrasonic Inspection

Once the ultrasonic parameters were set and the initial setup was complete, the reference standard was ultrasonically inspected as shown in Figure 57. Figure 58 shows the resulting amplitude C-Scan of the reference standard. The A-Scan depicts the front and back surface reflectors at one point on the fabric substrate for reference.

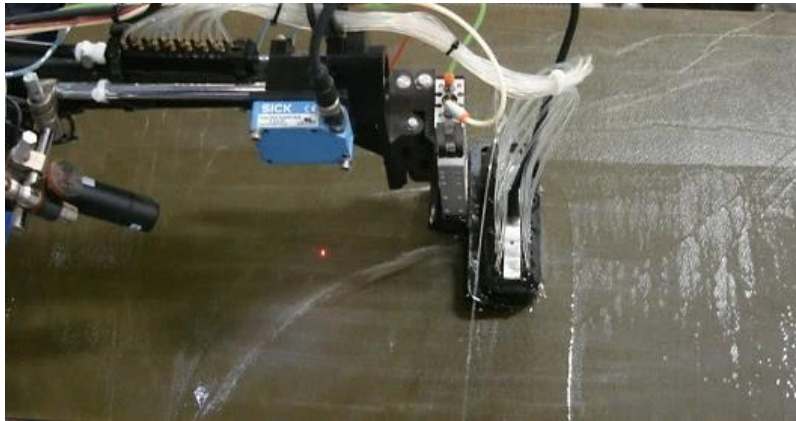


Figure 57: Ultrasonic inspection of the reference standard

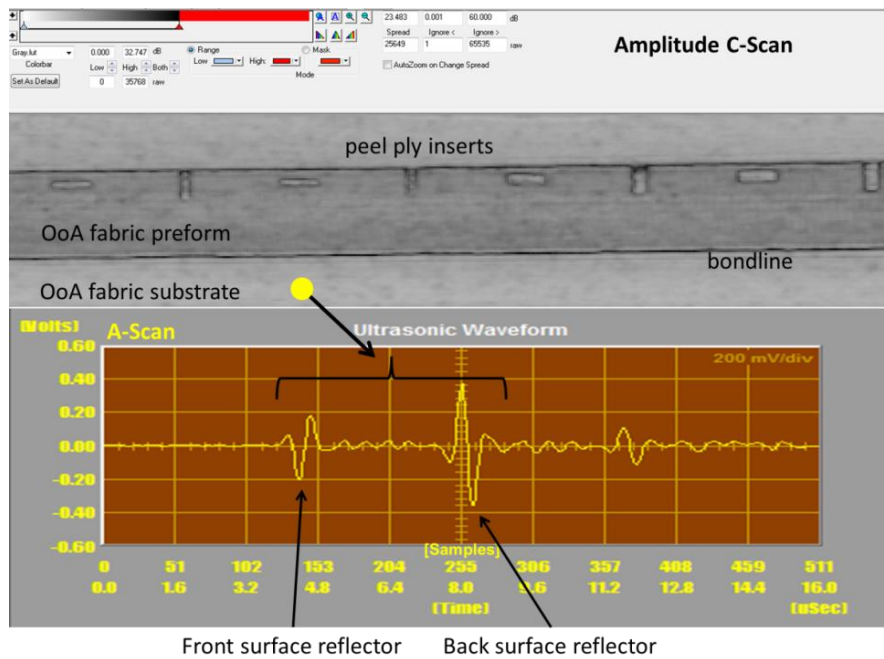


Figure 58: Amplitude C-Scan of the reference standard with front and back surface reflectors as reference

The edge of each insert is apparent due to edge reflections that are not normal to the surface resulting in signal loss (i.e. attenuation) as shown in Figure 59.

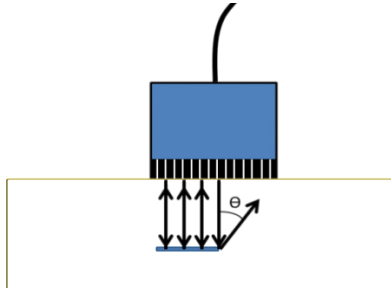


Figure 59: Resulting edge reflection that is not normal to the surface

Figure 60 shows the resulting attenuation from the edge of the insert compared to the center of the insert illustrated by the A-Scan. The C-Scan was set to an upper threshold of 20 dB (i.e. to distinguish signals that attenuate more than 20 dB) for clarification. Nevertheless, the apparent edge of each insert is not an accurate measure of detectability based on size and will be further addressed in Chapter 5.

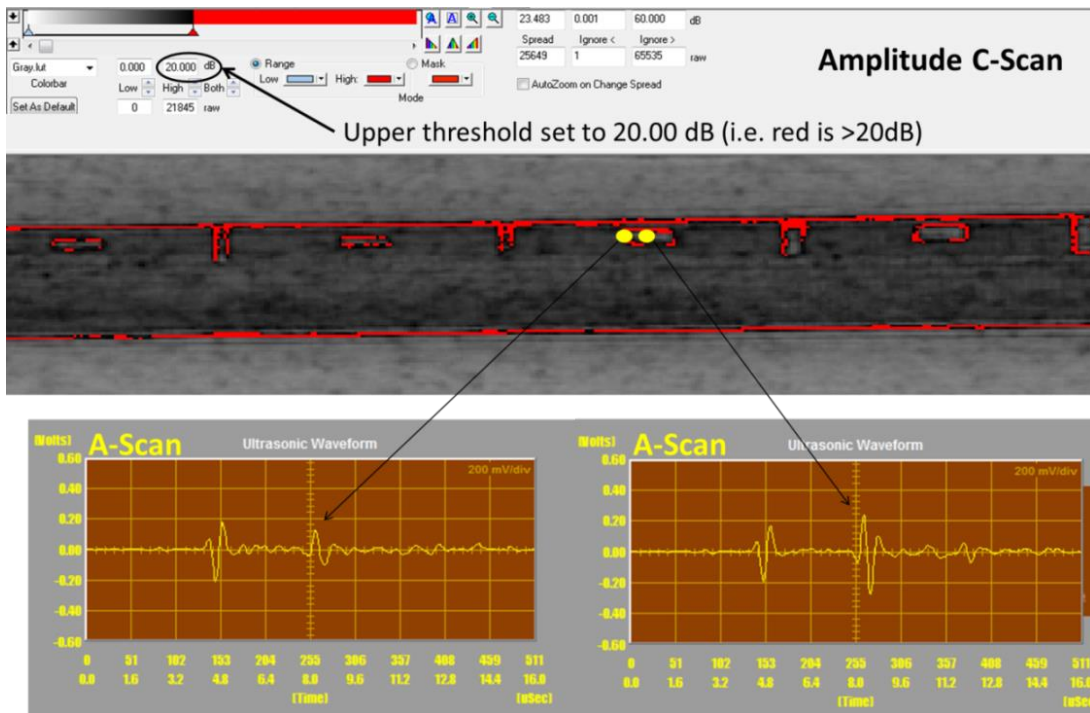


Figure 60: Comparison of attenuation due to the edge of the insert and the center of the insert

CHAPTER 4

ALGORITHM DEVELOPMENT

This chapter illustrates the method used to define the final algorithm through waveform analysis and real time post processing. Libraries of post processing software functions are strung together in a linear workflow. The digital waveforms are viewed as either raw or processed via the A-Scan scope. The resulting output is a desired C-Scan to further interpret the results.

4.1 Algorithm Workflow

The post process algorithm follows a linear workflow in which, calculations are based on engineering tools (i.e. function menus) to develop the algorithm. The workflow starts with the raw ultrasonic waveform from the array. A library of function menus can then be strung together with the appropriate parameters to generate a properly scaled C-Scan. Figure 61 shows the algorithm workflow for processing the ultrasonic waveform.

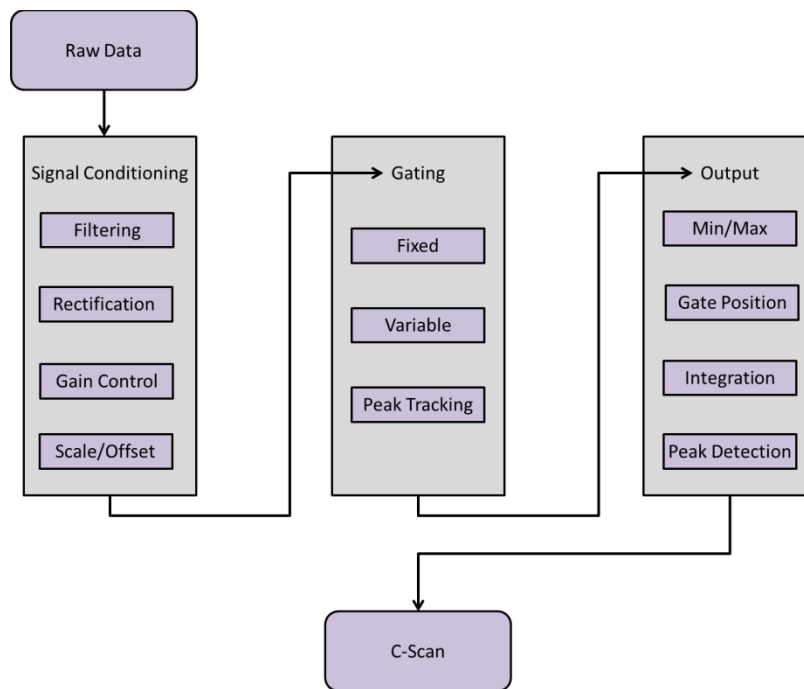


Figure 61: Algorithm Workflow

4.2 Signal conditioning functions

Raw ultrasonic data received from the array can be post processed and conditioned by filtering, rectification, gain control and scale and offset depending on the desired signal output.

4.2.1 Filtering

Raw data is subject to noise due to undesirable reflections, signal noise and other sources. The types of noise received depend on ultrasonic frequency, surface irregularities and internal reflections of the test object, the ultrasonic scanning system and electronics performing digital signal conversion. Low pass and high pass filter options are available to remove any unwanted noise. Low pass filters allow signals with a frequency lower than the cutoff frequency to pass while attenuating signals of higher frequencies. High pass filters allow signals with a frequency higher than the cutoff frequency to pass while attenuating signals of lower frequencies. Figure 62 shows an example of low-pass and high-pass filtering. The input signal is three cycles of a sine wave plus a slowly rising ramp. The impulse response is a smooth arch resulting in only the slowly changing ramp being passed to the output signal [84].

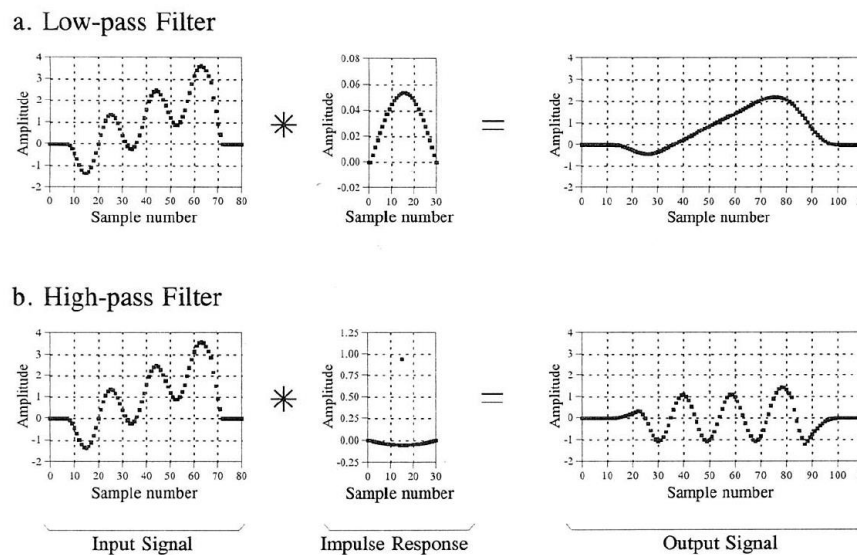


Figure 62: Examples of (a) low-pass and (b) high-pass filtering including an input signal, impulse response and output signal [84]

Figure 63 depicts the Infinite Impulse Response (IIR) low pass and high pass filter menu function. For example, the low pass filter option is selected with a cutoff frequency of 10 MHz. The 2 Pole Express option provides faster post processing times for large amounts of data associated with array inspections.

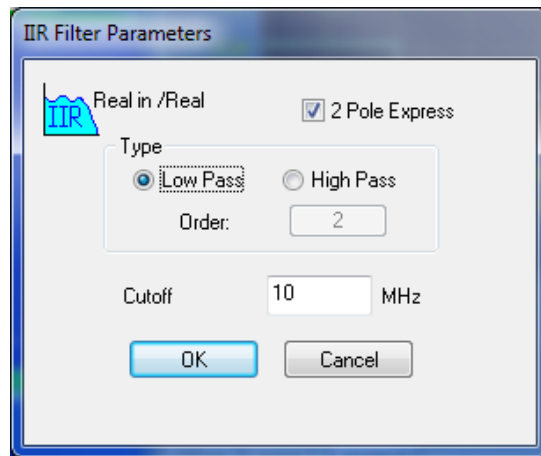
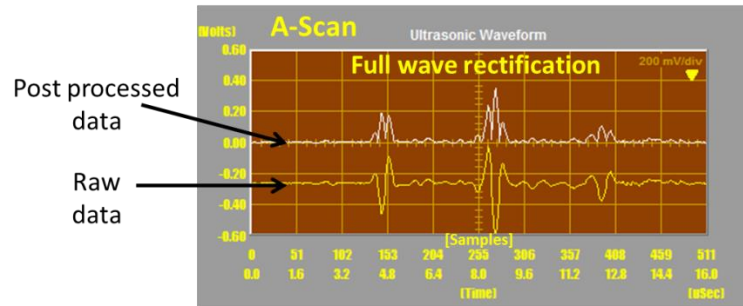


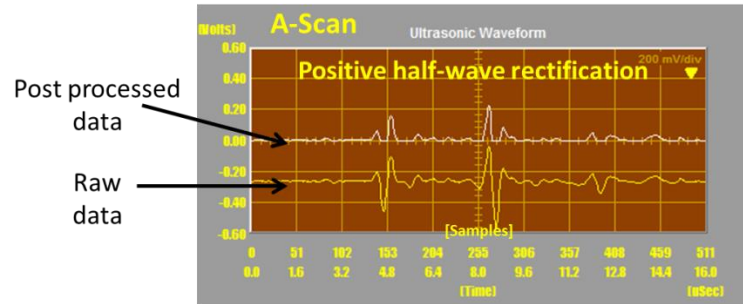
Figure 63: IIR low pass and high pass filter menu function and parameters

4.2.2 Rectification

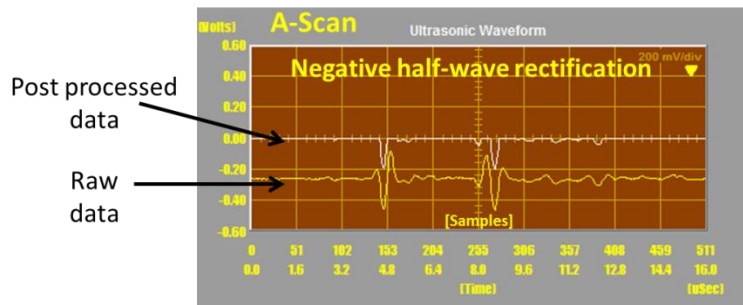
The raw RF signal can be post processed and rectified (e.g. full wave, negative half-wave and positive half-wave) depending on the desired output shown in Figure 64. Full wave rectification is the absolute value of the peak amplitude of the waveform samples (i.e. amount of data acquired per waveform). The positive half-wave rectification is the remaining positive samples with negative samples set to zero. The negative half-wave rectification is the remaining negative samples with positive samples set to zero. Figure 65 depicts the rectifier menu function and parameters.



(a)



(b)



(c)

Figure 64: Raw data (yellow) and post processed data (white) of (a) full wave rectification, (b) positive half-wave rectification and (c) negative half-wave rectification



Figure 65: Rectifier menu function and parameters

4.2.3 Gain Control

Gain controls are used to increase the power or amplitude of the ultrasonic signal. There are two gain control options that can be utilized based on the desired output, variable gain control and automated gain control. The variable gain control shown in Figure 66 varies the gain of the amplitude signal with time, either linearly or exponentially, to the desired maximum input. The variable gain control shown in Figure 67 is most commonly used to electronically compensate the signal gain as a function of time to obtain the same signal amplitude of reflections from equal reflectors at different thicknesses. The automatic gain control holds the desired (+/-) signal to a specific voltage level along the entire waveform, inside or outside of the gate. This option is typically used to provide consistent threshold levels for improved defect detection.

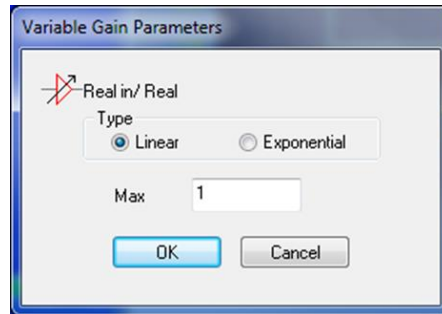


Figure 66: Variable gain menu function and parameters

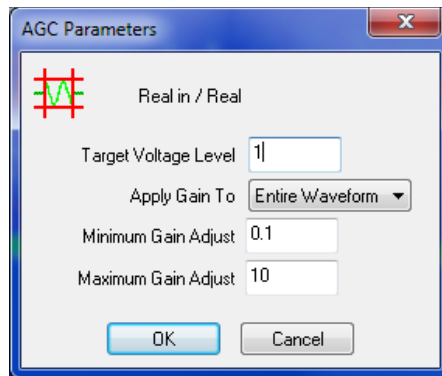


Figure 67: Automatic gain control (ACG) menu function and parameters

4.2.4 Scale/Offset

Each point of the waveform can be multiplied by a given positive or negative scale value. The scale can be useful to eliminate undesirable portions of the waveform or enhance desirable portions. The offset is applied to the input and can also be a positive or negative value. The offset is most commonly used to offset the post processed signal from the raw signal for better interpretation. Figure 68 shows two scale/offset menu functions and parameters with the raw and post processed A-Scan results. For example, the first scale/offset function menu applies a scale of zero to eliminate the front surface reflector with an offset of 0.4 volts. The second scale/offset function menu applies a scale of 1.5 to enhance the back surface reflector with an offset of 0.4 volts.

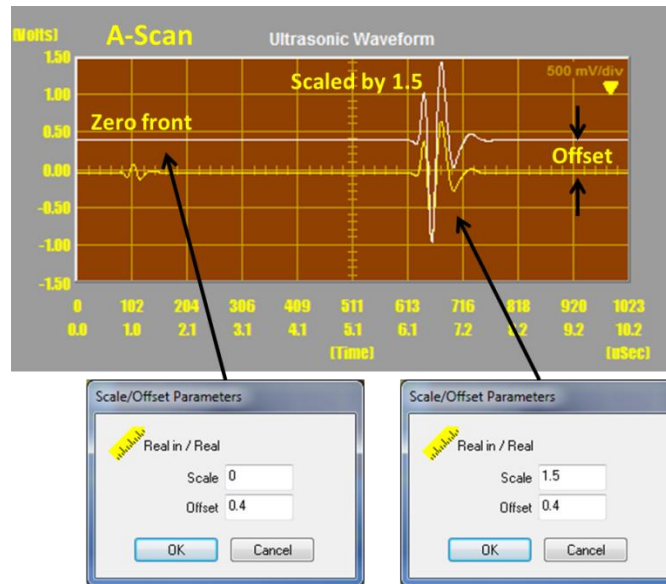


Figure 68: Examples of the Scale/Offset menu function and parameters, with the raw and post processed A-Scan results

4.3 Gating Functions

Data collection gates are established within specified regions of the waveform to monitor the signal levels at each point. Specific gating functions determine the region of the waveform that is used for the calculations.

4.3.1 Fixed Gate

The fixed gate function is a fixed length based on specified start and end triggers. The gate can be set to start and end at any sample of the waveform. For example Figure 69 shows the fixed gate to start at 0 samples and end at 1023 samples.

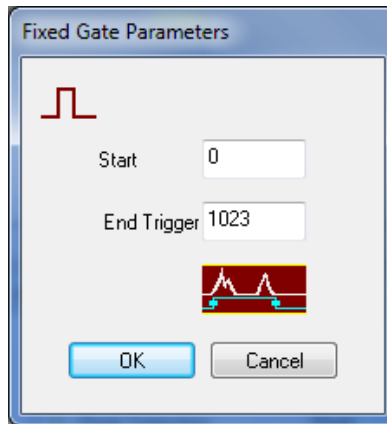


Figure 69: Fixed gate menu function and parameters

4.3.2 Variable Gate

The variable gate allows for the gate to be placed based on the first interface (i.e. first signal that exceeds the selected voltage threshold level) or the maximum signal. The trigger start window enables the start of the gate to be triggered in between a specified range of samples. The trigger selection can be set to threshold or maximum “signal + the start delay”. The gate will end at the “start + end delay”. The gate delays in which the gate actually starts and stops can be any (+/-) value. The threshold is the specified value in which the signal must cross in order to trigger the gate. The material velocity is set based on the material inspected for accurate thickness measurements (e.g. 115995.7969 in/sec). Figure 70 shows the variable gate menu function and the parameters to be selected and specified.

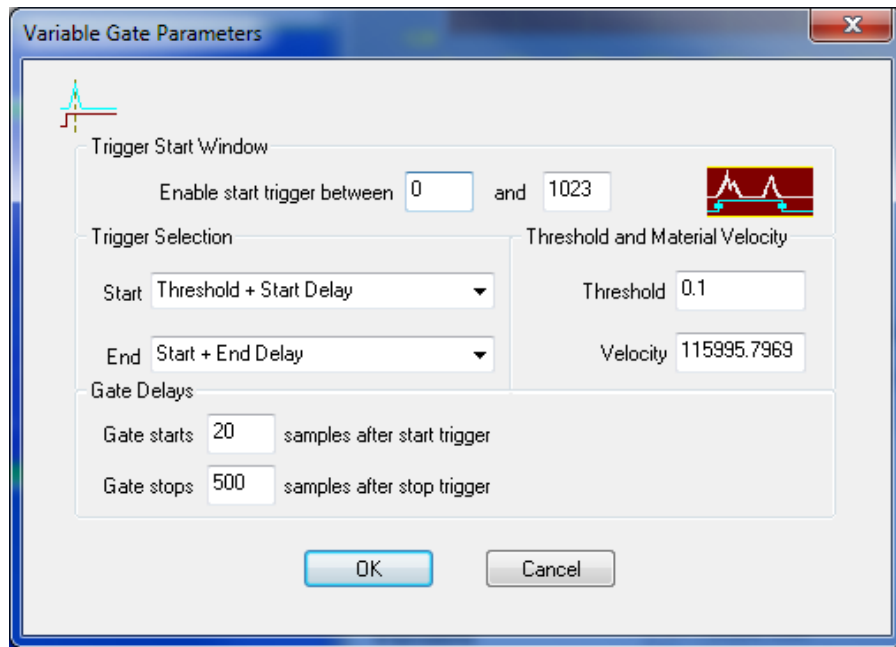


Figure 70: Variable gate menu function and parameters

4.3.3 Peak Tracking Gate

The peak tracking gate is based on the number of peaks above a threshold (Peak Thres). A peak is defined as a point above the selected threshold that is greater than the preceding and following points. Peak A represents the start of the gate and peak B represents the end. Peak A and peak B can also be offset to a specified value to encompass a desired portion of the waveform other than the peak itself. The trigger can be based on either the peak of the signal (i.e. center of the signal) or the positive slope (i.e. left side of the signal at the threshold point) or the negative slope (i.e. right side of the signal at the threshold point). Figure 71 shows the peak tracking gate menu function and the parameters to be selected and specified.

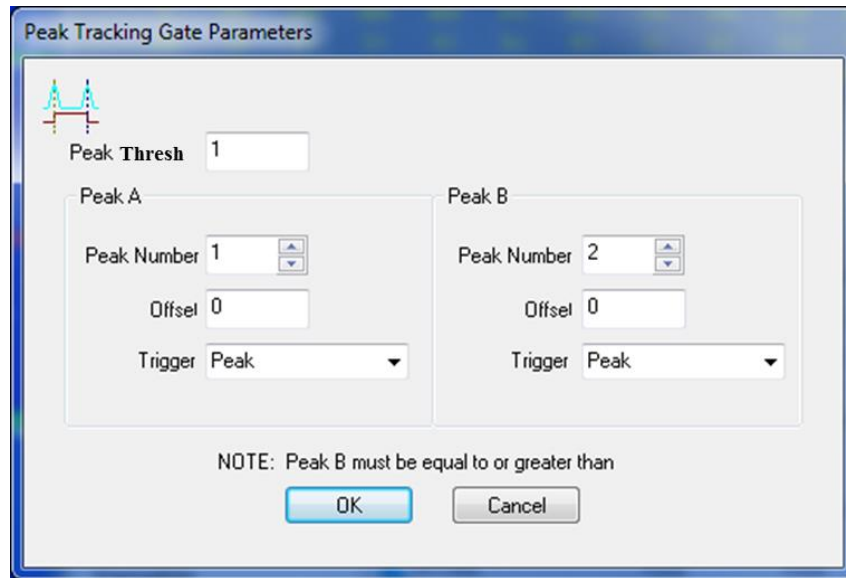


Figure 71: Peak tracking gate menu function and parameters

4.4 Output

The following function menus and parameters are available to further process the data into an output C-Scan for interpretation and results.

4.4.1 Minimum- Maximum Output

The minimum-maximum output locates the minimum or maximum value of the waveform within the current gating configuration and displays the information as user defined engineering units or on a logarithmic scale (i.e. dB). The distance from the gate count at the beginning of the waveform to the minimum or maximum value can also be determined for a variety of thickness measurements. Figure 72 shows the minimum-maximum function menu and parameter options. For example, the name of the C-Scan parameter tab is Maximum and only the maximum value will be displayed from 0 to 100 as a percentage.

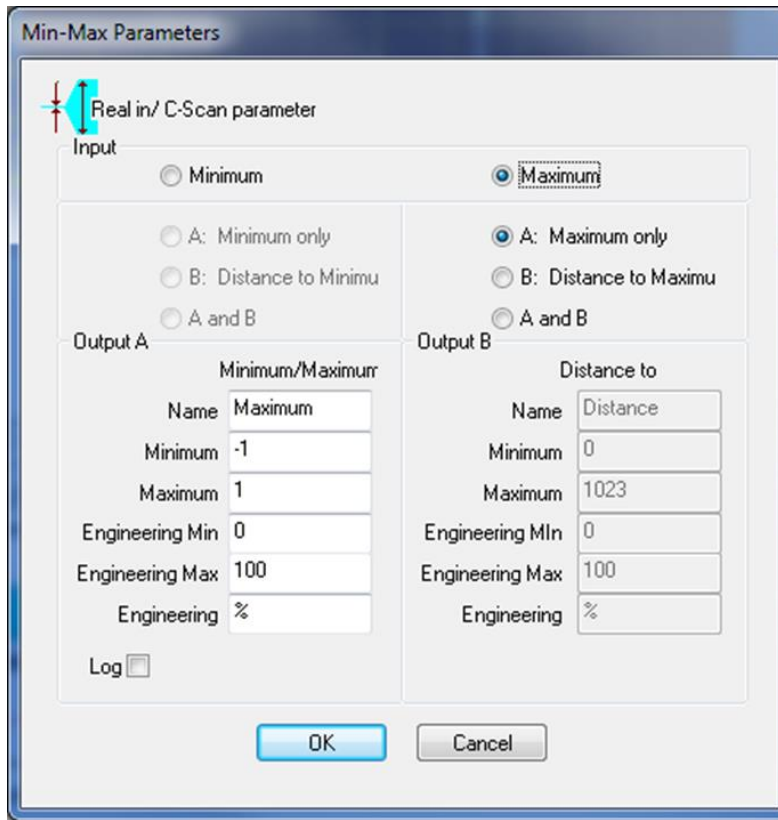


Figure 72: Minimum-Maximum function menu and parameters

4.4.2 Gate Position

The gate position output provides additional feedback on the length of the gate. The current gate length = start of the gate + the end of the gate +1. This function menu can be used when the gate length is a relevant parameter utilized for accurate thickness reading. The minimum and maximum values can be set based on the number of samples taken and displayed in user defined engineering units. Figure 73 shows the gate position function menu and parameters. For example, the name of the C-Scan parameter tab is GatePos and the samples taken are from 0 to 1023 with the output displayed from 0 to 100 as a percentage.

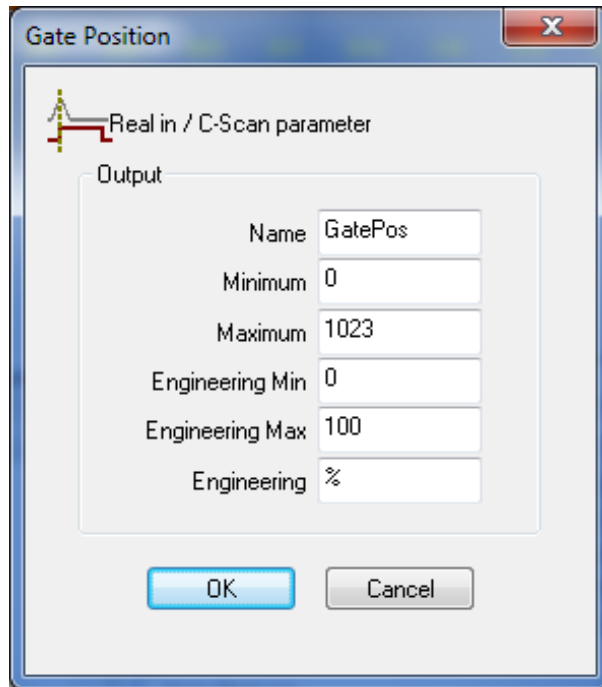


Figure 73: Gate position function menu and parameters

4.4.3 Integrate

The integrate output is the sum of all the x axis data points within the current gate relative to the amplitude. A simple calculation can be performed of the running sum according to equation (4.1). The running sum is calculated by summing all of the points in the original signal to the left of the sample location where $x[n]$ is the original signal and $y[n]$ is the running sum [84].

$$y[n] = x[n] + y[n - 1] \quad (4.1)$$

The integrate function menu is useful for differentiating signals of similar nature and reflections of similar acoustic impedance. The minimum and maximum values can be set based on the number of samples taken and displayed in user defined engineering units. Figure 74 shows the integrate function menu and parameters. For example, the name of the C-Scan parameter tab is Integrate and the samples taken are from 0 to 1023 with the output displayed from 0 to 100 as percent integration.

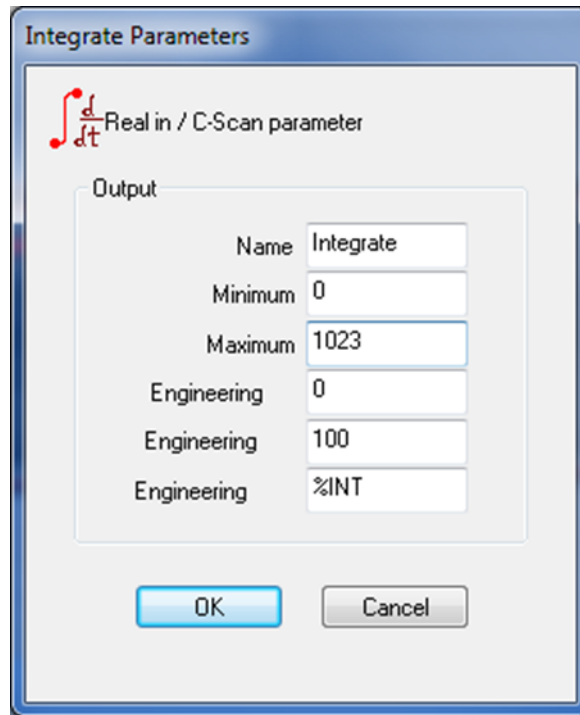


Figure 74: Integrate function menu and parameters

4.4.4 Peak Detection

The peak detection output is either the amplitude of the signal or the time in which the signal occurred (i.e. to determine thickness) or both. The peak is defined as a point above the threshold that is greater than the preceding or following points. The amplitude parameters are the amplitude of peaks A or B, the difference between the two or the ratio. The time parameters are either the width of the maximum peak, the distance from the start of the waveform (i.e. 0) to the maximum peak or the distance between peak A and B. Figure 75 shows the peak detection function menu and parameters. For example, the name of the C-Scan parameter tabs are Amplitude and Time in which both amplitude and time are selected as the output displaying the amplitude of peak A and time as the maximum peak width. The threshold is set to 0 volts and the user defined engineering units are 0-100 volts for amplitude and 0-1 samples for time.

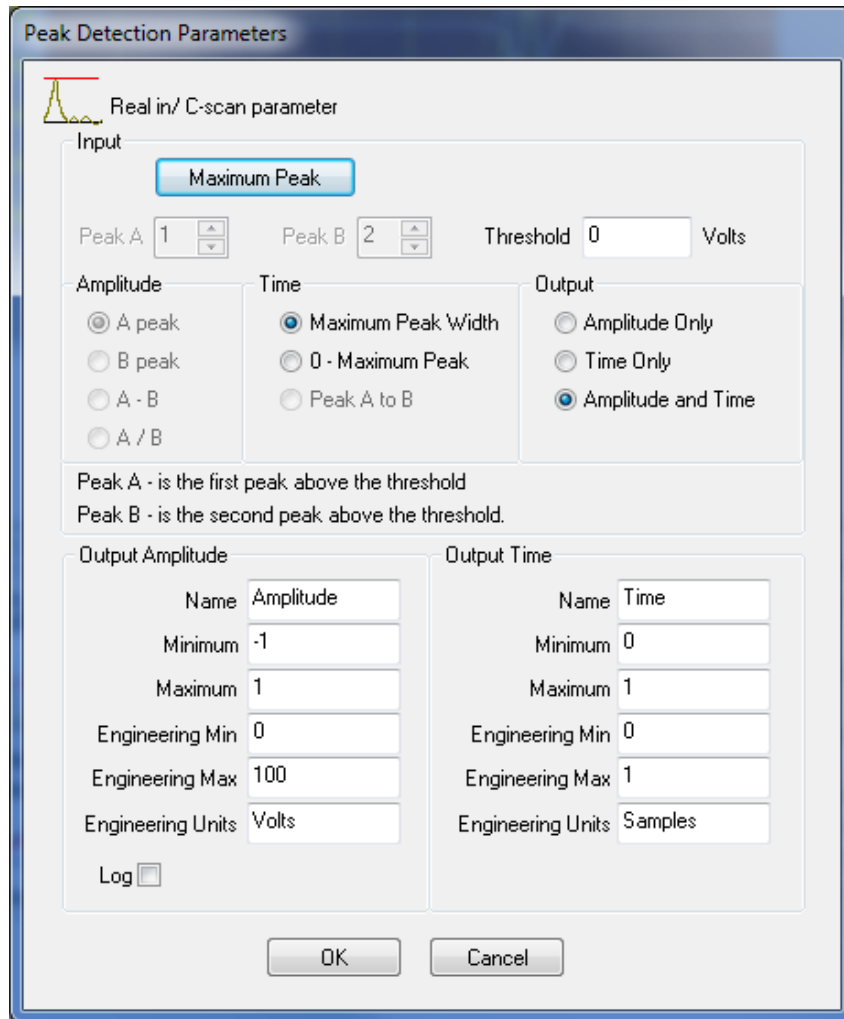


Figure 75: Peak detection function menu and parameters

4.4.5 A-Scan Output

The A-Scan output function menu shown in Figure 76 displays the waveform by making use of the parameter tab created by the function, shown in Figure 77. This allows the user to visually see the A-Scan output (e.g. both raw and processed waveform) at any point in the algorithm, as the algorithm is created.

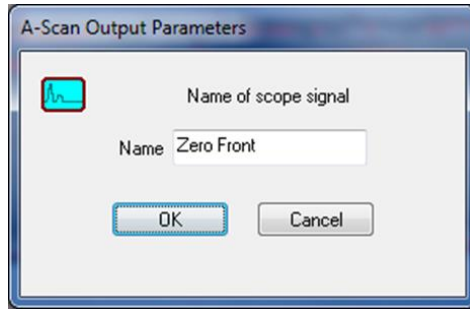


Figure 76: A-Scan Output function menu and parameters

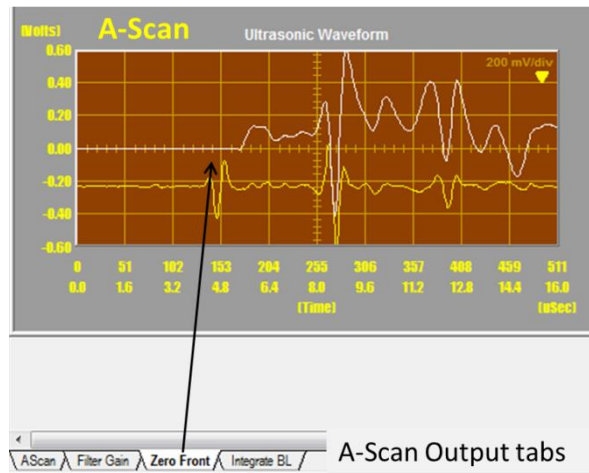


Figure 77: A-Scan Output tabs that shows the result in the A-Scan

4.5 Ultrasonic Waveform Region of Interest

As previously mentioned the difference in signal reflections from the peel ply inserts and the bondline are alike, due to very little acoustic impedance difference. The ultrasonic waveform of each reflection was reviewed in the frequency and time domain to determine regions of interest (ROI) and what signal processing techniques could be applied to improve the results. Fourier analysis can be applied to the frequency domain of waveforms with different amplitudes, frequencies and phases [85]. Figure 78 shows the ultrasonic waveform of the peel ply insert and the bondline in the frequency domain. Both contain similar frequencies and phases; however, the most significant difference is the change in amplitude below 0.5 MHz. This will be the region of interest in which a low pass filter will be applied to isolate the signal.

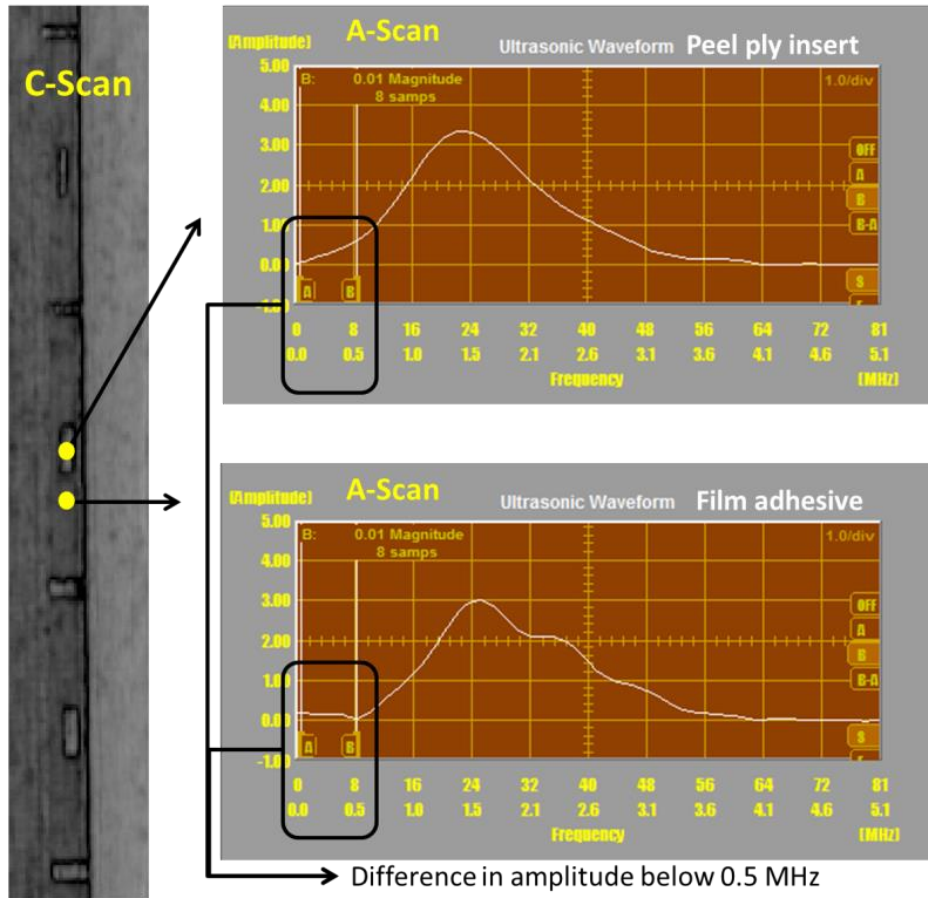


Figure 78: Ultrasonic waveform of the peel ply insert and the bondline in the frequency domain

Analyses of the time domain can further differentiate between signal amplitudes in volts or dB, time and phase shifts. Figure 79 shows the ultrasonic waveform of the peel ply insert and the bondline in the time domain. The portion of the waveform found to be of greatest difference is the magnitude of the negative half wave reflection. In theory, integration will be an appropriate signal processing technique to further differentiate between the two signals by summing each ROI. This technique would provide more information compared to simple difference in amplitude to improve the signal to noise ratio.

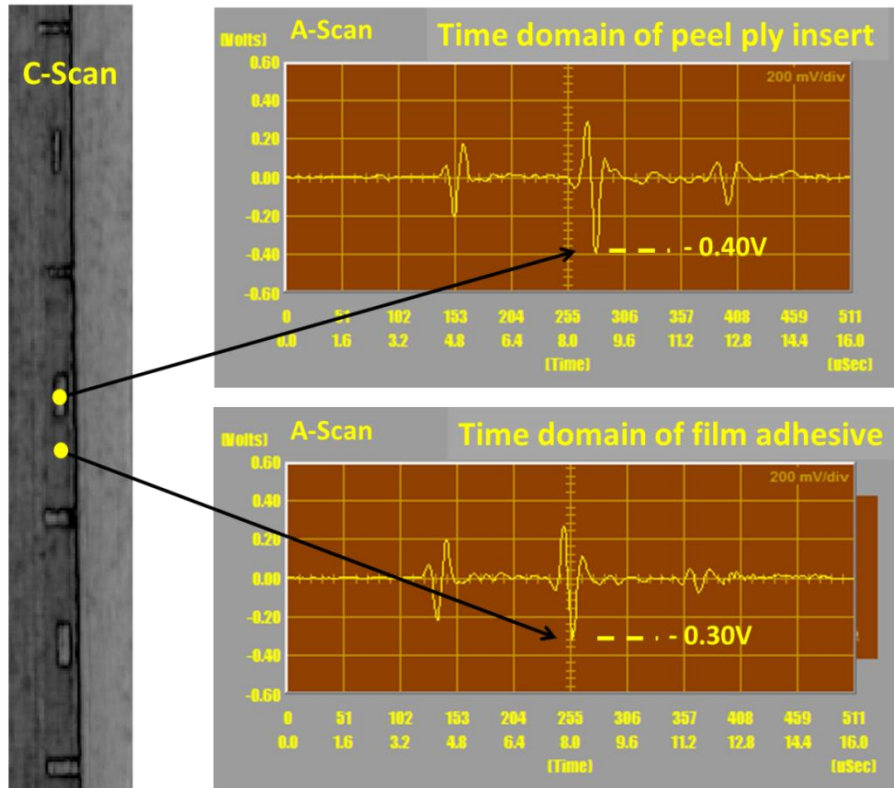


Figure 79: Ultrasonic waveform of the peel ply insert and the bondline in the time domain

Therefore, the final algorithm will be constructed by appropriate signal conditioning and gating configurations of the digital waveform of interest to be output in individual C-Scan parameter tabs for further analysis.

4.6 Final Algorithm

The following illustrates the workflow of the final algorithm with the corresponding ultrasonic waveforms shown by the corresponding A-Scan scopes at selected points on the C-Scan. The raw data is in yellow and the post processed data is in white.

4.6.1 Signal Conditioning Algorithm Workflow

The following signal conditioning algorithm, shown in Figure 80, was performed to eliminate unwanted noise (i.e. reflections and refractions) inherent to the OoA CFRP bonded assembly and then scaled to invert negative half wave reflections enhancing the desired ROI.

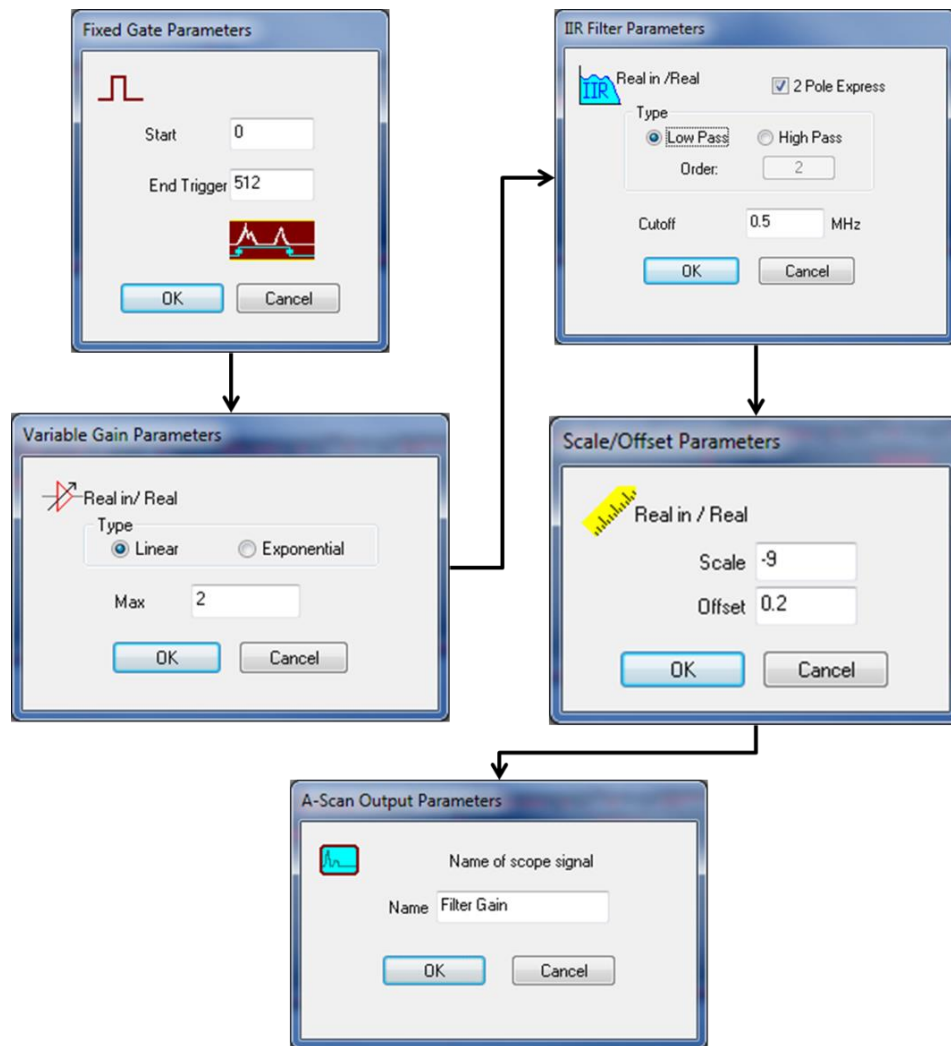


Figure 80: Signal conditioning algorithm workflow

First, the fixed gate was set to incorporate all of the sampled data from 0 to 512 samples. Next, variable gain was applied to linearly increase the gain to a maximum of 2 volts, shown in Figure 81. A low pass filter with a 0.5 MHz cutoff was then applied to isolate the signal of interest discovered in the frequency domain, shown in Figure 82. Each point of the waveform was then scaled by a negative 9 inverting all negative points and then offset for visual representation, shown in Figure 83. The scale offset function was performed to enhance the region of interest (i.e. negative wave reflections from the peel ply inserts just beyond the bondline) shown in Figure 84.

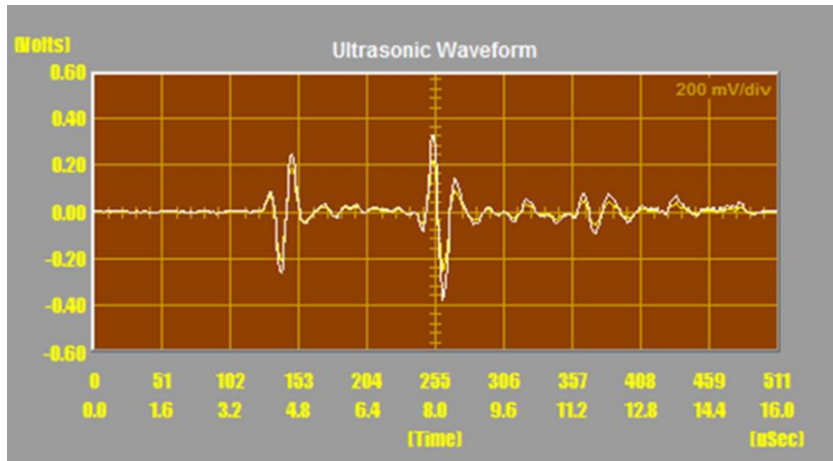


Figure 81: Ultrasonic waveform with variable gain

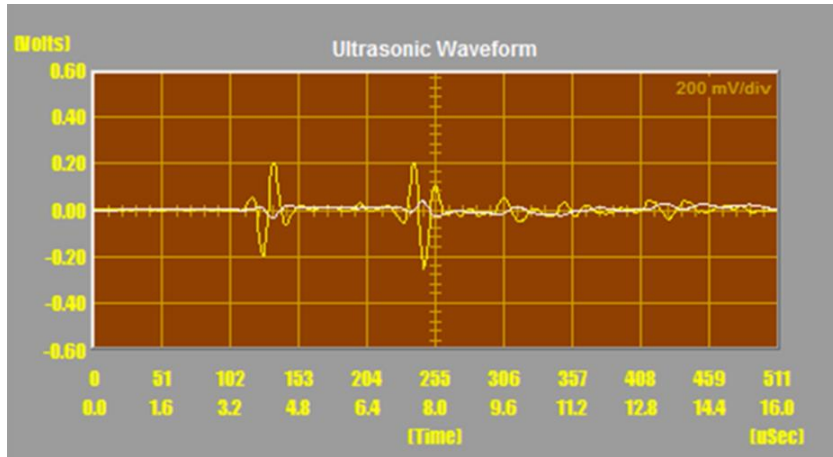


Figure 82: Ultrasonic waveform with low pass filter

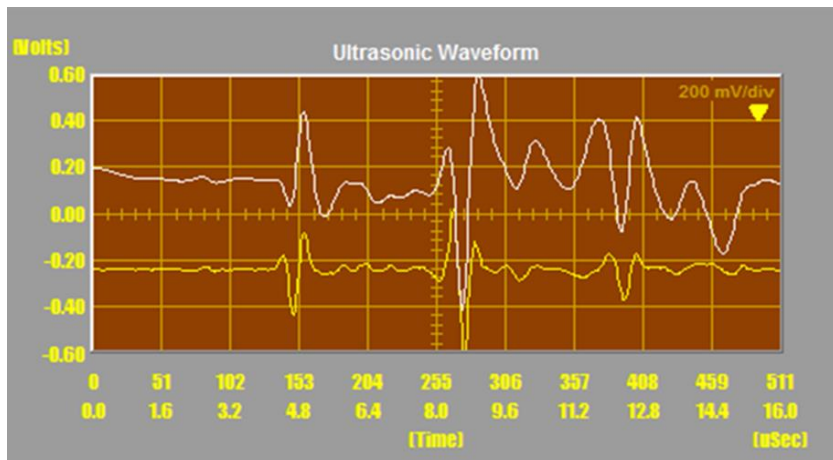


Figure 83: Ultrasonic waveform with scale/offset

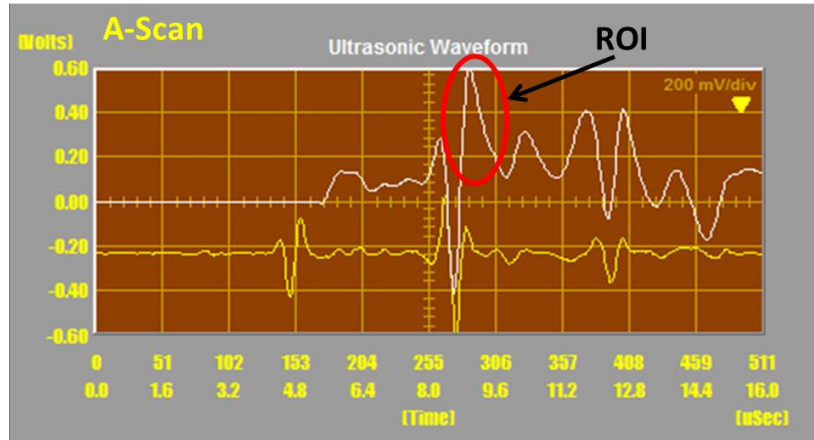


Figure 84: Ultrasonic waveform illustrating the region of interest

4.6.2 Zero Front Surface Algorithm Workflow

The following zero front surface algorithm, shown in Figure 85, was performed to set all of the points just beyond the front surface reflector to zero. This ensures all desired reflections beyond the front surface exceed the defined threshold.

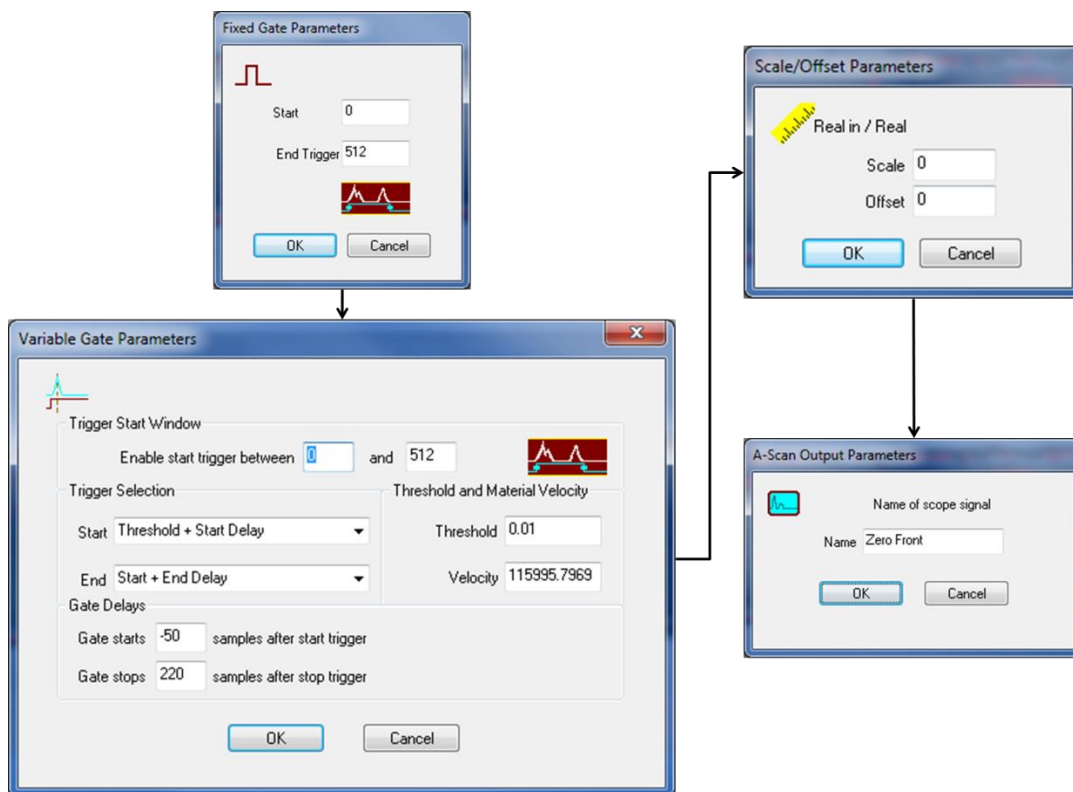


Figure 85: Zero front surface algorithm workflow

First, the fixed gate was set to incorporate all of the sampled data from 0 to 512 samples. A variable gate was then set at a threshold of 0.01 volts starting at negative 50 samples after the start trigger (i.e. threshold + start delay) and ending 220 samples after the stop trigger (i.e. start + end delay). All of the points within the variable gate were then scaled by zero, eliminating the front surface signal reflection, shown in Figure 86.

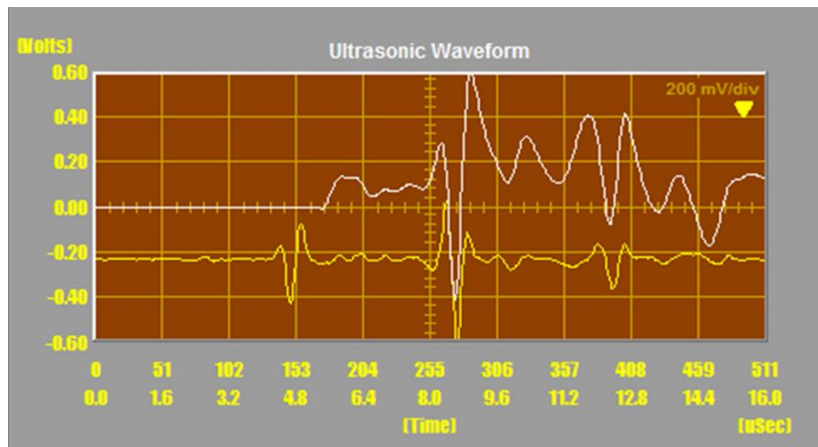


Figure 86: Front surface signal reflection set to zero

4.6.3 Integrate Algorithm Workflow

The following integrate algorithm, shown in Figure 87, was performed to sum the amplitude data under the reflected signal of interest within the current gate (i.e. set to incorporate only the signal of interest) to differentiate the peel ply insert and the bondline.

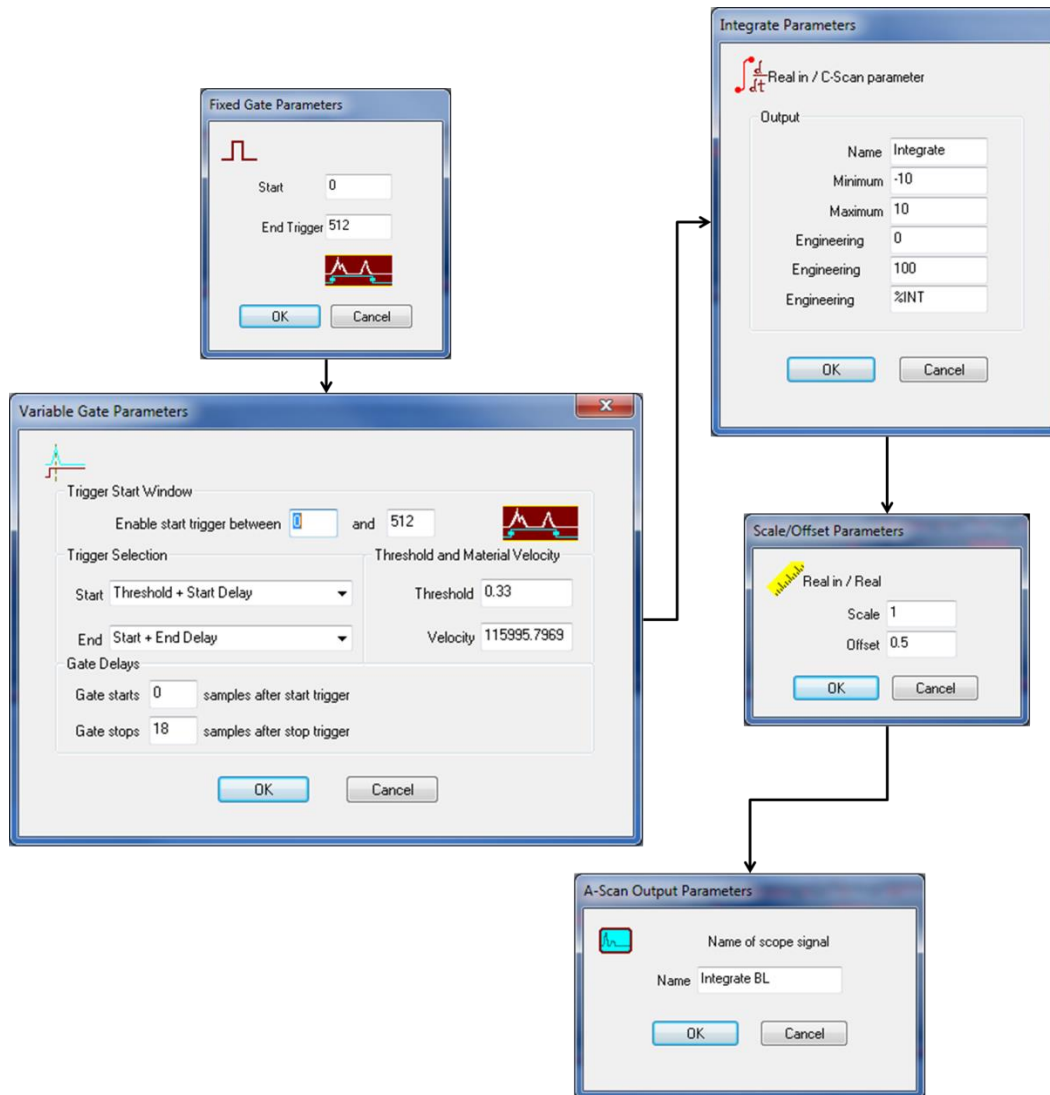


Figure 87: Integrate algorithm workflow

First, the fixed gate was set to incorporate all of the sampled data from 0 to 512 samples. A variable gate was then set at a threshold of 0.33 volts starting at 0 samples after the start trigger (i.e. threshold + start delay) and ending 18 samples after the stop trigger (i.e. start + end delay). All of the points within the variable gate were then integrated (i.e. summed) and set to display engineering units of %INT from 0 to 100. The post processed integrated waveform of the bondline (i.e. area adjacent to the peel ply insert) and selected peel ply insert are shown by the A-Scan scope in Figure 88. The resulting final algorithm is shown in Figure 89.

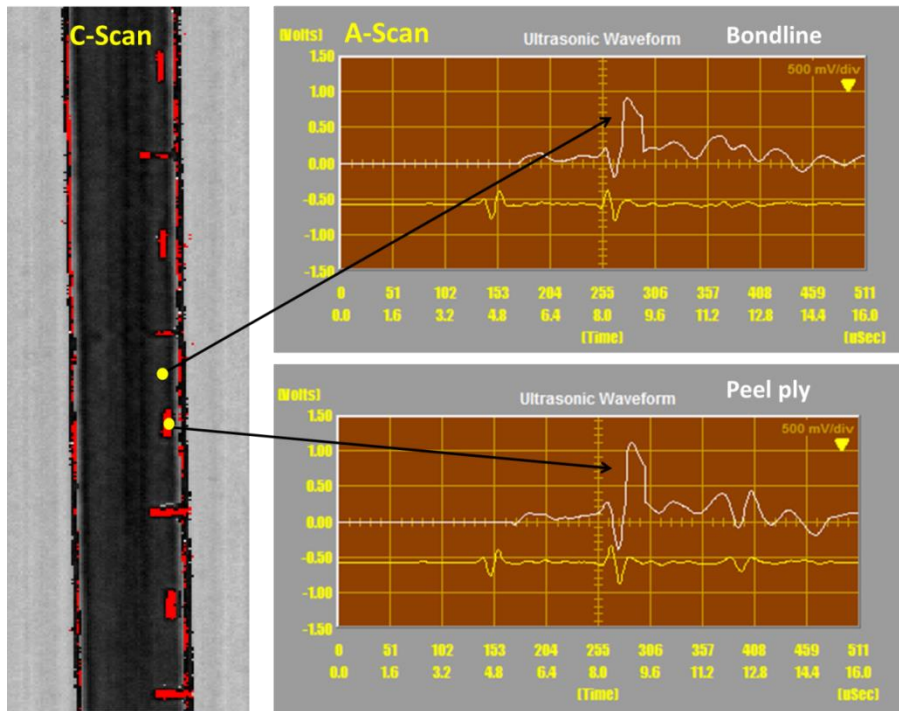


Figure 88: Post processed integration of the bondline and peel ply insert

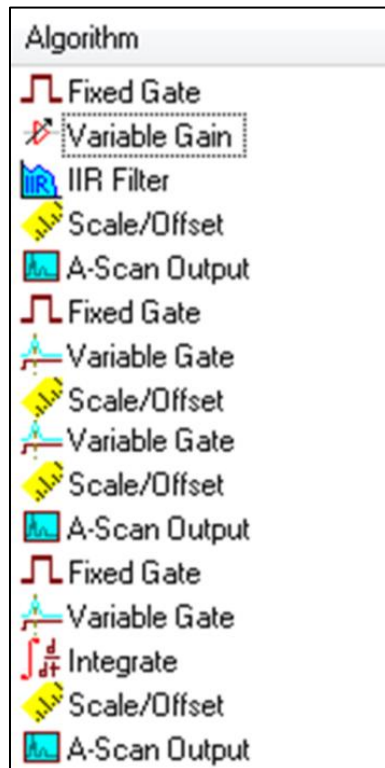


Figure 89: Final integration algorithm

CHAPTER 5

ANALYSIS AND RESULTS

5.1 Analysis

The following results include the amplitude data acquired by conventional gating techniques (i.e. from the setup in section 3.3.2) and the post processed data utilizing the final integration algorithm. The amplitude data is displayed in dB based on attenuation of the gated signal amplitude. The integration data is displayed as %INT (i.e. percent integration) based on the sum of all points in the gated signal. The data was output to individual C-Scan parameter tabs for further analysis. Figure 90 depicts the amplitude C-Scan of the peel ply inserts with the individual parameter tab (AmplBW). The edge of each insert is clearly defined at the 20 dB upper threshold; set to color red. Figure 91 depicts the integration C-Scan of the post processed data with the individual parameter tab (Integrate_XMT_pp). The area of each insert is clearly defined at the 88.00% integration threshold; set to color red.

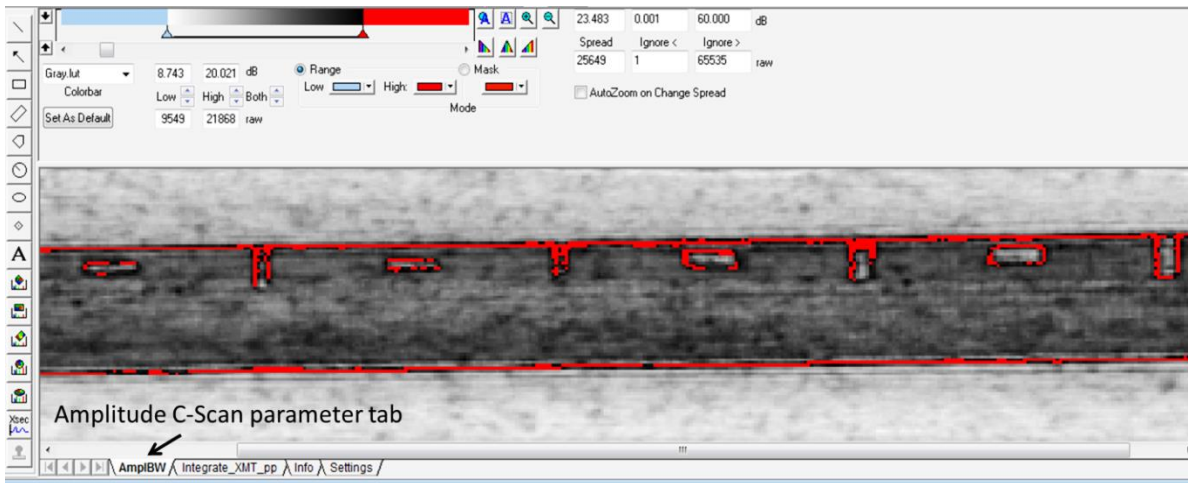


Figure 90: Amplitude C-Scan data with parameter tab (AmplBW)

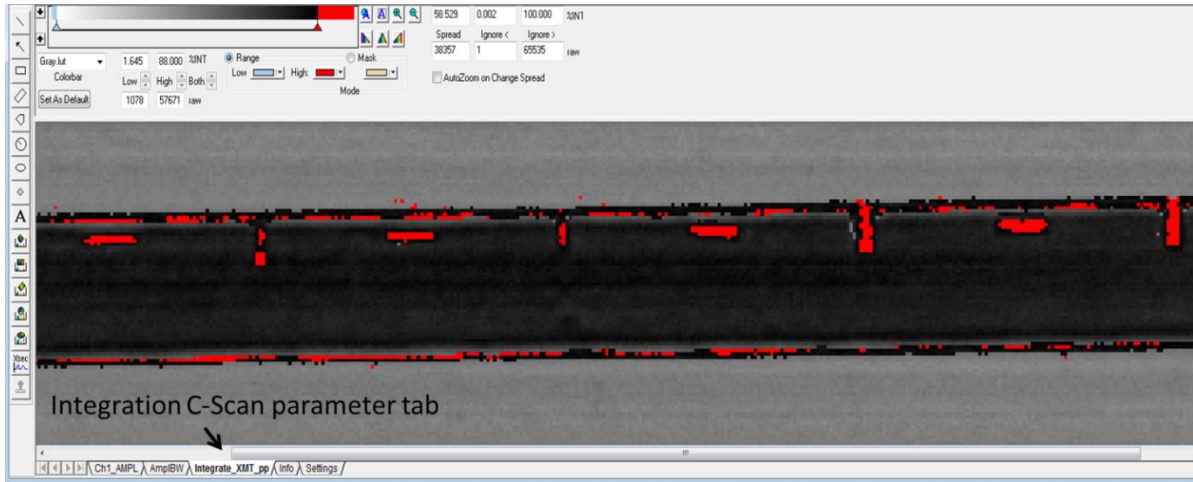
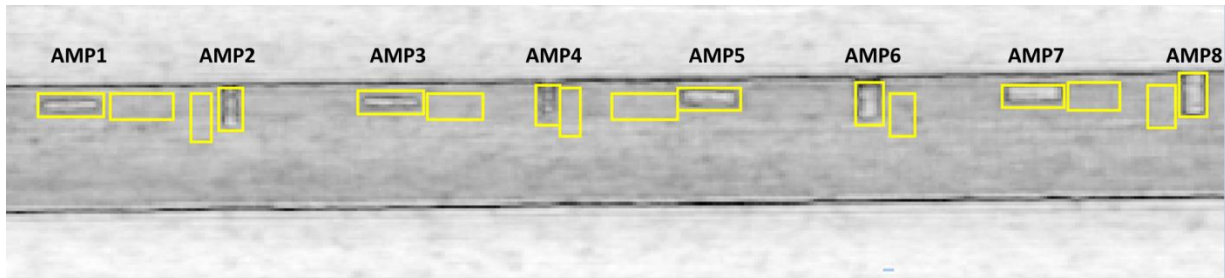
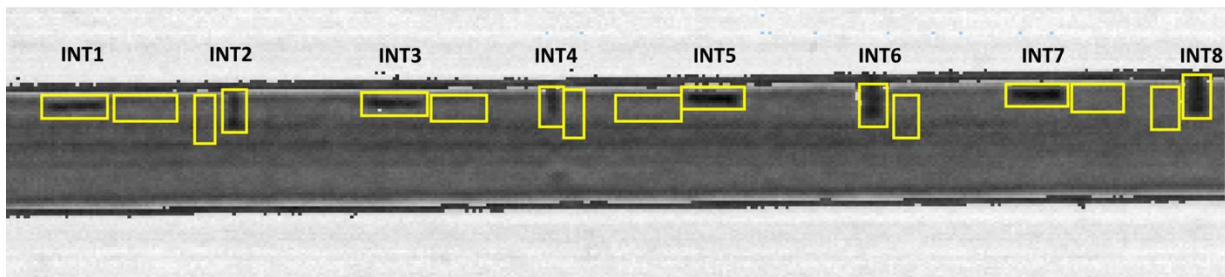


Figure 91: Integration C-Scan post processed data with parameter tab (*Integrate_XMT_pp*)

The peel ply inserts were identified on the C-Scan by AMP (i.e. amplitude) or INT (i.e. integration), shown in Figure 92. The polygon histograms placed around each insert (e.g. to include the entire area of each insert) and adjacent areas define the statistical data included within the polygon. The data was then analyzed and signal to noise ratios were calculated using the histogram statistics tool, shown in Figure 93.



(a)



(b)

Figure 92: Identification of peel ply inserts with histogram polygons on C-Scan by (a) amplitude and (b) integration

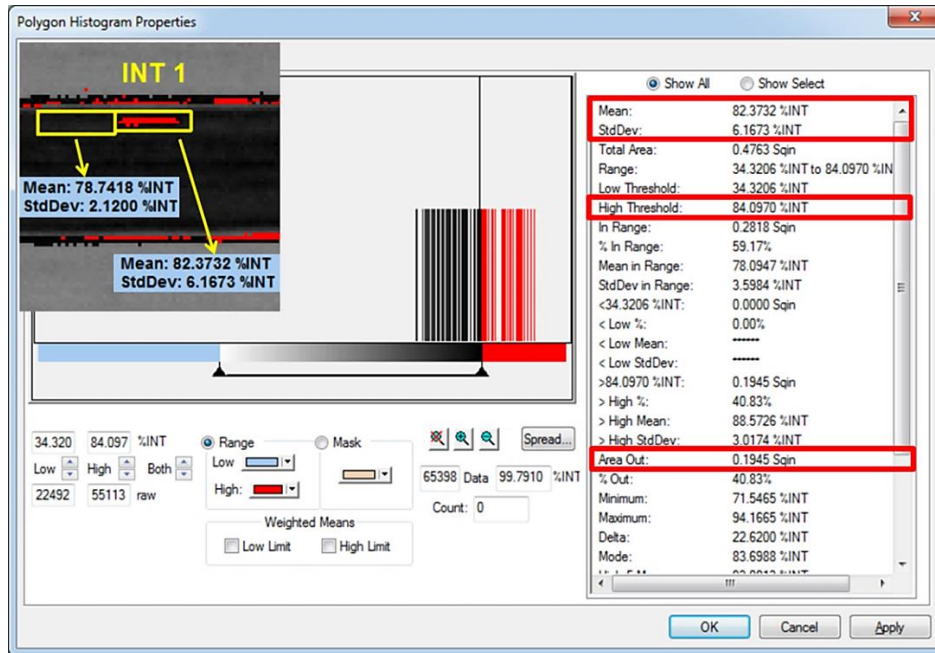


Figure 93: Histogram statistics tool displaying data from within the polygon

Inserts with length perpendicular to the OoA fabric preform extend beyond the edge of the preform by 0.15 inches. To provide accurate signal to noise ratios based on the area of the insert, signal reflections from the edge of the OoA fabric preform were excluded. Length of the inserts were taken as 0.85 inches long, shown in Figure 94.

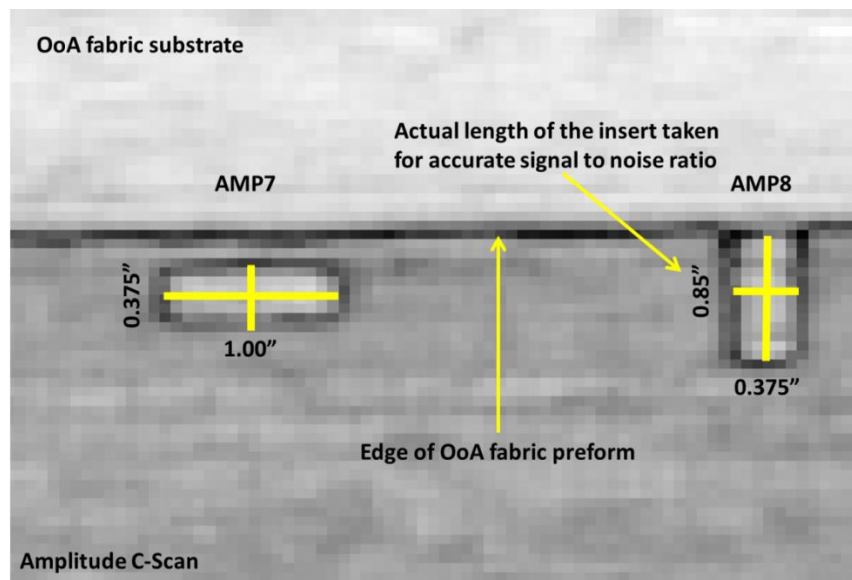


Figure 94: Length of inserts with length perpendicular to the edge of the OoA fabric preform

It is important to understand how the signals were gated to ensure accurate sizing and to obtain correct signal to noise results for both the amplitude and integrated data. The amplitude data is based on a single gate that starts after the front surface reflector capturing the signal amplitude as attenuation. The signal amplitude from the center of the insert is higher than the edge of the insert as previously mentioned in section 3.3.3. Figure 95 shows an illustration of the amplitude gate and the signal amplitude from the edge and center of the insert.

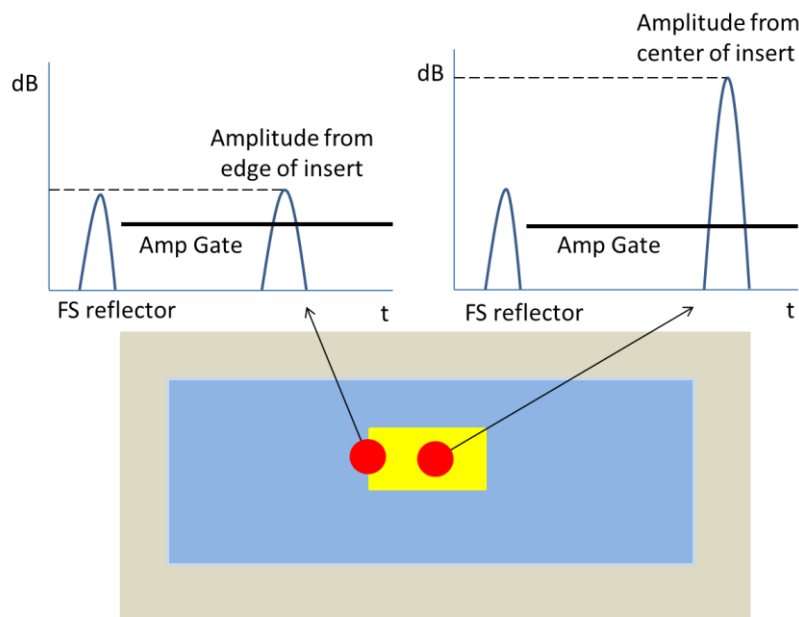


Figure 95: Illustration of the amplitude gate and the signal amplitude from both the edge and center of the insert

Consequently, there are two sets of data resulting in a histogram with bimodal distribution illustrating low signal attenuation (i.e. set to color blue), from the center of the insert and high signal attenuation (i.e. set to color red), from the edge, shown in Figure 96. Furthermore, the area of low attenuation is an accurate size of the insert. Figure 97 shows the AMP1 peel ply insert with high attenuation areas from the edge of the insert extending beyond the actual size. Areas in blue beyond the edge of the insert are low attenuation areas from the bondline and are similar to the peel ply insert.

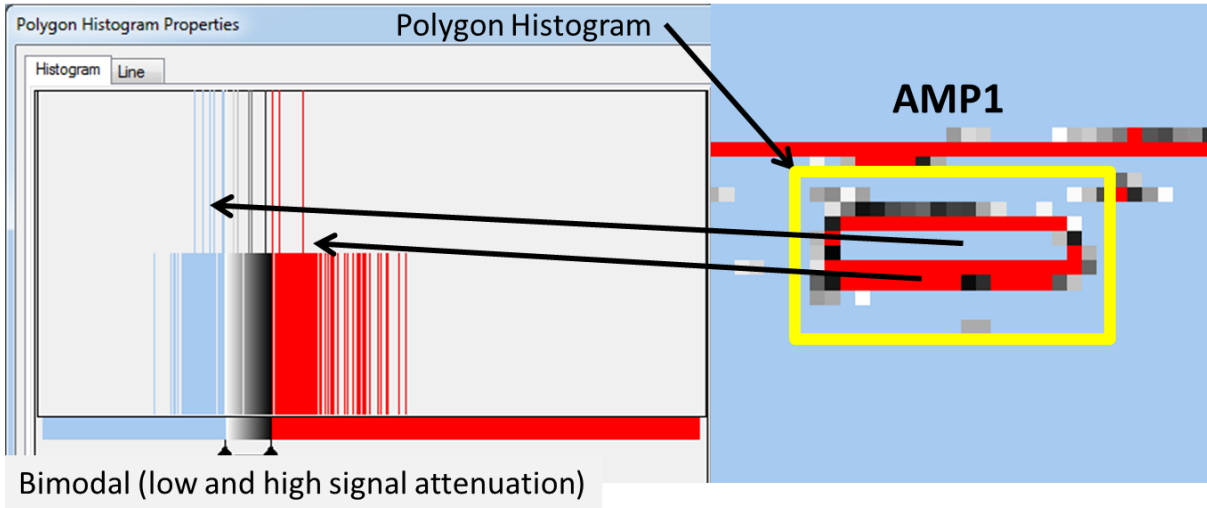


Figure 96: Bimodal histogram with low and high signal attenuation

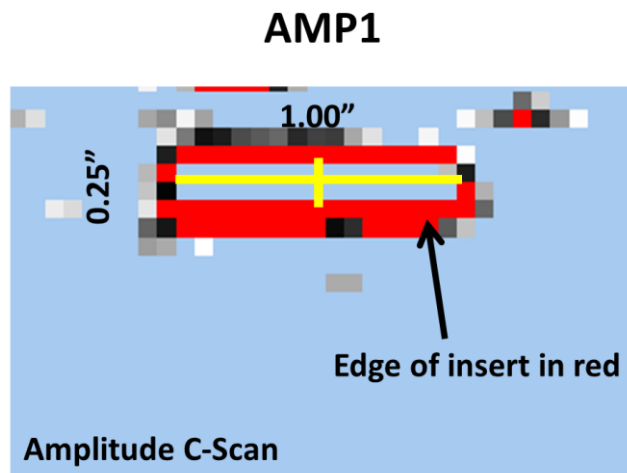


Figure 97: AMP1 insert with high attenuation extending beyond the actual size

The integrated data is based on a running sum of the all points in the original signal, based on the signal amplitude shown in Figure 98. The result is a unimodal distribution of an accurately sized insert with areas in red above the upper threshold, shown in Figure 99.

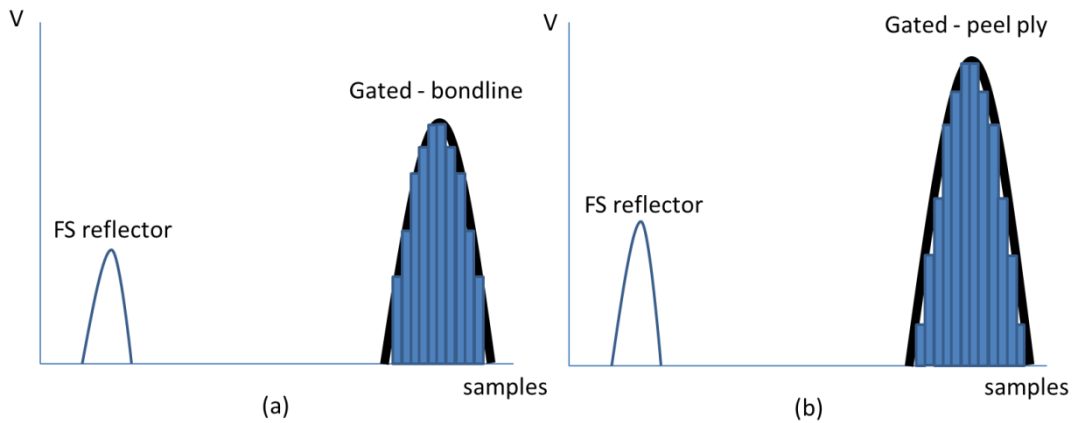


Figure 98: Integrated signals from the (a) gated bondline and (b) the gated peel ply

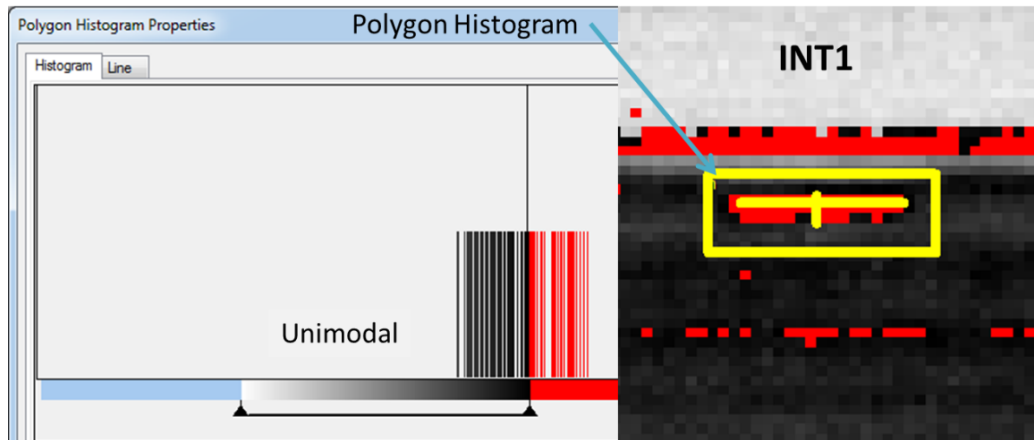


Figure 99: Unimodal histogram with an accurately sized insert using upper threshold

5.2 Results

Upon analysis, the signal to noise ratio of the amplitude data was calculated using the lower threshold (i.e. set to color blue) as the mean value of the insert and the signal to noise ratio of the integrated data was calculated using the upper threshold (i.e. set to color red) as the mean value of the insert. Figure 100 shows the amplitude C-Scan data of each insert, using the lower threshold. Figure 101 shows the integrated C-Scan data of each insert, using the upper threshold. Each display the polygon histograms and statistical values used to calculate the signal to noise ratios.

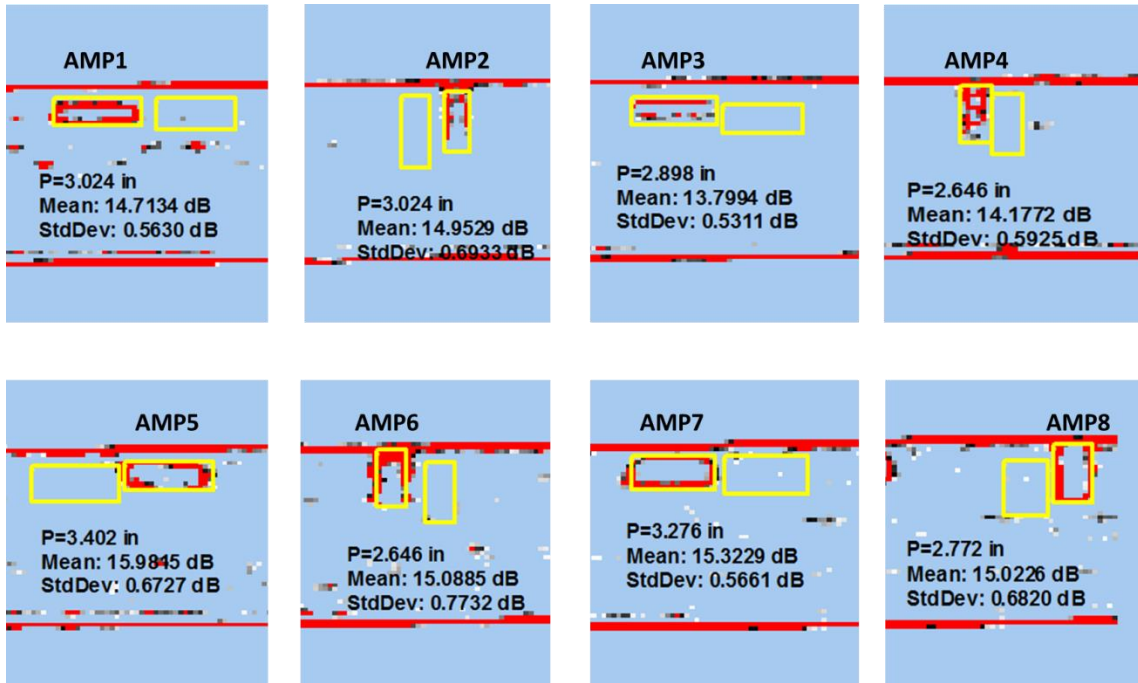


Figure 100: Amplitude C-scan with statistical values for each insert using the lower threshold

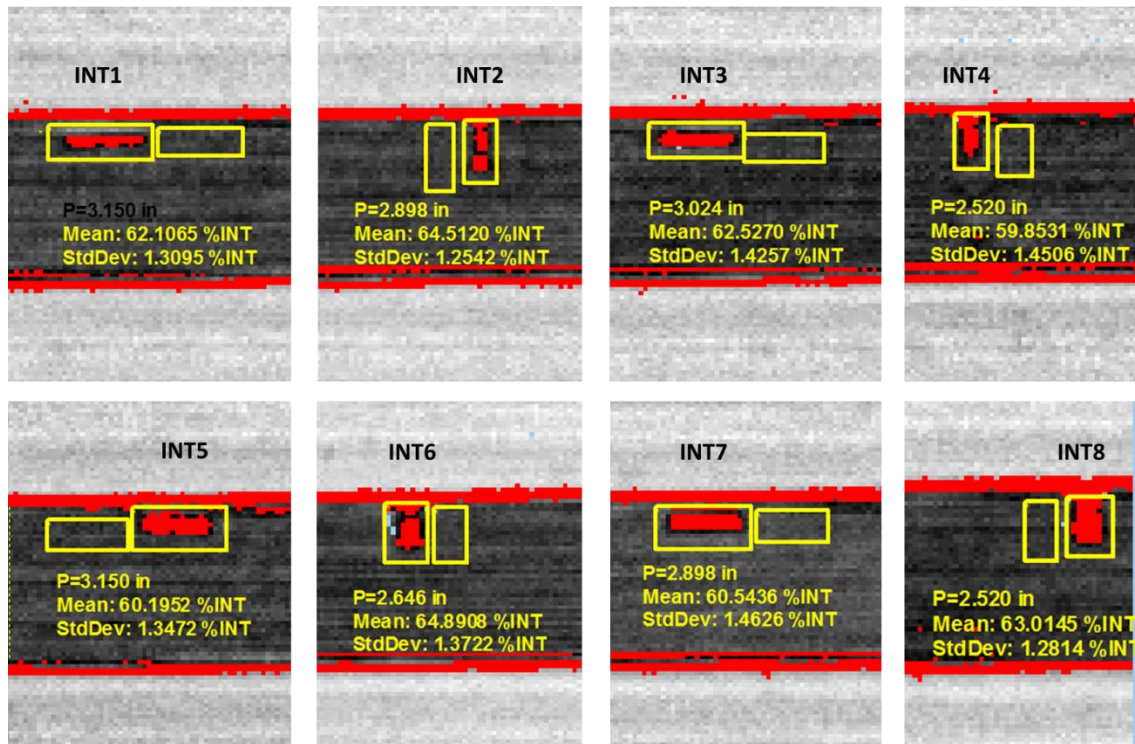


Figure 101: Integrated C-Scan with statistical values for each insert using the upper threshold

Table 2

Peel ply insert signal to noise ratio summary

Insert ID	Background Mean (Amplitude) or (% INT)	Background Standard Deviation (Amplitude) or (% INT)	Actual Area [sq inch]	MAXIMUM Reject Threshold to size inserts at $\pm 25\%$ (inch)	Signal Level	MAXIMUM Signal-to-Noise Ratio
AMP 1	14.7134	0.5630	0.250	15.89	-1.18	2.09
AMP 2	14.9529	0.6933	0.213	17.08	-2.13	3.07
AMP 3	13.7994	0.5311	0.250	15.45	-1.65	3.11
AMP 4	14.1772	0.5925	0.213	16.19	-2.01	3.39
AMP 5	15.9815	0.6727	0.375	18.28	-2.30	3.42
AMP 6	15.0885	0.7732	0.319	18.72	-3.63	4.70
AMP 7	15.3229	0.5661	0.375	16.73	-1.41	2.49
AMP 8	15.0226	0.6820	0.319	16.63	-1.61	2.36
INT 1	62.1065	1.3095	0.250	68.72	-6.61	5.05
INT 2	64.5120	1.2542	0.213	71.90	-7.39	5.89
INT 3	62.5270	1.4257	0.250	68.33	-5.80	4.07
INT 4	59.8531	1.4506	0.213	66.11	-6.26	4.31
INT 5	60.1952	1.3472	0.375	65.67	-5.47	4.06
INT 6	64.8908	1.3722	0.319	72.91	-8.02	5.84
INT 7	60.5436	1.4626	0.375	68.70	-8.16	5.58
INT 8	63.0145	1.2814	0.319	68.32	-5.31	4.14

Table 2 shows the summary of signal to noise ratio results for the peel ply inserts. The acceptable signal to noise ratios that exceed 3:1 are indicated with a green background in the far right column. The majority of the inserts that were inspected with the amplitude setup did meet the specified 3:1 SNR; however, AMP1, AMP7 and AMP8 did not. Three of the peel ply inserts did not provide sufficient signal response, compared to the bondline with the background noise of the out-of-autoclave material. In other words, there was not enough difference between the maximum reject threshold and the background mean to overcome the background standard deviation with gating the amplitude alone. Therefore, a wide amplitude gate alone does not meet the inspection requirements. On the other hand, it can be seen that all of the inserts, INT1 through INT8, did exceed a 4:1 SNR. This proves that low pass filtering and integrating the

signal within a finite gate significantly improves the peel ply signal response, compared to the bondline through the out-of-autoclave material.

A comparison between the peel ply inserts sized at 0.25" x 1.00" and 0.375" x 1.00" is shown in Figure 102 and Figure 103, respectively.

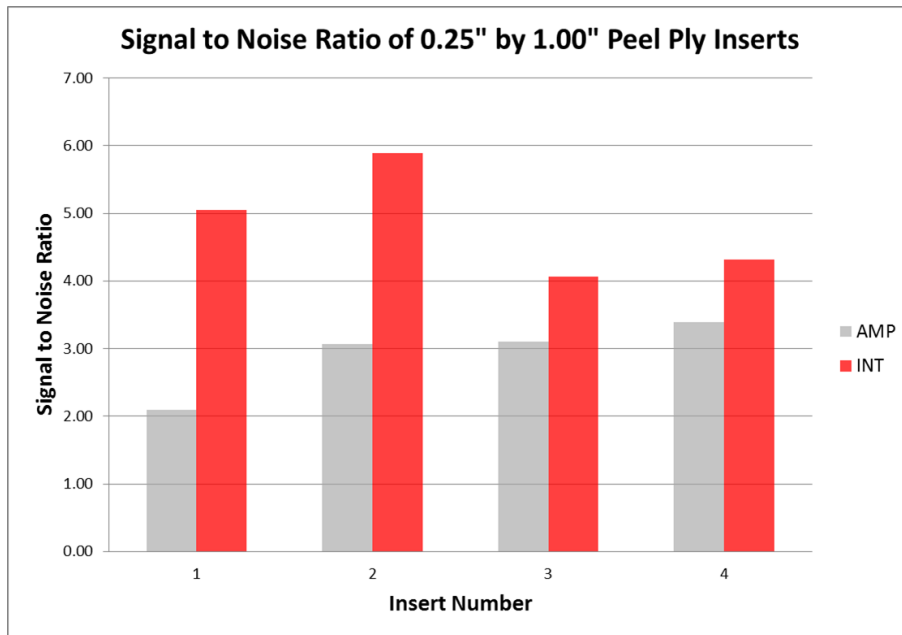


Figure 102: Signal to noise ratio of 0.25" by 1.00" peel ply inserts

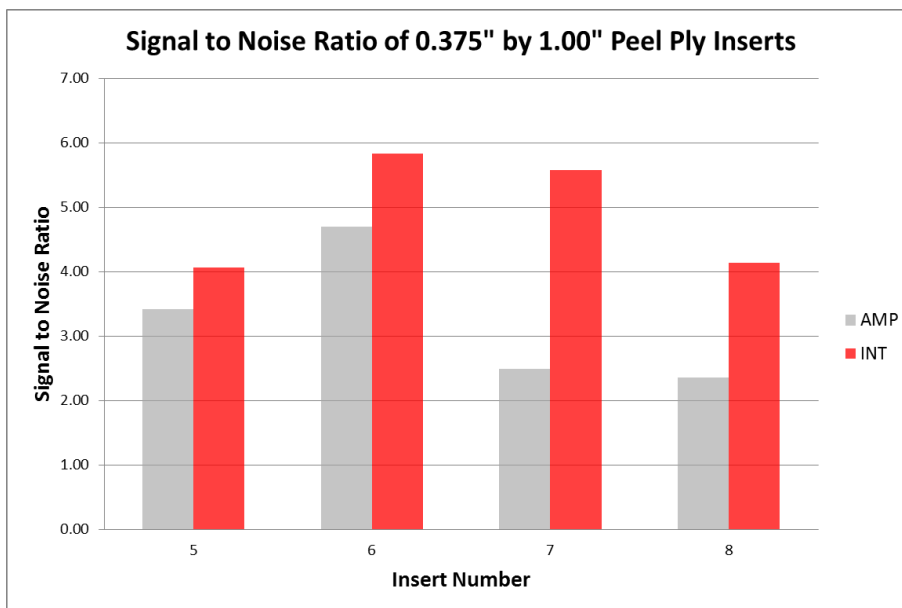


Figure 103: Signal to noise ratio of 0.375" by 1.00" peel ply inserts

The integrated data with the greatest signal to noise ratios were 5.89 and 5.84 for the INT2 and INT6 peel ply inserts, respectively. For each of these inserts the background standard deviation was lower compared to the mean. In contrast, AMP2 and AMP6 inserts had the highest standard deviations. The difference was likely due to the unfiltered signal and the wide amplitude gate compared to the filtered signal within the finite gate. Again, this proves the unnecessary noise was eliminated and the integrated signal, within the finite gate, provided for a lower standard deviation compared to the mean. The integrated signals with the lowest signal to ratios were 4.06 and 4.07 for the INT5 and INT3 peel ply inserts, respectively. These inserts did not exceed beyond the edge of the fabric preform and may have been partially bonded in.

Finally, care was taken when sizing each insert and the utilization of appropriate thresholds to ensure accurate results. The results conclude that the signal to noise ratio of each peel ply insert was enhanced with the integration algorithm exceeding the industry standard SNR of 3:1.

CHAPTER 6

CONCLUSION

This research provides a detailed analysis into the influence of out of autoclave materials assembled together with film adhesives and the reliability of finding finite peel ply inserts at the bondline with ultrasonic inspection. The critical aspects of the effects of foreign materials at the bondline of composite assemblies are identified. This research addresses ongoing problems with successfully identifying foreign materials with a similar acoustic impedance response as the bondline with ultrasonic methods. Novel ultrasonic signal processing techniques have been established to provide a better representation of the peel ply inserts post inspection. A method of measuring the signal to noise ratio, between non relevant, extraneous signals from the background and inserts of a finite size, is presented. The method relies on correct sizing, appropriate thresholds, and principles of statistical measurement to provide accurate signal to noise ratios from a representative reference standard to meet the industry standard of 3:1.

The reference standard was manufactured to include peel ply inserts of predetermined minimum detectable sizes at one side of the bonded interface, between an out-of-autoclave fabric substrate and preform. The research concluded that ultrasonic testing is the most comprehensively approved and suitable nondestructive test method to identify and quantify the inserts. The selected ultrasonic system was appropriately configured to perform the inspection of the manufactured reference standard. Post inspection analysis of the reflection response from the peel ply inserts and the bondline was conducted, utilizing the frequency and time domain of the ultrasonic waveform to determine regions of interest.

For this research, a novel integration algorithm was developed through function menus to provide a C-Scan output parameter detailing the peel ply inserts on one side of the bonded

interface. Such algorithms have never been established to improve the detection of peel ply at either of the bonded interfaces of out-of-autoclave assemblies of this configuration. Function menus with user defined parameters were established to accomplish signal conditioning and gating techniques to generate the desired output parameter. A low pass filter and signal amplification, via scaling, was performed to further condition the region of interest, based on analysis of the frequency domain. The theory of mathematical integration was executed post signal conditioning; providing the most distinguishable output, based on the region of interest, as a result of the time domain analysis.

Ultrasonic amplitude data acquired by conventional gating techniques were compared to data that were post processed with the final integration algorithm. The resulting data was output to individual C-Scans for further analysis with existing evaluation software. Initial assessment with color thresholds revealed the edge of each insert in the amplitude C-Scan and the area of the insert in the integration C-Scan. Further analysis revealed sizing issues due to reflections from the edge of the inserts and the edge of OoA fabric preform and was accounted for.

Polygon histograms were implemented and sized appropriately to acquire the mean and standard deviation of the peel ply inserts and areas adjacent as the background. The signal to noise ratio between each insert and the background were calculated for both the amplitude and integration with lower and upper thresholds, respectively. The calculated results conclude that the signal conditioning and the theory of applying integration over the region of interest did improve the signal to noise ratio of the peel ply inserts, based on the reference standard.

This concludes the difficulty of ultrasonically identifying and differentiating between materials of similar acoustic impedance in out-of-autoclave composite assemblies. As the technology moves in the direction of less expensive manufacturing and assembly processes, it is

imperative to continue the research to establish and ensure conclusive nondestructive test methods to meet the measure of detectability established by governing specifications of aerospace structures. The methods and results of this work will be incorporated into the manufacturing process as an approved ultrasonic inspection technique fulfilling all established requirements for the assembly under consideration.

CHAPTER 7

FUTURE WORK

The reference standard was designed as a prototype, based on the problem statement and established requirements. For simplicity and success, it was determined to place the peel ply inserts on only one side of the bondline to support the theory and the design of the algorithm, as an initial solution. Now that the theory was proven and the initial algorithm was successful an alternative reference standard will need to be manufactured with inserts incorporated on both sides of the bondline. Based on the developed algorithm, an additional working algorithm will need to be developed that is capable of detecting the peel plies on each side of the bondline. Finally, more reference standards are necessary with geometries that further represent the final product. Once complete, the ultrasonic inspection and pulse processing techniques with the final algorithm must be proven as robust to consistently identify and size defects accurately to meet all customer requirements.

Technology is moving in the direction to replace mechanically fastened repairs with adhesively bonded scarf repairs, resulting in higher performance and restoring load-carrying capability [86]. The same bondline defects, inherent to bonded assemblies, also apply to bonded repairs. Hence, this ultrasonic inspection and post processing technique can also be applied to such repairs, specifically for out-of-autoclave materials. The gating scheme within the algorithm ensures that the varying bondline signal is captured in conjunction with the taper of the scarf repair. Further analysis with this inspection technique would ensure the capability to identify defects inherent to adhesively bonded scarf repairs of OoA materials.

In an effort to find a faster and a cost-effective NDT solution, further research regarding alternative NDT methods, other than ultrasonic testing, is needed. Methods such as laser bond

inspection and infrared thermography have been proven as an alternative solution for inspection of composite materials of finite thicknesses but they cannot be as effective when the thickness exceeds certain limits. To compete with ultrasonic testing, future research and development is necessary to overcome these thickness limitations. Once a method is proven to be successful, it must be justified and certified so that customers will accept it and implement it is an equivalent process.

REFERENCES

REFERENCES

- [1] Askari, Davood, Ghasemi-Nejhad, & Mehrdad N. (2012). Effects of Vertically Aligned Carbon Nanotubes on Shear Performance of Laminated Nanocomposite Bonded Joints. *Science and Technology of Advanced Materials*, 1-10. doi:10.1088/1468-6996/13/4/045002

- [2] Gardiner, G. (2011, January 1). Out-of-Autoclave Prepregs: Hype or Revolution. Retrieved July 20, 2016, from compositesworld.com: <http://www.compositesworld.com/articles/out-of-autoclave-prepregs-hype-or-revolution>

- [3] M.D. Banea, L. d. (2009). Adhesively Bonded Joints in Composite Materials: an Overview. *Proc. I Mech Eng L-J Mater*, 223(1), 1-18. doi:10.1243/14644207JMDA219

- [4] Sloan, J. (2015, June 1). *Out of Autoclave Processing: <1% void content*. Retrieved July 21, 2016, from CompositesWorld: <http://www.compositesworld.com/articles/out-of-autoclave-processing-1-void-content>

- [5] *Acoustic Impedance*. (2001-2016). Retrieved July 21, 2016, from NDT-ed: <https://www.nde-ed.org/EducationResources/CommunityCollege/Ultrasonics/Physics/acousticimpedance.php>

- [6] *Reflection and Transmission Coefficients*. (2001-2016). Retrieved July 21, 2016, from NDT-ed: <https://www.nde-ed.org/EducationResources/CommunityCollege/Ultrasonics/Physics/reflectiontransmission.php>

- [7] *Material Sound Velocities*. (2016). Retrieved November 15, 2016, from Olympus-ims: <http://www.olympus-ims.com/en/ndt-tutorials/thickness-gage/appendices-velocities/>

- [8] *Metals and Alloys - Densities*. (2016). Retrieved November 15, 2016, from engineeringtoolbox.com: http://www.engineeringtoolbox.com/metal-alloys-densities-d_50.html

- [9] *Air Density and Specific Weight*. (2016). Retrieved November 15, 2016, from engineeringtoolbox.com: http://www.engineeringtoolbox.com/air-density-specific-weight-d_600.html
- [10] *Performance Composite Mechanical Properties*. (2016). Retrieved November 17, 2016, from Performance Composites Ltd: http://www.performance-composites.com/carbonfibre/mechanicalproperties_2.asp
- [11] *Nylons (Polyamide) Properties*. (2016). Retrieved November 17, 2016, from British Plastics Federation: <http://www.bpf.co.uk/plastipedia/polymers/polyamides.aspx>
- [12] ASTM Standard E1495M. (2012). *Standard Guide for Acousto-Ultrasonic Assessment of Composites, Laminates, and Bonded Joints*. West Conshohocken, PA: ASTM International. doi:10.1520/E1495-12, www.astm.org
- [13] ASTM Standard D4762. (2011). *Standard Guide for Testing Polymer Matrix Composite Materials*. West Conshohocken, PA: ASTM International. doi: 10.1520/D4762-11A, www.astm.org
- [14] MIL-HDBK-787, Military Standardization Handbook: *Nondestructive Test Methods of Composite Materials – Ultrasonics*. Department of Defense. Washington, DC: US Department of the Army, April 1, 1988.
- [15] *Signal to Noise Ratio*. (2001-2016). Retrieved July 21, 2016, from NDT-ed: <https://www.nde-ed.org/EducationResources/CommunityCollege/Ultrasonics/Physics/signaltonoise.php>
- [16] Chien-Ping Chiou, F. J. (2016). Techniques and Software Tools for Estimating Ultrasonic Signal-to-Noise Ratios. *AIP Conference Proceedings 1706* (pp. 070012_1-10). Minneapolis, Minnesota: AIP Publishing. doi:10.1063/1.4940530
- [17] I.S. Floros, Tserpes, K. T., & Lobel, T. (2015, April 1). Mode-I, Mode-II and Mixed Mode I+II Fracture Behavior of Composite Bonded Joints: Experimental Characterization and Numerical Simulation. *Elsevier*, 459-468. doi:10.1016/j.compositesb.2015.04.006

- [18] Thompson, Bruce R. T. G. (1983, July 5). A Model Relating Ultrasonic Scattering Measurements Through Liquid-Solid Surfaces to Unbound Medium Scattering Amplitudes. *Ames Laboratory Publications*, pp. 1279-1290. doi:0001-4966/83/101279-125
- [19] ASTM Standard E2580. (2012). *Standard Practice for Ultrasonic Testing of Flat Panel Composites and Sandwich Core Materials Used in Aerospace Applications*. West Conshohocken, PA: ASTM International. doi:10.1520/E2580-12, www.astm.org
- [20] Workman, Gary L. "Introduction to Nondestructive Testing." *Nondestructive Testing Handbook*, third edition: Vol. 10. Patrick O. Moore, ed. Chap. 1. Columbus, OH: American Society for Nondestructive Testing (2012).
- [21] The American Society of Nondestructive Testing. (2016). *Introduction to Nondestructive Testing*. Retrieved July 30, 2016, from asnt.org: <https://www.asnt.org/MinorSiteSections/AboutASNT/Intro-to-NDT>
- [22] Aastroem, T. (2008). From Fifteen to Two Hundred NDT - Methods in Fifty Years. *World Conference on Non-Destructive Testing*, (pp. 1-13). Shanghai, China.
- [23] Training Guidelines in Non-Destructive Testing Techniques . (2013, June). *Manual for Visual Testing at Level 2*. Vienna, Italy: International Atomic Energy Agency.
- [24] *Advantages and Disadvantages of Penetrant Testing*. (2001-2016). Retrieved July 23, 2016, from NDT-ed: <https://www.nde-ed.org/EducationResources/CommunityCollege/PenetrantTest/Principles/prosandcons.php>
- [25] Moore, David G. "Liquid Penetrant Testing." *Nondestructive Testing Handbook*, third edition: Vol. 10. Patrick O. Moore, ed. Chap. 4. Columbus, OH: American Society for Nondestructive Testing (2012).
- [26] ASTM Standard E708. (2008). *Standard Guide for Magnetic Particle Testing*. West Conshohocken, PA: ASTM International. doi:10. 10.1520/E0709-15, www.astm.org

- [27] *Basic Principles – Magnetic Particle Inspection*. (2001-2016). Retrieved July 23, 2016, from NDT-ed: <https://www.nde-ed.org/EducationResources/CommunityCollege/MagParticle/Introduction/basicprinciples.php>
- [28] *Magnetic Particle Examination*. (2016). Retrieved October 2, 2016, from nationalboard.org: <http://www.nationalboard.org/index.aspx?pageID=164&ID=377>
- [29] NASA-SP-5113, Technology Utilization: *Nondestructive Testing – A Survey*. National Aeronautics and Space Administration. Washington, DC: US Southwest Research Institute, January 1, 1973
- [30] Staats, H.N. “Brittle Coating Tests.” *Nondestructive Testing Handbook*, first edition. R.C. McMaster, ed. Sec. 52. Columbus, OH: American Society for Nondestructive Testing (1959).
- [31] *Basic Principles – Eddy Current Inspection*. (2001-2016). Retrieved July 24, 2016, from NDT-ed: <https://www.nde-ed.org/EducationResources/CommunityCollege/EddyCurrents/Introduction/IntroductiontoET.htm>
- [32] Bossi, Richard H. “Radiographic Testing.” *Nondestructive Testing Handbook*, third edition: Vol. 10. Patrick O. Moore, ed. Chap. 7. Columbus, OH: American Society for Nondestructive Testing (2012).
- [33] *Real-time Radiography*. (2001-2016). Retrieved July 24, 2016, from NDT-ed: <https://www.nde-ed.org/EducationResources/CommunityCollege/Radiography/AdvancedTechniques/realtime.htm>
- [34] Garrett, W.R., Splettstosser, H.R., & Titus, D.E. “Radiography in Modern Industry.”, fourth edition. Richard A. Quinn, Claire C Sigl, ed. Rochester, NY: Eastman Kodak Company (1980).
- [35] Iddings, Richard H., Wheeler, Frank A., & Moore, George C. “Radiographic Testing.” *Nondestructive Testing Handbook*, third edition, Vol. 4. Patrick O Bossi, ed. Columbus, OH: American Society for Nondestructive Testing (2002).

- [36] Hellier, Charles J. “Radiographic Testing.” *Handbook of Nondestructive Evaluation*, first edition. Kenneth McCombs, ed. Chap. 6. New York, NY: McGraw Hill (2001).
- [37] Workman, Gary L. “Ultrasonic Testing.” *Nondestructive Testing Handbook*, third edition: Vol. 10. Patrick O. Moore, ed. Chap. 10. Columbus, OH: American Society for Nondestructive Testing (2012).
- [38] Hellier, Charles J. “Ultrasonic Testing.” *Handbook of Nondestructive Evaluation*, first edition. Kenneth McCombs, ed. Chap. 7. New York, NY: McGraw Hill (2001).
- [39] Schmerr, Lester W. Jr. (2016) “Fundamentals of Ultrasonic Nondestructive Evaluation – A Modeling Approach.” *Springer Series in Measurement Science and Technology*”, second edition. Markys G Cain, Giovanni Battista Rossi, Jiri Tesar, Marijn van Veghel, ed. Switzerland: Springer International Publishing (2016).
- [40] *Basic Principles of Ultrasonic Testing*. (2001-2016). Retrieved August 10, 2016, from NDT-ed: <https://www.nde-ed.org/EducationResources/CommunityCollege/Ultrasonics/Introduction/description.php>
- [41] Hsu, D. (2013). Non-destructive Evaluation (ND) of Aerospace Composites: Ultrasonic Techniques. “*Non-Destructive Evaluation (NDE) of Polymer Matrix Composites*” (pp. 397-422). V. M. Karbhari, & V. M. Karbhari ed. Arlington, TX: Woodhead Publishing. doi:10.1533/9780857093554.3.397
- [42] *Air-coupled Ultrasound – A Millennial Review*. (1999). Retrieved August 10, 2016, from ndt.net: <http://www.ndt.net/article/wcndt00/papers/idn507/idn507.htm>
- [43] Leone, Frank A. Jr., Ozevin, Didem, Godinez, Valery, Mosinyi, Bao, Bakuckas, John G. Jr., Awerbuch, Jonathan, Lau, Alan, & Tan, Tein-Min. (2008). Acoustic Emission Analysis of Full-Scale Honeycomb Sandwich Composite Curved Fuselage Panels. *Nondestructive Characterization for Composite Materials, Aerospace Engineering, Civil Infrastructure, and Homeland Security*, (pp. 1-16). San Diego, CA. doi:10.1117/12.776146
- [44] *Introduction to Acoustic Emission Testing*. (2001-2016). Retrieved July 29, 2016, from NDT-ed: https://www.nde-ed.org/EducationResources/CommunityCollege/Other%20Methods/AE/AE_Intro.php

- [45] Miller, Ronnie K., & Hill, Eric. "Acoustic Emission Testing." *Nondestructive Testing Handbook*, third edition: Vol. 6. Patrick O. Moore, ed. Chap. 2. Columbus, OH: American Society for Nondestructive Testing (2005).
- [46] Smith, R. (2009). *Materials Science and Engineering*. Retrieved September 5, 2016, from desware.net: <http://www.desware.net/sample-chapters/d07/E6-36-04-03.pdf>
- [47] Waugh, R. C. "Adhesive Bonding." *Development of Infrared Techniques for Practical Defect Identification in Bonded Joints*, Switzerland: Springer International Publishing (2012).
- [48] Sherafat, M. H., Guitel, R., Quaegebeur, N., Hubert, P., Lessard, L., & Masson, P. (2016). Structural Health Monitoring of a Composite Skin-Stringer Assembly Using Within-the-Bond Strategy of Guided Wave Propagation. *Materials & Design*, 90, 787-794. doi:10.1016/j.matdes.2015.11.018
- [49] Whittingham, B., Li, H. C. H., Herszberg, I., & Chiu, W. K. (2006). Disbond Detection in Adhesively Bonded Composite Structures Using Vibration Signatures. *Composite Structures*, 75(1), 351-363. doi:10.1016/j.compstruct.2006.04.055
- [50] Bernasconi, A., Kharshiduzzaman, M., & Comolli, L. (2016). Strain Profile Measurement for Structural Health Monitoring of Woven Carbon-fiber Reinforced Polymer Composite Bonded joints by Fiber Optic Sensing Using an Optical Backscatter Reflectometer. *The Journal of Adhesion*, 92(6), 440-458. doi:10.1080/00218464.2015.1043005
- [51] Zhou, W., Liu, R., Lv, Z. H., Chen, W. Y., & Li, X. T. (2015). Acoustic Emission Behaviors and Damage Mechanisms of Adhesively Bonded Single-lap Composite Joints with Adhesive Defects. *Journal of Reinforced Plastics and Composites*, 34(1), 84-92. doi:10.1177/0731684414563112
- [52] Bak, K. M., Kalaichelvan, K., Jothilingam, A., & RajendraBoopathy, S. (2016). Acoustic Emission Characterization of Failure Modes of Single-lap Joints in Glass/Epoxy Specimens. *Journal of Composite Materials*, 50(1), 3-23. doi:10.1177/0021998315569749

- [53] Sherafat, M. H., Guitel, R., Quaegebeur, N., Lessard, L., Hubert, P., & Masson, P. (2016). Guided Wave Scattering Behavior in Composite Bonded Assemblies. *Composite Structures*, 136, 696-705. doi:10.1016/j.compstruct.2015.10.046
- [54] Yoo, B., Na, S. M., Flatau, A. B., & Pines, D. J. (2015). Ultrasonic Guided Wave Sensing Performance of a Magnetostrictive Transducer using Galfenol Flakes-Polymer Composite Patches. *Journal of Applied Physics*, 117(17), 17A916. doi:10.1063/1.4916811
- [55] *NDI and NDT Methods for Process Control*. (2014). Retrieved September 22, 2016, from CompositesWorld.com: <http://www.compositesworld.com/articles/ndi-and-ndt-methods-for-process-control>
- [56] *Certification of Bonded Composite Primary Structures*. (2014). Retrieved September 22, 2016, from CompositesWorld.com: <http://www.compositesworld.com/articles/certification-of-bonded-composite-primary-structures>
- [57] *LSP Technologies*. (2014). Retrieved September 22, 2016, from lspstechnologies.com: <http://www.lspstechnologies.com/lbi-application-development.php>
- [58] Ghali, Venkata S., Mulaveesala, Ravibabu. (2011). Comparative Data Processing Approaches for Thermal Wave Imaging Techniques for Non-Destructive Testing. *Sense Imaging*, 12-15. doi:10.1007/s11220-011-0059-0
- [59] Raakesh Raman, Alok Thakur. (1982). Thermal Emissivity of Materials. *Applied Energy*, vol 12, issue 3, pg. 205-220. doi:10.1016/0306-2619(82)90039-3
- [60] Genest, M., Martinez, M., Mrad, N., Renaud, G., Fahr, A. (2009). Pulsed Thermography for Non-Destructive Evaluation and Damage Growth Monitoring of Bonded Repairs. *Composite Structures*, 112-120. doi:10.1016/j.compstruct.2008.02.010
- [61] *Infrared Thermography as a Non-Destructive Tool for Materials Characterisation and Assessment*. (2011). Retrieved September 25, 2016, from twi-global.com: <http://www.twi-global.com/technical-knowledge/published-papers/infrared-thermography-as-a-non-destructive-tool-for-materials-characterisation-and-assessment/>

- [62] Benzerrouk, Souheil. (2011). Active and Passive Thermography for the Detection of Defects in Green-State Powdermetallic Compacts. *Dissertation submitted to Worcester Polytechnic Institute*, pg. 35-42.
- [63] Shin, P. H., Webb, S. C., & Peters, K. J. (2016). Pulsed phase thermography imaging of fatigue-loaded composite adhesively bonded joints. *NDT & E International*, 79, 7-16. doi:10.1016/j.ndteint.2015.11.008
- [64] Vinod, P. N., Joseph, S., & John, R. (2016). The detection and quantification of the defects in adhesive bonded joints of the piezoelectric sensors by infrared thermographic nondestructive testing. *Nondestructive Testing and Evaluation*, 1-15. doi:10.1080/10589759.2016.1159305
- [65] Wu, X., & Peters, K. (2015). Non-Destructive Inspection of Adhesively Bonded Joints using Amplitude Modulated Thermography. *Experimental Mechanics*, 55(8), 1485-1501. doi:10.1007/s11340-015-9997-0
- [66] Homin Song, Hyung Jin Lim, Sangmin Lee, Hoon Sohn, Wonjun Yun, Eunha Song. (2015). Automated Detection and Quantification of Hidden Voids in Triplex Bonding Layers Using Active Lock-In Thermography. *NDT&E International*, 94-105. doi:10.1016/j.ndteint.2015.05.004
- [67] Palumbo, Davide, Tabborrino, Rosanna, Umberto, Galietti, V.A.M., Luprano. (2015). Ultrasonic Analysis and Lock-In Thermography for Debonding Evaluation of Composite Adhesive Joints. *NDT&E International*, 2-26. doi: 10.1016/j.ndteint.2015.09.001
- [68] Liu, B., Zhang, H., Fernandes, H., & Maldague, X. (2016). Quantitative Evaluation of Pulsed Thermography, Lock-in Thermography and Vibrothermography on Foreign Object Defect (FOD) in CFRP. *Sensors (Basel, Switzerland)*, 16(5), 743. doi:10.3390/s16050743
- [69] Moore, David G. "Infrared and Thermal Testing." *Nondestructive Testing Handbook*, third edition: Vol. 10. Patrick O. Moore, ed. Chap. 6. Columbus, OH: American Society for Nondestructive Testing (2012).

- [70] Ehrhart, Bastien, Bockenheimer, C., & Valeske, Bernd. “Non-Destructive Evaluation (NDE) of Aerospace Composites: Methods for Testing Adhesively Bonded Composites.” *Non-Destructive Evaluation (NDE) of Polymer Matrix Composites*, pp.220-237. Cambridge, UK: Woodhead Publishing Limited (2013).
- [71] *Measurement Principles of Shearography* (2013). Retrieved September 30, 2016, from dantecdynamics.com: <http://www.dantecdynamics.com/measurement-principles-of-shearography>
- [72] *Digital Shearographic Non-Destructive Testing Laboratory* (2016). Retrieved September 30, 2016, from secs.oakland.edu: <http://secs.oakland.edu/~yang2/linkfile/Shearographic%20Non-destructive%20Testing%20Laboratory.pdf>
- [73] Katnam, K.B., DaSilva, L.F.M., Young, T.M. (2013). Bonded Repair of Composite Aircraft Structures: A review of Scientific Challenges and Opportunities. *Science Direct*, 26-42. doi:10.1016/j.paerosci.2013.03.003
- [74] ASTM Standard E2533. (2009). *Standard Guide for Nondestructive Testing of Polymer Matrix Composites Used in Aerospace Applications*. West Conshohocken, PA: ASTM International. doi:10.1520/E2533-09., www.astm.org
- [75] Lamboul, B., Giraud, O., & Osmont, D. (2015). Detection of disbonds in foam composite assemblies using flexural waves and shearography. *41ST ANNUAL REVIEW OF PROGRESS IN QUANTITATIVE NONDESTRUCTIVE EVALUATION: Volume 34* (Vol. 1650, No. 1, pp. 1155-1161). AIP Publishing
- [76] Ma, B., Zhou, Z., Zhao, H., Zhang, D., & Liu, W. (2015). Characterisation of inclusions and disbonds in honeycomb composites using non-contact non-destructive testing techniques. *Insight-Non-Destructive Testing and Condition Monitoring*, 57(9), 499-507. doi:10.1784/insi.2015.57.9.499
- [77] De Angelis G., Dati E. & Bernabei M (2016). Non Destructive Investigation of Disbonding Damage in Air Cooling Inlet Composite Panel Using Active Thermography and Shearography. *MAYFEB Journal of Material Science*, vol. 1, 10-20.

- [78] Dragan, K., Swiderski, W. (2009). Studying Efficiency of NDE Techniques Applied to Composite Materials in Aerospace Applications. *Eleventh Annual Conference of the Materials Research Society of Serbia, YUCOMAT 2009*.
- [79] Vijayakumar, R.L., Bhat, M.R., & Murthy, C.R.L. (2012). Non Destructive Evaluation of Adhesively Bonded Carbon Fiber Reinforced Composite Lap Joints with Varied Bond Quality. *AIP Conference Proceedings*, 1430, doi:10.1063/1.4716365.
- [80] Adams, R.D., Cawley, P. (1988). A Review of Defect Types and Nondestructive Testing Techniques for Composites and Bonded Joints. *NDT International*, vol. 21, no. 4, pg.208-222.
- [81] Ehrhart, Bastien, Valeske, Bernd, Muller, Charles-Edouard, & Bockeneimer, Clemens. (2010). Methods for the Quality Assessment of Adhesive Bonded CFRP Structures – A Resume. *NDT in Aerospace, We.5.B.2*.
- [82] *Figure 16. Schematic of 8-Harness Satin Weave Fabric Laminates; a)...* - Scientific Figure on ResearchGate (2003). Retrieved October 27, 2016, from researchgate.net https://www.researchgate.net/figure/235072263_fig3_Figure-16-Schematic-of-8-Harness-Satin-Weave-Fabric-Laminates-a-Planform-and-b
- [83] *3D Multilayer Woven Fabric* (2014). Retrieved October 27, 2016, from 3dwovens.com <http://3dwovens.com/>
- [84] Smith, Steven W. “Convolution.” *The Scientists and Engineer’s Guide to Digital Signal Processing*, second edition. Chap. 6. San Diego, CA (1997).
- [85] *Ultrasound – Signal Processing Techniques*. (2001-2016). Retrieved November 05, 2016, from NDT-ed: <https://www.nde-ed.org/EducationResources/CommunityCollege/Ultrasonics/MeasurementTech/signalprocessing.php>
- [86] Katnam, K.B., Da Silva, L.F.M. and Young, T.M. (2013). Bonded Repair of Composite Aircraft Structures: A Review of Scientific Challenges and Opportunities. *Prog. Aerosp. Sci.*, vol. 61, pp. 26-42.

APPENDIX

APPENDIX

GE Inspection Technologies Phased Array Probe Specification

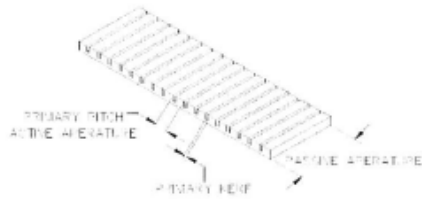
Linear Phased Array				
			inch	mm
Part Number	115-001-108	Primary Element Count	64	
Number of Elements	64	Primary Pitch	0.0630	1.6000
Frequency [MHz]	5	Primary Kerf	0.0035	0.0900
Connector	ITT Cannon 64 pin			
Cable Type	111-160-172 Coax, 38 Gauge, 50 Ohm, 68 Conductors			
Cable Length	8 Feet			
Total Crystal Size	102.4mm x 8mm			
			Element Passive Aperture	0.3150
				8.0000
Array Configuration	1D			
Notes	Array is fabricated @ 5.0MHz before hardwater materials are applied. Array is specified at 2.4-2.8MHz after the hardwater material is applied. .75" Radius with .5" Hardwater delay attached			

ITT Canon 64 Pin

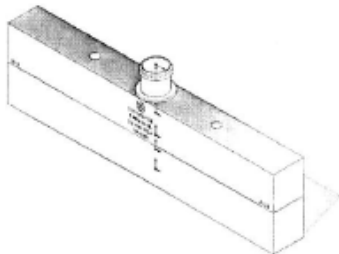
PINOUT INFORMATION

	4	3	4	3	2	1
A	Pos	Pos	1	50E	Pos	Pos
B	Pos	2	50D	3	Pos	1
C	07	Pos	18	50E	Pos	26
D	Pos	Pos	50D	13	Pos	Pos
E	23	34	Pos	50E	25	26
F	40	Pos	50D	Pos	50	Pos
G	Pos	50	Pos	50E	Pos	52
H	5	5	50D	Pos	7	3
J	21	Pos	Pos	50E	Pos	Pos
K	Pos	22	50D	22	Pos	24
L	27	Pos	30	50E	20	Pos
M	Pos	Pos	50D	48	Pos	Pos
N	52	54	Pos	50E	55	54
P	5	Pos	50D	Pos	11	Pos
R	Pos	8	Pos	12	Pos	Pos
S	28	29	50D	50E	27	28
T	Pos	Pos	41	50E	Pos	Pos
U	Pos	42	50D	23	Pos	44
V	57	Pos	50	50E	53	Pos
W	Pos	Pos	50D	50	Pos	Pos
X	13	14	Pos	3	15	16
Y	25	Pos	48	Pos	30	Pos
Z	Pos	30	Pos	5	Pos	22
a	48	48	5	50E	48	Pos
b	Pos	Pos	1000D	14	Pos	48
c	50	41	10	54	53	Pos

1D Element Geometry



Element Orientation 115-001-108



Chris Galland
12/18/2014